

Hochschule für Angewandte Wissenschaften Hamburg

Faculty of Life Sciences

Bachelor Thesis

Analysis of the Effect of Proximal and Distal Displacement  
Constraints on the Femur During Biomechanical Testing for  
Diaphyseal Implants

submitted by

Levita Graciella Valeriant



Degree of programme: Medizintechnik (Bachelor of Science)

Supervisor: Prof. Nicholas Bishop (HAW Hamburg)  
Supervisor: Dr. -Ing. Tobias Barth (BG Klinikum Hamburg)

**Hamburg, 15<sup>th</sup> November 2024**

## **Acknowledgements**

I would like to express my gratitude to my supervisors, Prof. Nicholas Bishop and Dr. -Ing. Tobias Barth, for their unwavering support and guidance throughout the writing process of this thesis. Thank you for making the time to discuss my questions and for proofreading my work. I am especially grateful to Prof. Nicholas Bishop for his assistance with the finite element analysis.

I also want to thank the Clinical Research department at BG Klinikum Hamburg for the opportunity to write my thesis there.

Finally, I want to extend my appreciation to my family and friends for their encouragement and support throughout my undergraduate studies. Special thanks to Michelle and Lyon for always being so supportive and for helping me every step of the way.

# Table of Content

List of Figures.....	IV
List of Tables.....	X
1 Introduction .....	1
2 State of the Art.....	3
2.1 Skeletal System.....	6
2.2 Femur.....	7
2.3 Femoral Shaft & Diaphyseal Fracture .....	10
2.3.1 AO/OTA Classification .....	11
2.3.2 Physiology of Fracture Healing.....	17
2.3.3 Treatment.....	18
2.3.3.1 Intramedullary Nailing .....	18
2.3.3.2 Plate Osteosynthesis .....	20
2.4 Preclinical testing for femoral implants.....	23
2.4.1 Loading.....	24
2.4.2 Proximal and Distal Constraints .....	27
2.4.3 Specimen .....	30
2.4.4 Outcomes .....	31
2.5 Femoral Loading during Gait .....	32
3 Chapter I: Finite Element Analysis .....	39
3.1 Finite Element Analysis – an Overview .....	39
3.2 Methodology-Finite Element Analysis and Analytical Modelling.....	41
3.3 Results .....	53
3.3.1 Bone.....	54
3.3.2 Plate .....	61

3.3.3	Nail .....	68
3.4	Discussion.....	70
4	Chapter II: Literature Review .....	74
4.1	Methodology.....	74
4.2	Result .....	76
4.3	Discussion.....	97
5	Discussion.....	101
5.1	Limitations.....	104
6	Conclusion .....	105
	Bibliography .....	108
	Affidavit.....	125

# List of Figures

<b>Figure 1.</b> The structural differences between trabecular bone and cortical bone. Figure adapted from (Willems et al., 2013). .....	6
<b>Figure 2.</b> Femur with all characteristic areas highlighted (Pérez-Cano et al., 2023). .....	8
<b>Figure 3.</b> Muscles attached to the femur categorized by compartments. Figure adapted from (Jones, 2023a, 2023b, 2024). .....	10
<b>Figure 4.</b> Alphanumeric structure of the AO/OTA fracture classification system to describe fractures (Meinberg et al., 2018). .....	12
<b>Figure 5.</b> Designation of bone location used in the AO/OTA fracture classification (Meinberg et al., 2018). .....	13
<b>Figure 6.</b> Three equal parts of the diaphyseal segment of the femur according to the AO/OTA fracture classification system (Meinberg et al., 2018). .....	14
<b>Figure 7.</b> Fracture types in the diaphyseal segment of the femur according to AO/OTA fracture classification system: 32A (Simple), 32B (Wedge), 32C (Multifragmentary). Each type is further divided into groups. Figure adapted from (AO Foundation, 2018). .....	15
<b>Figure 8.</b> Comparison of primary and secondary bone healing processes (Paruchuri, Choudur and Chodavarapu, 2023). .....	18
<b>Figure 9.</b> Two possible starting points in antegrade nailing: (A) Entry point through the piriformis fossa; (B) Entry point through the greater trochanter (Moein et al., 2005). .....	19
<b>Figure 10.</b> Two plating types: Conventional plating, where the plate is compressed onto the surface of the bone (a) and locked plating, where the screw engages in the plate hole and there is no direct bone and plate contact (Szypryt and Forward, 2009). .....	23
<b>Figure 11.</b> Test setups for: A) Compression test; B) Torsion test; C) Three-point bending test; D) Four-point bending test. Figure adapted from (Merriman et al., 2015; Nagler, 2019). .....	25
<b>Figure 12.</b> Stress distribution based on different loadings: Axial force ( $F$ ) leads to axial stress ( $\sigma_{Axial}$ ) (left) and bending moment ( $M$ ) leads to bending stress, which is a combination of compressive stress ( $\sigma_{Compressive}$ ) and tensile stress ( $\sigma_{Tensile}$ ) (right). .....	27
<b>Figure 13.</b> Coordinate system and the basic movement in 2D. ....	28
<b>Figure 14.</b> Examples of bearing types used in biomechanical testing. Figure adapted from (Grisell, Moed and Bledsoe, 2010; D. Wähnert et al., 2013). .....	29

**Figure 15.** The first four models of the lower limb in the coronal plane developed by Pauwels to demonstrate various structures in the skeleton that reduce stress on the bone. The graph next to the column shows the stress experienced by the column and the stress value in  $\text{kp/cm}^2$ . First, the limb was modelled as a single column (A). Next, he added the hip joint and the abductors (B). Then, he added the knee joint and the lateral ligament (C). In the fourth model, he enlarged the articulation to match the width of the knee joint (D). Figure adapted from (Pauwels, 1980). ..... 33

**Figure 16.** The last three models of the lower limb in the coronal plane developed by Pauwels to demonstrate various structures in the skeleton that reduce stress on the bone. The graph next to the column shows the stress experienced by the column and the stress value in  $\text{kp/cm}^2$ . He added the iliotibial band, the greater trochanter, and the flexor muscles (E). Then, an articulation was added to the lower end of the column and the column was inclined to the left around this joint (F). In the final model, he added an angulation at the middle joint (physiological valgum) (G). Figure adapted from (Pauwels, 1980). ..... 34

**Figure 17.** The first three models of the lower limb in the sagittal plane developed by Pauwels to demonstrate various structures in the skeleton that reduce stress on the bone. The graph next to the column shows the stress experienced by the column and the stress value in  $\text{kp/cm}^2$ . First, the limb was modelled as an inclined column (A). Then, he introduced three joints and a monoarticular muscle (B). Next, he added biarticular muscles (C). Figure adapted from (Pauwels, 1980). ..... 35

**Figure 18.** The last two models of the lower limb in the sagittal plane developed by Pauwels to demonstrate various structures in the skeleton that reduce stress on the bone. The graph next to the column shows the stress experienced by the column and the stress value in  $\text{kp/cm}^2$ . He bowed the femur forward and altered the shape of the articulation between the femur and tibia (D). In the last model, the short head of the biceps femoris was added (E). Figure adapted from (Pauwels, 1980). ..... 36

**Figure 19.** The model developed by Duda, Schneider and Chao (1997) to calculate the internal loads of the femur. The results of their research are shown in two graphs: the graph on the left shows the internal forces along the length of the femur and the graph on the right shows the internal moment along the length of the femur. The thin lines in both graphs represent the femoral loads with only hip contact considered (without muscles). Figure adapted from (Duda, Schneider and Chao, 1997). ..... 38

**Figure 20.** Twelve models developed for the study. The femur in models 1, 9, 10, 11, and 12 was oriented vertically, while in models 2 to 8 was oriented at a  $10^\circ$  angle. The coordinate system was aligned with the bone orientation. When the bone is vertical (as in models 1 and 9 to 12), the coordinate system is also vertical, as shown in model 1. However, in models where the femur is tilted  $10^\circ$  (models 2 to 8), the coordinate system is tilted  $10^\circ$  accordingly, as shown in model 2. The table next to the models shows the bearing symbols and their

respective movements. “0” indicates that no movement is allowed along the axis, while “Free” indicates that movement along the axis is permitted. .... 43

**Figure 21.** Plate placement and dimensions of the bone (femur) and lateral plate..... 45

**Figure 22.** Free body diagrams of the bone-plate structure, from which three equations were derived to calculate the internal forces along the x-axis ( $F2x(y)$ ), internal forces along the y-axis ( $F2y(y)$ ), and internal moments along the z-axis ( $M2zy$ ). A) shows the free body diagram for calculating  $F2xy, F2yy, M2zy$  along the bone and nail. B) shows the free body diagram for calculating  $F2xy, F2yy, M2zy$  along the plate. .... 47

**Figure 23.** Dimensions and geometry of the lateral plate used in this study..... 50

**Figure 24.** Dimensions and geometry of the bone and intramedullary nail used in this study. .... 51

**Figure 25.** Results of the analytical modelling: Internal forces along the x-axis ( $F2x$ ) in the bone for the models 1 to 12. The y-axis shows the internal forces along the x-axis ( $F2x$ ) in newtons (N), while the x-axis represents the length along the bone (y) in metres (m), with  $y = 0$  m at the distal end and  $y = 0,4$  m at the proximal end. Below the graph, the twelve models are displayed. The graphs for models 1, 7, 9, 10, 11, and 12 overlap due to their similar  $F2x$  values and the graph for model 8 is obscured by these graphs. Similarly, the graphs for models 2, 5, and 6 overlap due to their similar  $F2x$  values. The graphs for models 3 (dark purple) and 4 (light purple) are clearly visible in the combined graph. .... 54

**Figure 26.** Results of the analytical modelling: Internal forces along the y-axis ( $F2y$ ) in the bone for models 1 to 12. The y-axis shows the internal forces along the y-axis ( $F2y$ ) in newtons (N), while the x-axis represents the length along the bone (y) in metres (m), where  $y = 0$  m is the distal end and  $y = 0,4$  m is the proximal end. The twelve models are shown below the graph. The graphs of models 7 and 8 overlap due to their similar  $F2y$  values. Models 1, 9, 10, 11, and 12 also show overlapping graphs. Similarly, the graphs of models 5 and 6 overlap. The graphs for model 2 (grey), 3 (dark purple), and 4 (light purple) are clearly visible in the merged graph..... 55

**Figure 27.** Results of the analytical modelling: Internal moments ( $M2z$ ) along the bone for model 2, 3, 4, 5, 6, and 8 (non-constant group). The y-axis shows the internal moments ( $M2z$ ) in newton-metres (Nm), while the x-axis represents the length along the bone (y) in metres (m), where  $y = 0$  m is the distal end and  $y = 0,4$  m is the proximal end. The models are shown below the graph. Model 8 (light green) shows minimum variation in  $M2z$  along the bone, while the other models (2 (grey), 3 (dark purple), 4 (light purple), 5 (dark blue), and 6 (light blue)) exhibit significant variation in  $M2z$  along the bone..... 56

**Figure 28.** Results of the analytical modelling: Internal moments ( $M2z$ ) along the bone for models 1, 7, 9, 10, 11, and 12 (constant group). The y-axis shows the internal moments

( $M2z$ ) in newton-metres (Nm), while the x-axis corresponds to the length along the bone ( $y$ ) in metres (m), where  $y = 0$  m is the distal end and  $y = 0,4$  m is the proximal end. The corresponding models are shown below the graph. The internal moments along the bone for these models are approximately 0 Nm. Due to the similarity in their internal moments, their graphs overlap..... 57

**Figure 29.** Results of the analytical modelling: Absolute maximum stress values along the bone for models 2, 3, 4, 5, 6, and 8 (non-constant group). The y-axis represents the absolute maximum stress values in megapascals (MPa), while the x-axis corresponds to the length along the bone ( $y$ ) in metres (m), with  $y = 0$  m as the distal end and  $y = 0,4$  m as the proximal end. The corresponding models are shown below the graph. Model 8 (light green) shows minimum variation in stress values along the bone’s length, making the graph appears nearly constant. The other models (models 2 (grey), 3 (dark purple), 4 (light purple), 5 (dark blue), and 6 (light blue)) exhibit significant variation in stress values along the bone’s length. .. 58

**Figure 30.** Results of the analytical modelling: Absolute maximum stress values along the bone for models 1, 7, 9, 10, 11, and 12 (constant group). The y-axis represents the absolute maximum stress values in megapascals (MPa), while the x-axis corresponds to the length along the bone ( $y$ ) in metres (m), with  $y = 0$  m as the distal end and  $y = 0,4$  m as the proximal end. The corresponding models are shown below the graph. The graphs for these models overlap due to their similar stress distributions along the bone. .... 59

**Figure 31.** Results from the analytical modelling: Internal forces in the x-axis ( $F2x$ ) along the lateral plate for models 1 to 12. The y-axis shows the internal forces in the x-axis ( $F2x$ ) in newtons (N), and the x-axis represents the length along the plate ( $y$ ) in metres (m), where  $y = 0$  m is the distal end and  $y = 0,4$  m is the proximal end. The twelve models are shown below the graph. The graphs for models 2, 5, and 6 overlap due to their similar  $F2x$  values. Similarly, the graphs for models 1, 8, 10, 11, and 12 overlap. The graphs for models 3 (dark purple), 4 (light purple), 7 (dark green), and 9 (dark red) are clearly visible in the combined graph. .... 61

**Figure 32.** Results from the analytical modelling: Internal forces in the y-axis ( $F2y$ ) along the lateral plate for models 1 to 12. The y-axis shows the internal forces in the y-axis ( $F2y$ ) in newtons (N), while the x-axis corresponds to the length along the plate ( $y$ ) in metres (m), where  $y = 0$  m is the distal end and  $y = 0,4$  m is the proximal end. The twelve models are shown below the graph. The graphs for models 1, 9, 10, 11, and 12 overlap due to their similar  $F2y$  values. Similarly, the graphs for models 5 and 6 overlap, partially obscuring the graph for model 2. The graphs for models 3 (dark purple), 4 (light purple), 7 (dark green), 8 (light green) are clearly visible in the combined graph. .... 62

**Figure 33.** Results from the analytical modelling: Internal moments in the z-axis ( $M2z$ ) along the lateral plate for models 2, 3, 4, 5, 6, 7, and 9 (non-constant group). The y-axis shows the internal moments in the z-axis ( $M2z$ ) in newton-metres (Nm), while the x-axis

corresponds to the length along the plate ( $y$ ) in metres (m), where  $y = 0$  m is the distal end and  $y = 0,4$  m is the proximal end. The corresponding models are shown below the graph. Compared to models 2 (grey), 3 (dark purple), 4 (light purple), 5 (dark blue), and 6 (light blue), models 7 (dark green) and 9 (dark red) exhibit lower  $M2z$  values along the lateral plate. .... 63

**Figure 34.** Results from the analytical modelling: Internal moments in the z-axis ( $M2z$ ) along the lateral plate for models 1, 8, 10, 11, and 12 (constant group). The y-axis shows the internal moments in the z-axis ( $M2z$ ) in newton-metres (Nm), while the x-axis represents the length along the plate ( $y$ ) in metres (m), where  $y = 0$  m is the distal end and  $y = 0,4$  m is the proximal end. The corresponding models are shown below the graph. Due to their similar  $M2z$  values along the plate, the graphs for models 1 and 10 overlap. Similarly, the graphs for models 11 and 12 overlap, partially obscuring the graph for model 8. .... 64

**Figure 35.** Results from the analytical modelling: Absolute maximum value of stress along the lateral plate for models 2, 3, 4, 5, 6, 7, and 9 (non-constant group). The y-axis shows the stress values in megapascals (MPa), while the x-axis corresponds to the length along the plate ( $y$ ) in metres (m), where  $y = 0$  m is the distal end and  $y = 0,4$  m is the proximal end. The corresponding models are shown below the graph. .... 65

**Figure 36.** Results from the analytical modelling: Absolute maximum value of stress along the lateral plate for models 1, 8, 10, 11, and 12 (constant group). The y-axis shows the stress values in megapascals (MPa), while the x-axis corresponds to the length along the plate ( $y$ ) in metres (m), where  $y = 0$  m is the distal end and  $y = 0,4$  m is the proximal end. The corresponding models are shown below the graph. Due to their similar stress values along the plate, the graphs for models 1 and 10 overlap. Similarly, the graphs for models 11 and 12 overlap, partially obscuring the graph for model 8. .... 66

**Figure 37.** Results from the analytical modelling: Absolute maximum value of stress along the nail for models 2, 3, 4, 5, 6, and 8 (non-constant group). The y-axis shows the stress in megapascals (MPa), while the x-axis corresponds to the length along the nail ( $y$ ) in metres (m), with  $y = 0$  m as the distal end and  $y = 0,4$  m as the proximal end. The corresponding models are shown below the graphs. The stress values in model 8 (light green) vary only slightly along the nail's length, which is why the graph seems constant. In contrast, the stress values in models 2 (grey), 3 (dark purple), 4 (light purple), 5 (dark blue), and 6 (light blue) vary significantly along the nail's length. .... 69

**Figure 38.** Results from the analytical modelling: Absolute maximum value of stress along the nail for models 1, 7, 9, 10, 11, and 12 (constant group). The y-axis shows the stress in megapascals (MPa), while the x-axis represents the length along the nail ( $y$ ) in metres (m), with  $y = 0$  m as the distal end and  $y = 0,4$  m as the proximal end. The corresponding models are displayed below the graphs. The graphs for models 1, 9, 10, 11, and 12 overlap due to similar stress values along the nail's length, obscuring the graph for model 7. .... 70

**Figure 39.** The twelve models developed for the study. Reproduced from Section 3.2 Methodology-Finite Element Analysis and Analytical Modelling, Figure 20. .... 71

**Figure 40.** The process of article selection and the number of papers included at each stage. .... 77

## List of Tables

<b>Table 1.</b> Mechanical properties of 316L, Ti-6Al-4V ELI, and Ti-6Al-7Nb (Ninomi, 1998; Gervais et al., 2016; Li et al., 2020). .....	21
<b>Table 2.</b> Possible constraint combinations in 2D and their stability. The highlighted rows indicate the combinations simulated in the finite element analysis. “0” indicates that no movement is allowed along the axis, while “Free” indicates that movement along the axis is permitted.....	42
<b>Table 3.</b> Displacement constraint sets for the twelve models.....	44
<b>Table 4.</b> Results from the finite element analysis of the bone model: Minimum and maximum normal stress values in the bone.....	60
<b>Table 5.</b> Results from the finite element analysis of the plate model: Minimum and maximum normal stress values in the plate.....	67
<b>Table 6.</b> Results from the literature review: Parameters regarding the biomechanical test setup extracted from studies focusing on femoral mid-shaft plate osteosynthesis.....	79
<b>Table 7.</b> Results from the literature review: Parameters regarding the biomechanical test setup extracted from studies focusing on intramedullary nails for mid-shaft fracture fixation. ....	94
<b>Table 8.</b> Results from the literature review: Number of papers and corresponding models similar to the axial compression test setups.....	97

# 1 Introduction

Diaphyseal femur fractures, also known as femoral shaft fractures, are among the most common injuries in orthopaedic practice (Denisiuk and Afsari, 2023). These fractures typically result from high-energy trauma, such as motor vehicle accidents, particularly in younger populations. However, in elderly patients, they are more commonly associated with low-energy trauma, such as slips, trips, or falls from standing height (Zhu *et al.*, 2020; Denisiuk and Afsari, 2023). Globally, the incidence of femoral shaft fractures is estimated to range from 10 to 21 cases per 100.000 individuals annually, highlighting their significant impact on healthcare systems (Denisiuk and Afsari, 2023). The incidence in low- and middle-income countries is higher than the incidence observed in high-income countries, with rates ranging from 15,7 to 45,5 per 100.000 people annually (Agarwal-Harding *et al.*, 2015). When not appropriately treated, femoral shaft fractures can lead to disability. The disability weight associated with femoral shaft fractures is estimated at 0,272; this number is higher than that for malaria (0,191) and comparable to untreated tuberculosis (0,271) (Kramer *et al.*, 2016).

A variety of treatment options are available for managing femoral shaft fractures, ranging from non-operative methods such as traction and bracing to operative interventions like intramedullary nailing, external fixation, and plate osteosynthesis (Denisiuk and Afsari, 2023; Miao and Miao, 2023). Among these, intramedullary nailing, which involves inserting a metal rod into the medullary canal of the femur and securing it with screws at both ends, is considered the gold standard for treating femoral shaft fractures due to its ability to provide stable fixation and promote early mobilization (Helmy *et al.*, 2008; Medda, Unger and Halvorson, 2023; Oesman, Kurniawan and Canintika, 2023). However, in certain clinical scenarios, such as recalcitrant nonunions, narrow femoral canals, open fractures with associated vascular injury, or fractures located either too proximal or distal from the femoral shaft, intramedullary nails may not be suitable (Yates and Fountain, 2016; Denisiuk and Afsari, 2023). In these cases, plate osteosynthesis is often the preferred alternative. This method stabilizes and fixes fractured bones with plates and screws.

The development and evaluation of orthopaedic implants require preclinical testing to ensure their safety, durability, and effectiveness. Both the implant and its interfaces with the body must be evaluated. Biomechanical testing plays a crucial role in this process, providing insights into how these implants interact with the body under physiological loading conditions. Typically, biomechanical tests involve the use of osteotomized cadaver bones or synthetic bone models, modified to simulate post-fracture and post-reduction conditions (Schorler *et al.*, 2017). These tests are usually conducted using a material testing machine, which applies various loading regimes, including compression, bending, torsion, and often the combination of these loadings to better mimic the complex loading conditions experienced by bones during daily activities, to the bone-implant constructs (Zhang *et al.*, 2022).

One of the most critical activities to consider in biomechanical testing is gait, as it is a repetitive activity that places continuous stress on the femur and the implanted constructs. There has been ongoing debate in the literature regarding how the femur is loaded during gait, but evidence suggests that the body has mechanisms to limit bending forces, resulting in low compressive stresses within the femur (Pauwels, 1980; Taylor *et al.*, 1996; Duda, Schneider and Chao, 1997).

Biomechanical test setups in studies on implants for diaphyseal femur fractures show considerable variation, particularly in the design of the distal and proximal test fixtures used to hold the femurs during testing. This lack of standardization makes it difficult to interpret and compare the results related to the mechanical behaviour of bone-implant constructs (Schorler *et al.*, 2016; Wang *et al.*, 2019). Inacio *et al.* (2022) highlighted that the mechanical performance of the constructs is highly sensitive to the boundary conditions imposed by the test fixtures, with increased degree of constraints leading to a significant increase in axial stiffness.

Given these challenges, the present study aims to determine how the proximal and distal displacement constraints of the femur during biomechanical testing affect the internal forces, moments, and stresses within the bone, osteosynthesis nails and laterally mounted plates. An overview of crucial knowledge necessary to comprehend these challenges is provided in the section “State of the Art” (see 2 State of the Art). To address the aim of the study, a finite

element model is combined with analytical modelling to investigate the effects of testing setup on internal forces and moments, as well as the resulting stresses in intact bone, a lateral plate, and an intramedullary nail (see 3 Chapter I: Finite Element Analysis). Additionally, a comprehensive literature review of femoral mid-shaft fracture studies will be conducted to assess and discuss the appropriateness and effectiveness of the chosen biomechanical testing setup for addressing the study's objectives (see 4 Chapter II: Literature Review). Through this approach, the study seeks to contribute to the standardization of biomechanical testing methods by improving the understanding of how test setups influence the mechanical behaviour of bone-implant constructs and suggesting realistic test setups. The results are discussed (see 5 Discussion) and summarized (see 6 Conclusion) at the end of this study.

## **2 State of the Art**

This section provides the theoretical foundation for the thesis. It begins with an overview of the skeletal system, covering its functions and the types of bones in the human body (see 2.1 Skeletal System). The femur, as the main focus of this study, is part of the skeletal system, which serves three primary functions: mechanical support, hematopoietic cell formation, and metabolic regulation (Clarke, 2008; Baig and Bacha, 2023). This study primarily focuses on the mechanical function of the skeletal system. Based on its shape, the femur is classified as a long bone. Long bones are characterized by three anatomical regions: the diaphysis (shaft), the epiphysis, and the metaphysis. The epiphysis, located at the ends of long bones, and the metaphysis, found between the diaphysis and epiphysis, are primarily composed of trabecular bone. The diaphysis or shaft of long bones has medullary cavity, and its outer layer is composed of cortical bone (Cowan, Launico and Kahai, 2024).

The subsequent section provides a comprehensive overview of the femur (see 2.2 Femur), examining its anatomical division into three primary regions: proximal, shaft, and distal. The shaft, which serves as the primary focus of this study, is located between the proximal and distal regions. Additionally, this section highlights the muscles attached to the femur, which play a crucial role in limiting bending forces and stress on the femur. These aspects will be further discussed in the section on femoral loading during gait.

The next section discusses diaphyseal femur fractures (see 2.3 Femoral Shaft & Diaphyseal Fracture). External forces exerted on the femur generate stress within the femur (Morgan and Bouxsein, 2008). When the stress exceeds the femur's yield strength, fractures occur. The yield strength of cortical bone, as the main material of the diaphyseal femur, typically ranges between 75,9–136,6 MPa (Baleani *et al.*, 2024). This section covers one of the most used fracture classification systems, which provides a standardized approach for evaluating fracture severity and selecting appropriate treatment methods. It is also useful for documenting clinical studies, allowing readers to recognize fracture patterns without the need to include multiple X-rays (Eveleigh, 1997). This section offers insights into the types of fractures observed in the diaphyseal femur.

When discussing fractures, it is essential to also address fracture healing and the available treatment options. These topics are explored in separate sections. In the treatment section, two common options to treat diaphyseal femur fractures are discussed: intramedullary nails and plate osteosynthesis (conventional and locked plating).

Fracture healing can be classified into two types: primary and secondary healing. The type of healing that occurs depends on the amount of motion and mechanical strain at the fracture site. Primary bone healing happens when the mechanical strain at the fracture site is less than 2%, while secondary bone healing occurs when the mechanical strain is kept between 2% and 10% (Sheen, Mabrouk and Garla, 2023).

These types of fracture healing are directly related to the choice of implant, as different implants promote different healing processes. For instance, intramedullary nails and locked plating typically promote secondary healing (Augat and von Ruden, 2018; Sheen, Mabrouk and Garla, 2023). On the other hand, conventional plating is designed for fractures that benefit from primary bone healing (Augat and von Ruden, 2018). In both cases, the implant must ensure proper anatomical alignment of the bone and may bear most or all of the mechanical load during the early stages of recovery (Eveleigh, 1997). Implants for orthopaedic purposes, such as intramedullary nails and plates, are typically made from materials like titanium alloys (such as Ti–6Al–4V and Ti–6Al–7Nb) and stainless steel (316L) (Heyland *et al.*, 2017; Zhang *et al.*, 2022). These materials are selected for their

strength, biocompatibility, and resistance to corrosion. The yield strength for these materials ranges between 795 MPa and 1000 MPa.

Preclinical testing for femoral implants, including the types of tests used to evaluate implants and parameters involved in biomechanical testing—such as loading, proximal and distal constraints, specimen type, and outcomes—is described afterwards (see 2.4 Preclinical testing for femoral implants). This section emphasizes the importance of preclinical testing and how it is conducted. Preclinical testing ensures that implants meet safety and performance standards before they are used in clinical settings. It is normally conducted using a material testing machine and can be categorized into two types:

- Mechanical testing for regulatory purposes: In this type of test, only the implant is evaluated according to published, internationally recognized standards (Schorler *et al.*, 2017).
- Biomechanical testing: This type of testing involves fixing the implants to cadaveric or synthetic bones, which are osteotomized to simulate specific types of fractures. The bone-implant construct is then subjected to loading conditions that closely resemble physiological scenarios (Schorler *et al.*, 2017).

This study focuses on biomechanical testing, with a particular emphasis on the proximal and distal constraints. There is still a lack of standardization in the parameters involved in biomechanical testing, including the applied loading (Schorler *et al.*, 2016; Wang *et al.*, 2019). Gait is one of the activities that researchers commonly attempt to mimic during testing (Lever *et al.*, 2010; O’Connell *et al.*, 2018; Wisanuyotin *et al.*, 2023).

Lastly, a section on how the femur is loaded during gait completes the state of the art (see 2.5 Femoral Loading during Gait). Gait is a repetitive activity that humans perform, placing continuous stress on the femur and the implants. This section explores theories about how the femur is loaded during gait. According to Munich, Kralj and Bajd (1992) and Pauwels (1980), muscles help limit the bending moments and stresses experienced by the femur. Additionally, studies by Taylor *et al.* (1996) and Duda, Schneider and Chao (1997) show that during gait, the femur is mainly subjected to axial compression with limited bending. These findings support the application of axial compression to the femur in biomechanical testing, as it better reflects the actual loading conditions the femur experiences during

walking. The bending moment experienced by the femur during biomechanical testing should be limited.

## 2.1 Skeletal System

The human skeletal system has three primary functions: mechanical support, hematopoietic cell formation, and metabolic regulation. Its mechanical support role includes providing a frame for muscles, tendons, and ligaments to attach, enabling movement. It also gives structural support for the body and protects internal organs. In its role in hematopoietic cell formation, bone marrow, which can be found within the trabecular sections of the bones, produces red blood cells, white blood cells, and platelets through a process called haematopoiesis. For metabolic regulation, the bone matrix stores essential minerals such as calcium, phosphorus, and iron (in the form of ferritin). Additionally, bones help regulate pH levels (Clarke, 2008; Baig and Bacha, 2023).

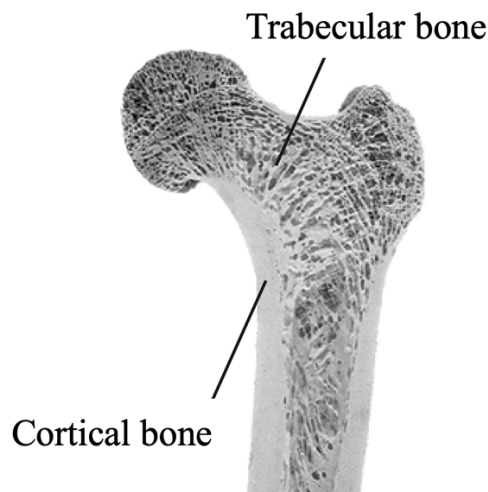


**Figure 1.** The structural differences between trabecular bone and cortical bone. Figure adapted from (Willems *et al.*, 2013).

There are two main types of bone in the human body: cortical and trabecular (Figure 1) (ElHawary *et al.*, 2021). Cortical bone makes up 80% of the skeleton, while the remaining 20% is trabecular bone (Nandiraju and Ahmed, 2019). Cortical bone is stronger, denser, and provides more resistance to bending, torsion, and compression. The shaft of long bones and the outer shell of trabecular bone are primarily composed of cortical bone. On the other hand, trabecular bone is more dynamic and responds more quickly to changes in load. It is

commonly found in areas subjected to higher compressive forces, such as the vertebral bodies, pelvis, and metaphysis of long bones (Baig and Bacha, 2023).

Based on their shape, bones in the human body can be categorized into four groups: flat bones, irregular bones, short bones, and long bones (Clarke, 2008). Flat bones are thin and made up of a layer of trabecular bone surrounded by two layers of cortical bone, with the mandible and calvaria being the examples. The second category is irregular bones, such as the vertebrae and the hyoid bone. Short bones are typically cube-shaped with approximately equal horizontal and vertical dimensions. Examples of short bones in the human skeletal system are the carpal and tarsal bones. Irregular bones and short bones are primarily composed of trabecular bone, covered by a thin layer of cortical bone (ElHawary *et al.*, 2021).

Lastly, long bones have three anatomical regions: diaphysis (shaft), epiphysis, and metaphysis. The inner part of the diaphysis is hollow, known as the medullary cavity. In newborn mammals, the medullary cavity contains red bone marrow. Starting from the early postnatal period, the red bone marrow, particularly in the bones of the extremities, is gradually replaced by yellow bone marrow (Gurevitch, Slavin and Feldman, 2007). The outer layer of the diaphysis is composed of cortical bone. In contrast, the epiphysis and metaphysis are primarily composed of trabecular bone surrounded by a thin shell of cortical bone. The epiphysis, located at the ends of long bones, contains red marrow, which is crucial for blood cell production. The metaphysis, located between diaphysis and epiphysis, houses the epiphyseal plate in children, which is responsible for linear bone growth (Cowan, Launico and Kahai, 2024). Femur, humerus, and radius are examples of long bones (ElHawary *et al.*, 2021).

## **2.2 Femur**

As mentioned in the previous section, femur, which is the focus of this study, is a long bone. The femur is considered the longest and strongest long bone in the human body (Henle, 2008). Its primary functions include bearing weight and maintaining stability during movement (Chang *et al.*, 2023). The femur is anatomically divided into three primary sections: proximal, shaft, and distal region (Figure 2). The proximal region extends from the femoral head to the subtrochanteric region, which is defined as the area 5 cm distal to the

lesser trochanter (Jackson, Tanios and Ebraheim, 2018). The distal region covers the 15 cm distal of the femur (Coon and Best, 2023). The shaft region is located between the proximal and distal regions.

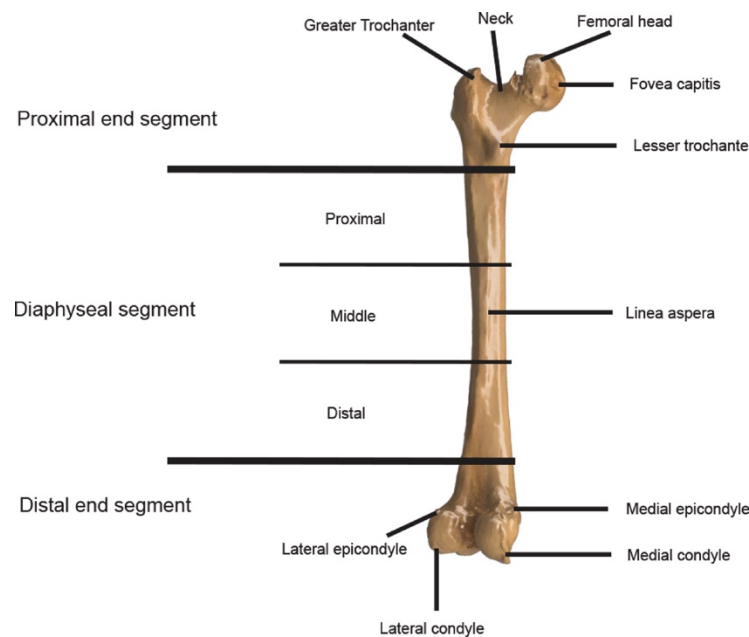


**Figure 2.** Femur with all characteristic areas highlighted (Pérez-Cano *et al.*, 2023).

The proximal femur is divided into four main regions: femoral head, femoral neck, intertrochanteric region, and subtrochanteric region (Konda, 2017). The femoral head, which is the most proximal part of the femur, is supported by the femoral neck. The neck is embryologically a continuation of the shaft and forms an angle with the shaft which ranges from  $120^{\circ}$  to  $140^{\circ}$  in adult (Harty, 1984; Haddad *et al.*, 2022). This angle is called the neck-shaft angle (NSA) or caput-collum-diaphyseal (CCD) angle. The articulation between the femoral head and the acetabulum of the pelvis forms the hip joint (Lo, Talkad and Sharma, 2023). The hip joint is a ball-and-socket joint with three degrees of freedom. It allows movement of the thigh in sagittal, transverse, and frontal plane (Hamill and Knutzen, 2006).

The intertrochanteric region is located between the greater and lesser trochanters. The greater trochanter serves as an attachment site for several muscles, such as gluteus medius, gluteus minimus, obturator internus, and piriformis. It's also the site from where vastus lateralis originates. The lesser trochanter is smaller than the greater trochanter and serves as the attachment site for the iliacus and psoas major (Attum and Pilson, 2023). The subtrochanteric

region is defined as the area 5 cm distal to the lesser trochanter (Jackson, Tanios and Ebraheim, 2018).

The femoral shaft is also often called the diaphysis of the femur. On the posterior surface of the femoral shaft, there are roughened, longitudinally oriented, irregular ridges of bone, called the *linea aspera*. This structure has two lips: the *labium mediale* and the *labium laterale* (Abdelaal *et al.*, 2016). The lateral lip continues proximally as the gluteal tuberosity, while the medial lip diverges into two separate lines—*spiral line* and *pectineal line* (Polguy *et al.*, 2013).

The distal femur refers to the area from the metaphyseal-diaphyseal junction to the articular surface of the knee. It has a trapezoidal shape, when viewed from the axial plane (Coon and Best, 2023). The distal femur houses the medial and lateral condyles, which articulate with the tibia and patella to form the knee joint (Chang *et al.*, 2017). The medial condyle extends farther distally than the lateral condyle (Coon and Best, 2023). The area between the 2 condyles is called *intercondylar fossa*. This area houses the anterior (ACL) and posterior (PCL) cruciate ligaments, the anterior (aMFL) and posterior (pMFL) meniscomfemoral ligaments, and pericruciate fat, all of which contribute to stabilizing the knee joint (Hirtler, Kainberger and Röhrich, 2022). The knee joint is typically considered to have two degrees of freedom: flexion and extension in the sagittal plane and rotation in the transverse plane. However, the joint also experiences slight linear translation in the frontal plane when the joint surfaces glide over one another, although these are not classified as an additional degree of freedom (Hamill and Knutzen, 2006).

The femur consists of two types of bone: cortical and trabecular. Cortical bone forms the outer layer of the shaft, while trabecular bone is found at the proximal and distal ends of the femur (Gautam and Rao, 2019). This distribution is typical for long bones (see Section 2.1 Skeletal System).

Many muscles attach to the femur, playing crucial roles in the movement and stability of the thigh and leg. These muscles primarily facilitate movements of the hip and knee joints during activities like walking, running, and jumping. They can be divided into three compartments: anterior compartment, posterior compartment, and medial compartment (Figure 3) (Chao, McCann and Fowler, 2014; Betts *et al.*, 2022; Larson and Ryan, 2023; Launico, Sinkler and

Nallamothu, 2023). The anterior compartment contains muscles for hip flexion and knee extension. Muscles in the posterior compartment function mainly as hip extensors and knee flexors. Muscles in the medial compartment are mainly involved in thigh adduction (Launico, Sinkler and Nallamothu, 2023). Muscle contractions induce complex loading patterns in the femur (Björnsdóttir, 2014). These loading patterns, combined with external forces, can lead to stress that contribute to the risk of fracture. The fractures in the diaphyseal segment of the femur will be discussed in the next section.

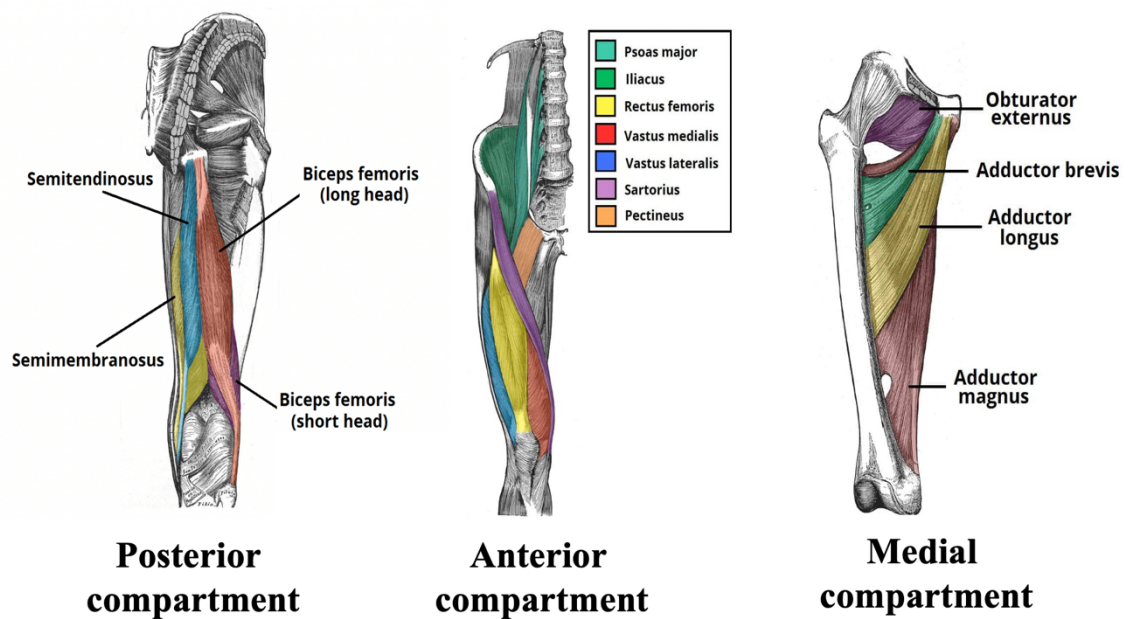


**Figure 3.** Muscles attached to the femur categorized by compartments. Figure adapted from (Jones, 2023a, 2023b, 2024).

## 2.3 Femoral Shaft & Diaphyseal Fracture

External forces result in complex and varied stress distributions throughout bone structures (Morgan and Bouxsein, 2008). Materials, including bones, fail when their stress surpasses their strength. The yield point on a stress-strain curve is the point at which the bone enters the plastic region, where stress causes permanent and irreversible damage to the bone structure (Downey and Siegel, 2006). This point, also known as yield strength, is often used to assess the strength of the bone (Bluemel *et al.*, 2015). The yield strength of cortical bone, which is the main material of diaphyseal femur, typically falls within the range of 75,9–136,6 MPa (Baleani *et al.*, 2024). Trabecular bone has a lower yield strength, typically ranging from 3 MPa to 12 MPa (Bazyar *et al.*, 2023).

Femoral diaphyseal fracture refers to a crack or break within the shaft (diaphysis) of the femur. These fractures often result from high-energy trauma (e.g. automobile accidents and falls from height) in young population and lower energy trauma (e.g. ground-level falls) in elderly population, which is linked to osteoporosis (Denisiuk and Afsari, 2023). Femoral shaft fractures are frequently seen in older individuals, particularly those with lower bone density, low body mass index, and anterior and lateral bowing of the femur (Medda, Unger and Halvorson, 2023). These fractures are often associated with polytrauma, open fractures, and multiple fractures (El Beaino *et al.*, 2019; Saraç, Karadeniz and Özer, 2021).

### **2.3.1 AO/OTA Classification**

To easily distinguish various fracture patterns, many classification systems have been developed. The AO/OTA classification is one of the most used fracture classification systems thanks to its high interobserver reliability and accuracy (Denisiuk & Afsari, 2023). The AO/OTA classification is a system used to classify fractures based on their anatomical location and fracture pattern. It was developed by the AO Foundation (Arbeitsgemeinschaft für Osteosynthesefragen or "Association for the Study of Internal Fixation" in English) and the Orthopaedic Trauma Association (OTA). The classification was published as a compendium in 1996 and then it was updated in 2018 (Meinberg *et al.*, 2018). The AO/OTA classification system helps standardize communication about fractures among healthcare professionals, aiding in treatment planning and ensuring consistent terminology across medical disciplines. The classification adopted a five-element alphanumeric code to describe fractures, as shown in Figure 4 (Zhang, 2016).



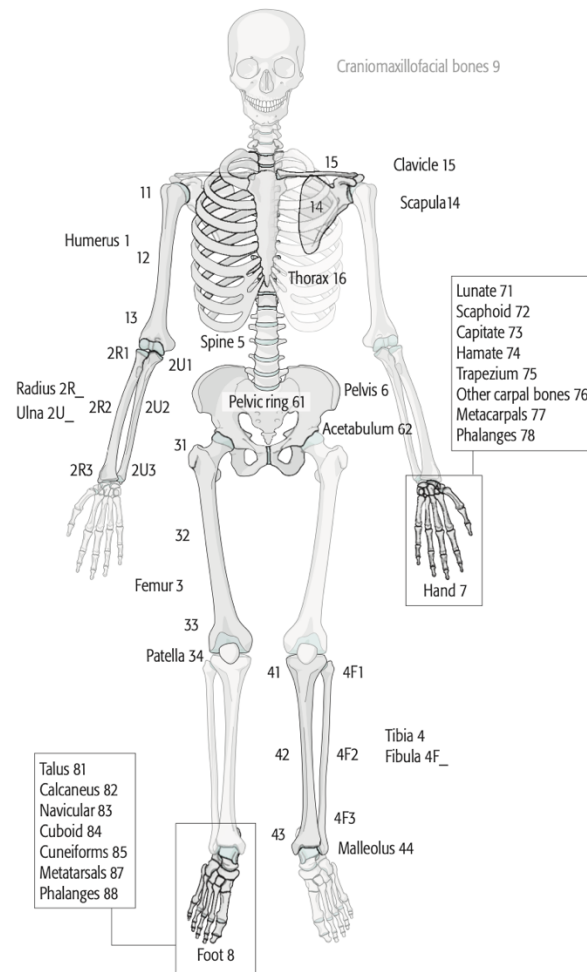


**Figure 5.** Designation of bone location used in the AO/OTA fracture classification (Meinberg *et al.*, 2018).

In the second step, the fracture location is determined. Each bone is divided into segments and the segment number represents the second number of the alphanumeric code. The femur is divided into three bone segments and they are numbered as (Meinberg *et al.*, 2018):

- Proximal end segment = 1,
- Diaphyseal segment = 2,

The diaphyseal segment is divided into three equal parts (Figure 6):

- Proximal 1/3,
- Middle 1/3,
- Distal 1/3,

These diaphyseal parts are noted in the fracture qualifications to provide a more precise fracture location. Fracture qualifications are terms used to describe fracture morphology or location that are specific to each fracture (Meinberg *et al.*, 2018).

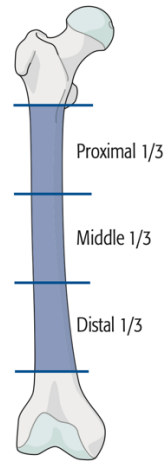


**Figure 6.** Three equal parts of the diaphyseal segment of the femur according to the AO/OTA fracture classification system (Meinberg *et al.*, 2018).

- Distal end segment = 3.

The next step is to identify the fracture type, which describes the fracture patterns and is represented by an uppercase letter in the alphanumeric code. Following this, the group and subgroup should be identified. The group provides a more specific description based on the individual bone or specific fracture pattern (Meinberg *et al.*, 2018). The groups are further subdivided into subgroups that provide further detail on the fracture characteristics, such as the fracture pattern, degree of displacement, and other specific features (Jankowski, no date). These subgroups differ amongst each bone. Next, the fracture qualifications should be identified. The fracture qualifications are expressed in lowercase letters. In the diaphyseal segment of the femur, these qualifications define the precise location of the fracture within that segment (Meinberg *et al.*, 2018). The fracture qualifications in the diaphyseal segment of the femur include:

- a: Proximal 1/3,
- b: Middle 1/3,
- c: Distal 1/3,
- i: Proximal diaphyseal-metaphyseal,

- j: Pure diaphyseal,
- k: Distal diaphyseal-metaphyseal.

The final step is to identify the universal modifiers, which are terms used to describe the fracture morphology, displacement, associated injury, or location that apply broadly across most fractures (Meinberg *et al.*, 2018).

For fractures in the diaphyseal segment of the femur (bone 3, segment 2), the fracture patterns are classified into three types: “simple” (A), “wedge” (B), and “multifragmentary” (C). Each type is further subdivided into specific fracture groups (Figure 7) (Trompeter and Newman, 2013).

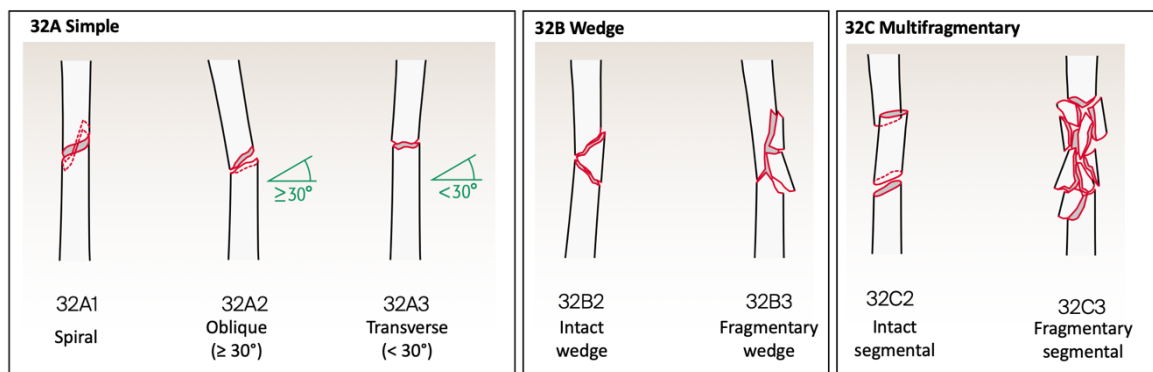


**Figure 7.** Fracture types in the diaphyseal segment of the femur according to AO/OTA fracture classification system: 32A (Simple), 32B (Wedge), 32C (Multifragmentary). Each type is further divided into groups. Figure adapted from (AO Foundation, 2018).

Following are the fracture types explained:

- Simple fractures (Type A) are identified by a cortical disruption of at least 90% of the bone’s circumference (Eveleigh, 1997). This fracture can be divided into three groups:
  - Spiral fracture  
Spiral fractures occur when the bone is subjected to torsional loads or a combination of torsional and axial loads (Morgan and Bouxsein, 2008). Falls from height may cause this type of fracture (Giannoudis, Pape and Schütz, no date b). When spiral fractures are treated with traction, they often result in external rotatory deformity (Rixford, 1925).
  - Oblique fracture

Oblique fractures are caused by pure compressive forces or in combination with bending loads (Morgan and Bouxsein, 2008). This type of fracture is identified by a fracture angle greater than 30° and considered unstable (Ömeroğlu, 2018; Giannoudis, Pape and Schütz, no date a). Oblique fractures often experience high levels of shear motion at the fracture site, which can lead to complications such as delayed healing or nonunion of the bone (Metcalf, Saleh and Yang, 2005).

- Transverse fracture

Transverse fractures are often caused by direct bending force. This type of fracture requires absolute stability with no interfragmentary motion for effective treatment, which can be achieved through compression plating (Giannoudis, Pape and Schütz, no date c).

- Wedge fractures (Type B) are characterized by a wedge-shaped gap or break in the bone. Following reduction, this fracture type still retains cortical contact between the main fragments (Kellam, 2018; Meinberg *et al.*, 2018). These fractures typically result from a three-point bending force applied to the bone (Giannoudis, Pape and Schütz, no date d). The wedge fragment can be intact or in multiple fragments.
- Multifragmentary fractures (Type C) are fractures with more than one fracture line, resulting in one or more fracture fragments (Cornelius *et al.*, 2014). These fractures are referred to as "complex fractures" in the Müller comprehensive classification (Meinberg *et al.*, 2018). Unlike wedge fractures, following reduction, there is no cortical contact between the main proximal and distal fragments (Kellam, 2018). Multifragmentary fractures are further divided into two groups: intact segmental and fragmentary segmental (Meinberg *et al.*, 2018).

The fracture pattern plays a crucial role in helping surgeons decide the most suitable treatment for effective fracture healing. For simple fractures, direct reduction with interfragmentary compression is often recommended to minimize interfragmentary motion and facilitate primary bone healing. On the other hand, comminuted fractures are better treated with indirect reduction and bridging fixation using plates, intramedullary nails, or external fixators. These methods provide relative stability, which allows controlled interfragmentary motion to stimulate callus formation, promoting secondary fracture healing. In comminuted fractures, the motion is distributed across multiple fracture gaps,

which allows this fracture type to tolerate more movement than simple fractures (Hak *et al.*, 2010). The differences between the two types of fracture healing will be discussed in the next section.

### **2.3.2 Physiology of Fracture Healing**

Bone or fracture healing can be classified into two types: primary and secondary (Figure 8). Primary healing occurs when bone fragments are fixed under compression with no movement at the fracture site, typically achieved through open reduction and internal fixation under compression (ElHawary *et al.*, 2021). This type of healing takes place when mechanical strain is kept below 2%, allowing the bone to heal through direct remodelling of lamellar bone and Haversian canals (Sheen, Mabrouk and Garla, 2023). However, this type of bone healing is less common compared to secondary bone healing (Fong, Chan and Goodman, 2011).

Secondary bone healing occurs in non-operative fracture treatment or in certain operative treatments where some motion occurs at the fracture site, with mechanical strain between 2-10% (Marsell and Einhorn, 2011; Sheen, Mabrouk and Garla, 2023). Secondary healing occurs via four main stages. The first stage is the formation of hematoma, which forms a temporary scaffold for callus formation. In the second stage, mesenchymal stem cells differentiate into fibroblasts, osteoblasts, and chondroblasts, forming a fibrocartilaginous network across the fracture site. In the third stage, the soft callus is replaced by hard callus through endochondral ossification. In the final stage, the bony callus is remodelled by osteoclasts and osteoblasts into compact bone centrally and lamellar bone peripherally, restoring the bone's strength and stability (ElHawary *et al.*, 2021).

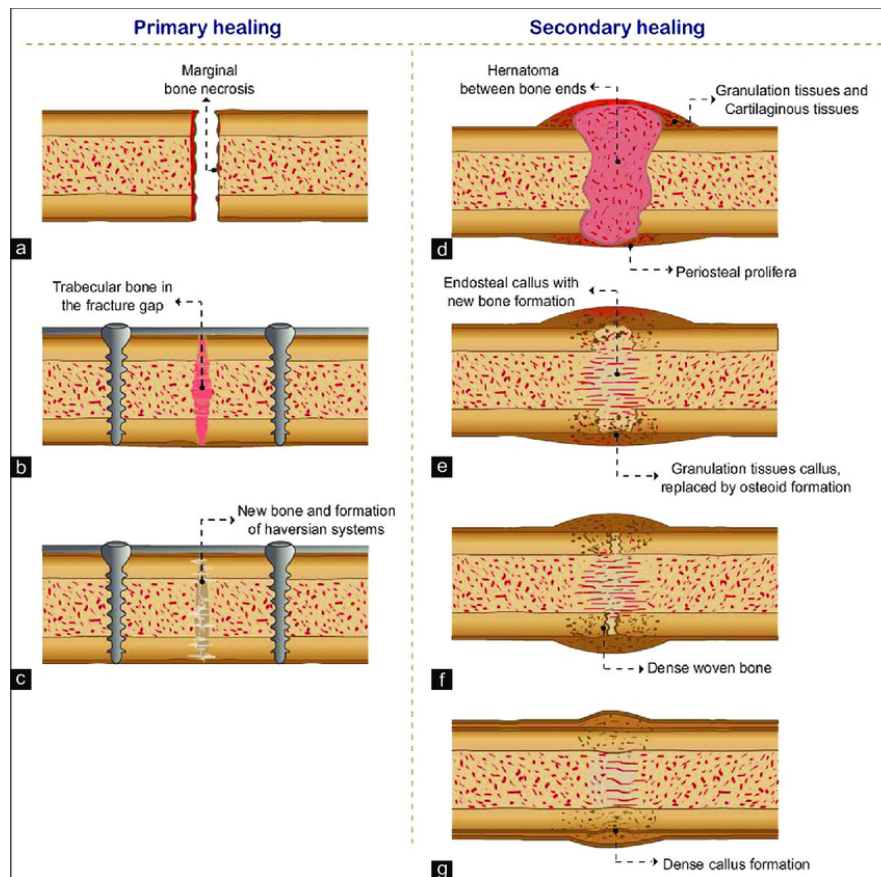


**Figure 8.** Comparison of primary and secondary bone healing processes (Paruchuri, Choudur and Chodavarapu, 2023).

Strain greater than 10% can lead to nonunion or delayed union (Sheen, Mabrouk and Garla, 2023). In such cases, the osteosynthesis is considered to have failed.

The type of fracture treatment used influences the type of bone healing achieved. Details on available fracture treatments will be discussed in the next section.

### 2.3.3 Treatment

The treatment of diaphyseal femur fractures has developed over time, with various treatment options available, including both non-operative and operative. This section presents two common operative treatment options used to fix diaphyseal femur fracture.

#### 2.3.3.1 Intramedullary Nailing

Intramedullary nailing (IMN) is considered the gold standard for treating femoral shaft fractures (Rudloff and Smith, 2009). The nail is inserted into the medullary canal of the femur and secured at both distal and proximal ends using interlocking screws (Cheung *et al.*,

2004). These screws prevent compression of the fracture fragments and rotational movement. The nails help stabilize the fracture fragments, facilitate load transfer across the fracture site, and maintain the bone's anatomical alignment (Eveleigh, 1995).



**Figure 9.** Two possible starting points in antegrade nailing: (A) Entry point through the piriformis fossa; (B) Entry point through the greater trochanter (Moein *et al.*, 2005).

Nailing can be performed either antegrade (proximal to distal) or retrograde (distal to proximal) (*Intramedullary nailing: Basic technique*, no date). The starting point for retrograde nailing is the centre of the intercondylar notch of the distal femur and 2 to 4 mm anterior to the distal tip of Blumensaat's line (Denisiuk and Afsari, 2023). There are two possible starting points in antegrade nailing: the greater trochanter and the piriformis fossa (Figure 9) (Denisiuk and Afsari, 2023; Medda, Unger and Halvorson, 2023).

The insertion of an intramedullary nail can be performed with or without reaming. Reaming increases the diameter of the medullary canal, which allows the use of a larger diameter nail, thereby providing greater stability to the fixation (Helmig, Kakish and DeCoster, 2022). However, reaming can disrupt blood flow to the bone in the diaphyseal region, which can lead to bone necrosis and the formation of emboli. Reaming can also increase blood loss and longer operative time (Li *et al.*, 2016).

Intramedullary nails bear most of the weight in the early stages of recovery, and as the fracture heals, the load gradually transfers from the nail to the bone, making early weight-bearing within six weeks post-surgery possible (Bhanushali *et al.*, 2022). Intramedullary nails provide angular, rotational, and longitudinal stability (*Intramedullary nailing: Basic technique*, no date). Additional advantages include minimal disruption to the fracture site and surrounding soft tissues, low risk of infection, reduced nonunion rates, small operative scars, early mobilization, and high success rate (Rosa *et al.*, 2019). However, disadvantages include longer operating times, possibility of pulmonary complications due to fat embolism in the venous system, and potential destruction of the intramedullary blood supply (Pairon *et al.*, 2015).

Intramedullary nails are commonly made from titanium alloy and stainless steel (Cheung *et al.*, 2004). Both materials offer significant stability at the fracture site due to their high bending and torsional stiffness. However, this high axial rigidity can lead to a negative effect known as stress shielding, where the nail bears most of the load, causing the femur to become underload. This can result in atrophy and loss of density in the bone surrounding the nail. Over time, this process may result in nail loosening (Samiezadeh *et al.*, 2020).

### **2.3.3.2 Plate Osteosynthesis**

Plate osteosynthesis is a procedure in which femoral shaft fractures are stabilized with plates and screws. It is preferred in specific situations where intramedullary nailing may not be suitable, such as when the fracture location is too proximal or distal, preventing stable and secure locking of the intramedullary nailing. Additionally, osteosynthesis plates are commonly used for certain periprosthetic fractures, femurs with narrow canals, recalcitrant nonunions, or open fractures with vascular injury (Yates and Fountain, 2016; Denisiuk and Afsari, 2023).

Bone plates offer numerous advantages, including high stability, resistance to tension, compression, shear, torsion, and bending forces, rigid fixation, and direct fracture reduction (Li *et al.*, 2020; Miao and Miao, 2023). However, plate osteosynthesis can impair periosteal circulation (Bäcker *et al.*, 2022).

The concept of using screws and plates for fracture fixation was introduced by several European surgeons by the end of the 19<sup>th</sup> century, including Carl Hansmann (1853–1917),

William Arbuthnot Lane (1856–1943), and Albin Lambotte (1866–1956) (Augat and von Rden, 2018). Since then, significant advancements have been made in the materials and design of these plates.

Stainless steel and titanium alloy are commonly used as materials for bone plates (Heyland *et al.*, 2017; Zhang *et al.*, 2022). Key characteristics of these materials include ductility, strength, stiffness, and biocompatibility (Barber *et al.*, 2021). Stainless steel alloys are stiffer than bone and durable to allow healing. They are also ductile enough to allow contouring of the plate without fracture and biocompatible. Type 316L is widely used for bone plates due to its corrosion resistance, better fatigue strength, ductility, and non-magnetic properties (Helguero, Ramrez and Amaya, 2019).

In contrast to stainless steel, titanium more closely matches the modulus of elasticity of bone, providing flexibility that can aid fracture healing in areas requiring more strain for effective healing response (Barber *et al.*, 2021). Titanium has gained significant popularity for load-bearing implants and is the most used material for osteosynthesis plates in Europe. The most frequently used titanium alloy is the Ti–6Al–4V ELI (Extra Low Interstitial). However, due to concerns about the release of aluminium and vanadium ions and their long-term health effects, alternatives such as Ti–6Al–7Nb have been developed (Heyland *et al.*, 2017).

Table 1 shows the mechanical properties of 316L, Ti–6Al–4V ELI, and Ti–6Al–7Nb.

**Table 1.** Mechanical properties of 316L, Ti–6Al–4V ELI, and Ti–6Al–7Nb (Niinomi, 1998; Gervais *et al.*, 2016; Li *et al.*, 2020).

Material	Young’s Modulus [GPa]	Ultimate Tensile Strength [MPa]	Yield Strength [MPa]
316L	193	540-1000	1000
Ti–6Al–4V ELI	112	895-930	795-875
Ti–6Al–7Nb	110-114	900-1050	880–950

PEEK is a promising material for plate osteosynthesis because its strength and elastic modulus are similar to bone, which is believed to help prevent the stress shielding effect. It is particularly beneficial for implants in areas with low mechanical loads (Barth *et al.*, 2022).

Bone plating facilitates the force transmission along the bone, allowing for load transfer and/or load bearing (Egol *et al.*, 2004). It also ensures the mechanical alignment of fracture fragments, stabilizes the fracture zone, and protects it from overloading, ultimately promoting fracture healing process. For an optimal bone healing, the plate must not be too stiff, as this can inhibit callus formation, potentially leading to delayed fracture healing (Mori *et al.*, 2024). Additionally, a plate that is too stiff can result in stress shielding, where the plate bears most of the load instead of the underlying bone tissue (Zhang *et al.*, 2022). This may lead to bone resorption, potentially increasing the risk of re-fracture when the plate is removed (Fice and Chandrashekar, 2012). On the other hand, an excessively flexible plate is proven not to be advantageous for bone healing, as it allows too much axial motion, bending, torsional, or shear motion at fracture site. This can potentially result in delayed union and nonunion (Kandemir, 2018). According to Uthoff, Poitras and Backman (2006), the possible solution to improve fracture healing under plates is to allow micromotion through the fracture site. However, the micromotion must be limited to the axial direction.

The plating can be categorized into two types (Egol *et al.*, 2004; Augat and von Rden, 2018):

- Conventional plating

The plate is compressed onto the surface of the bone by the pressure applied using screws, which engage bicortically in the bone (Figure 10). The friction from this compression enables the transfer of axial loads between the plate and the bone (Augat and von Rden, 2018). A disadvantage of conventional plating is that it can potentially damage the blood supply to the underlying periosteum (Szypryt and Forward, 2009). The criteria for achieving successful osteonal bridging with conventional plating involve maintaining fracture gaps smaller than 0,5 mm and ensuring that the interfragmentary strain remains below 2%. These conditions facilitate primary bone healing, particularly effective for simple transverse fractures (Hak *et al.*, 2010; Augat and von Rden, 2018).

- Locked plating

In this type of plating, the screw head engages in the plate hole, creating a locking mechanism that transfers loads from the bone to the plate (Augat and von Rden, 2018). Locked plating offers angular stability without relying on compression to the bone. This design allows the plate to be positioned slightly away from the bone, which preserves the periosteal blood supply (Figure 10) (Szypryt and Forward, 2009). Compared to conventional plating, the interfragmentary strain in locked plating is typically above 2%, which is essential for stimulating secondary bone healing (Augat and von Rden, 2018).

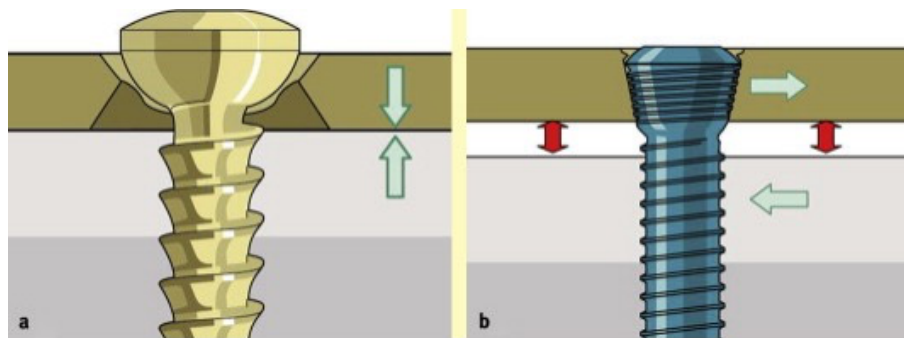


**Figure 10.** Two plating types: Conventional plating, where the plate is compressed onto the surface of the bone (a) and locked plating, where the screw engages in the plate hole and there is no direct bone and plate contact (Szypryt and Forward, 2009).

## 2.4 Preclinical testing for femoral implants

Implants such as intramedullary nails and osteosynthesis plates must undergo preclinical testing to ensure their capacity to withstand functional loading by the patient during the healing process. The testing is normally conducted using a material testing machine, which is a device used to measure the mechanical properties of materials and structures under different loading conditions (Saunders, 2015). In the context of femoral implants, material testing machines help evaluate how both implant materials and bone behave under physiological loading.

According to Schorler *et al.* (2017), there are two approaches for implant testing in the laboratory, namely biomechanical testing and mechanical testing for regulatory purposes. Biomechanical testing involves evaluating a bone-implant construct under anticipated loading conditions that closely resemble physiological scenarios. In biomechanical testing, the test subject is typically a cadaver bone or a bone substitute. The bone is first osteotomized

to simulate a fracture and then stabilized using a fracture fixation method. This approach assesses the strength and stability of plate and screw constructs and is designed for laboratory comparison of bone plates, to analyse different fixation techniques, or for clinical research on healing capabilities after fracture (Schorler *et al.*, 2017).

Mechanical testing for regulatory purposes is performed based on internationally recognized testing standards, such as ISO (International Organization for Standardization) or ASTM (American Society for Testing and Materials) (Schorler *et al.*, 2017). ASTM and ISO are organizations that develop international standards for a variety of industries (*ASTM Fact Sheet - Overview - About Us*, no date; *About ISO*, no date). Mechanical testing measures performance-related mechanical characteristics deemed important for the *in vivo* performance of the implants, such as strength and deformation of the implant under various types of loading conditions, including compression, bending, and torsion. For instance, ASTM F382 and ISO 9585 employ a four-point bending test for the assessment of bone plates (Chen *et al.*, 2024). In mechanical testing, the implant is typically evaluated independently, without being implanted into bone (Schorler *et al.*, 2017).

The following sections discuss important variables for biomechanical testing. The first consideration when conducting biomechanical testing is the type of loading applied to the specimen, followed by the selection of proximal and distal constraints, which is the focus of this study. Next, the choice of specimen is critical—whether to use cadaveric or synthetic bones. Finally, it is essential to identify which outcomes to be measured during testing to effectively address the research questions.

### **2.4.1 Loading**

The choice of loading applied during biomechanical testing includes compression, bending (three- or four-point), and torsion, often combining these loadings to better mimic the real load conditions experienced by bones (Figure 11) (Zhang *et al.*, 2022). In three-point bending test, the bone or implant is positioned on two supports, and an external load is applied to the opposite surface at a point precisely in the middle of the two supports. Four-point bending tests are carried out similarly to the three-point bending tests, except that the external loads are applied at two points that are equidistant from the midpoint (Oksztulska-Kolanek *et al.*, 2015; Khan, 2019). A review by Schorler *et al.* (2016) found that, in

biomechanical testing of the femur, compression is the most commonly applied load, followed by torsion, with bending (three- or four-point) being the least frequently used.

It is important to note that the axial load applied during compression test can cause the femur to experience bending moments along its length. This occurs due to the positioning of the loading point and the bearing used, which introduces a moment arm for the applied axial load (see 3.3 Results, in Chapter I: Finite Element Analysis). A moment arm is defined as the perpendicular distance from the line of action of a force to the centre of rotation (Sherman, Seth and Delp, 2013).

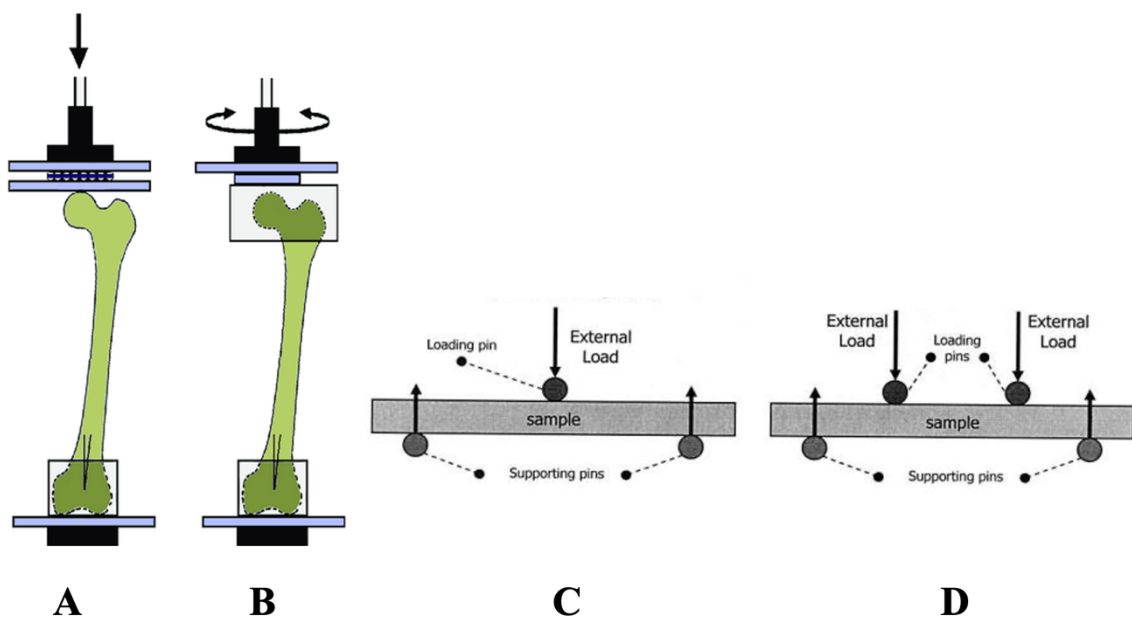


**Figure 11.** Test setups for: A) Compression test; B) Torsion test; C) Three-point bending test; D) Four-point bending test. Figure adapted from (Merriman *et al.*, 2015; Nagler, 2019).

The load can be applied either as single static loads or as cyclic dynamic loads. Static loading generally refers to a slow, continuous application of force, but it can also involve incremental steps of loading and repeated elastic cycles to achieve a steady state of behaviour. This type of loading is typically used to examine the stiffness of a construction. On the other hand, dynamic loading is a term used to describe cyclic loads, which subject the test object to repeated loading with variations in the amount, type, and/or direction of the load. Dynamic cyclic testing is often used to investigate failures that occur due to fatigue, as it closely simulates the real-life stresses and strains that materials and structures endure over time (Olson *et al.*, 2012).

The load applied to a material induces stress. There are five main stress types: axial stress (tensile stress and compressive stress), shear stress, bending stress, and torsional stress (Böge, 2011; Moore and Booth, 2015). Based on the loading condition of the femur during gait (see 2.5 Femoral Loading during Gait), this study focuses only on axial and bending stresses.

Axial stress is caused by an axial load, which can either be tensile or compressive, attempting to stretch or compress the material. Tensile stress is positive, while compressive stress is negative (Moore and Booth, 2015). When the line of action of the axial force passes through the centroid of the cross-section, the axial stress is uniformly distributed (Figure 12) (Arndt, Brüggemann and Ihme, 2021). Axial stress can be calculated as:

$$\sigma_{Axial} = \frac{F}{A}$$

where  $F$  is the axial force and  $A$  is the cross-sectional area (Hulse and Cain, 1991b).

Bending stress arises due to bending moments acting on the structure. These moments induce compressive stresses on the inner side of the bend and tensile stresses on the outer side (Figure 12). Between these two sections lies a region called the neutral axis, where there is no tension or compression (Baar, 2022). The further a point is from the neutral axis, the higher the compressive or tensile stress (Hulse and Cain, 1991a). Bending stress can be calculated as:

$$\sigma_{Bending} = \frac{M \cdot y}{I}$$

where  $M$  is the bending moment,  $y$  is the distance from the neutral axis, and  $I$  is the moment of inertia. The moment of inertia  $I$  is influenced by the shape of the body, the distribution of its mass in space, and the position and orientation of the axis of rotation (Harten, 2009).

The moment of inertia  $I$  for a point of mass  $m$  can be calculated as (Davidovits, 2013):

$$I = m \cdot r^2$$

where  $r$  is the distance to the axis of rotation.

For an object consisting of multiple mass points  $m_i$ , the moment of inertia  $I$  can be calculated as (Arfken *et al.*, 1984):

$$I = \sum_i m_i \cdot r_i^2$$

Where  $r_i$  represents the distances of each mass point from the axis of rotation.

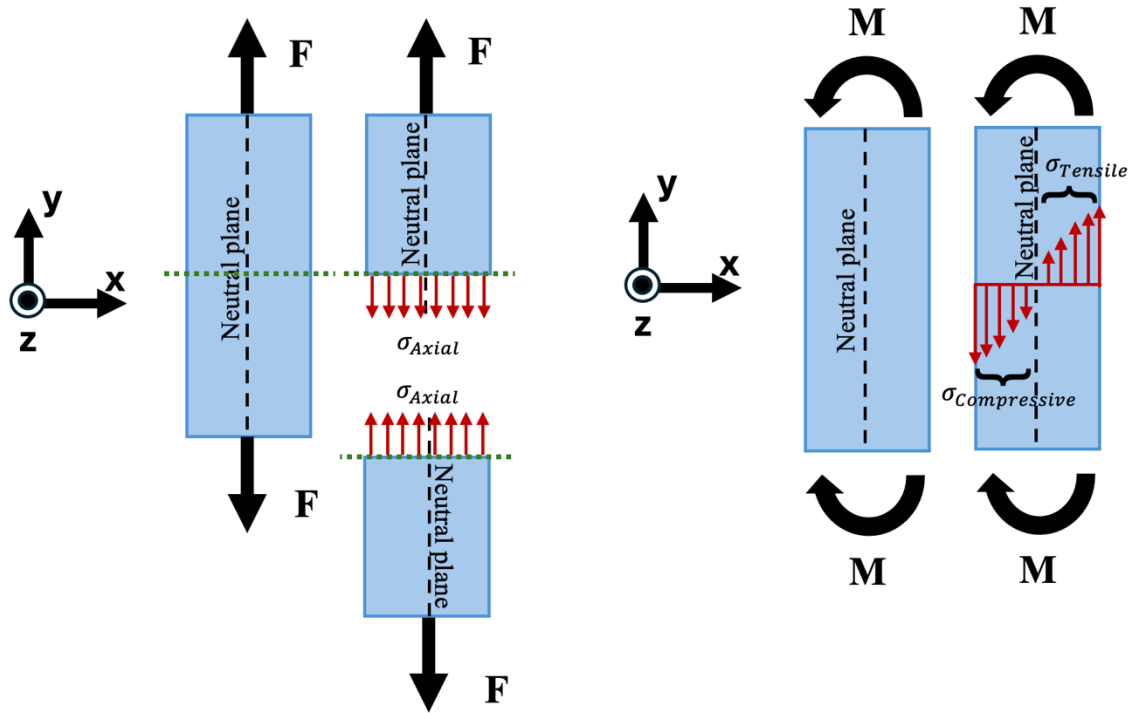


**Figure 12.** Stress distribution based on different loadings: Axial force ( $F$ ) leads to axial stress ( $\sigma_{Axial}$ ) (left) and bending moment ( $M$ ) leads to bending stress, which is a combination of compressive stress ( $\sigma_{Compressive}$ ) and tensile stress ( $\sigma_{Tensile}$ ) (right).

## 2.4.2 Proximal and Distal Constraints

In the majority of implant testing studies, a vertical uniaxial testing machine is used to apply load to the proximal femur. In these tests, muscles are less commonly incorporated. However, variations arise in the displacement constraints at the proximal and distal ends of the bone, as well as in its angle relative to the vertical axis of the testing machine (O'Connell *et al.*, 2018; Wähnert *et al.*, 2020; Konya *et al.*, 2021; Pierret *et al.*, 2022; Wisanuyotin *et al.*, 2023).

When observing the biomechanical test setup in 2D, the most basic movements involve horizontal translation ( $d_x$ ), vertical translation ( $d_y$ ), and rotation around an axis perpendicular to the 2D plane ( $r_z$ ) (Figure 13). Consequently, the most basic displacement constraints involve restricting horizontal translation ( $d_x$ ) or rotation around an axis perpendicular to the 2D plane ( $r_z$ ).

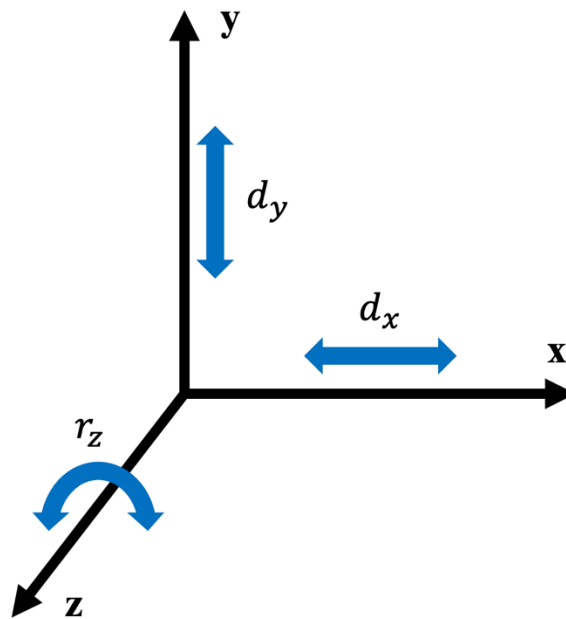


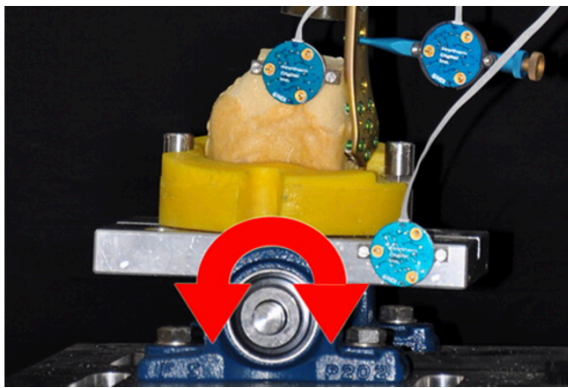
Figure 13. Coordinate system and the basic movement in 2D.

The system must remain stable under the applied force, meaning it must be prevented from moving uncontrollably. Stability ensures the system can withstand applied forces without collapsing or experiencing unintended displacements (Villwock and Hanau, 2020). A system is considered stable if the following conditions are met:

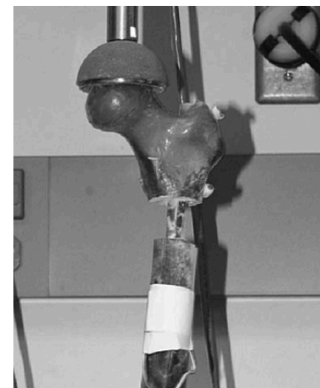
- **Vertical translation ( $d_y$ ):** One end of the system should have restricted vertical movement to prevent uncontrolled displacement along the vertical axis. In biomechanical tests, force is typically applied vertically to the proximal femur. Therefore, the system should allow vertical translation at the proximal end while restricting vertical translation at the distal end.

- **Horizontal translation ( $d_x$ ):** Horizontal translation must be restricted at one or both ends of the system. Without this restriction, the system can slide to infinity, causing instability.
- **Rotation around an axis perpendicular to the 2D plane ( $r_z$ ):** Rotation around an axis perpendicular to the 2D plane can either be restricted at one end, restricted at both ends, or left unrestricted, depending on the test setup.

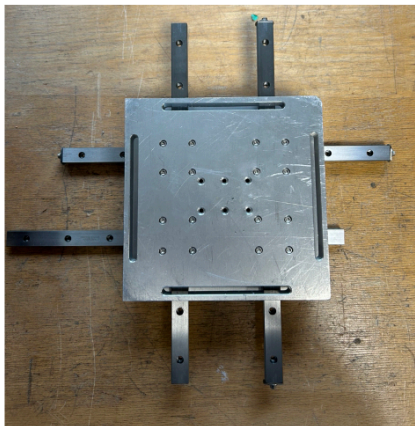
The following are examples of bearing types commonly used in biomechanical testing of the femur to decouple the degrees of freedom mentioned above ( $d_y$ ,  $d_x$ , and  $r_z$ ) (Figure 14):



Tilting table



Cup simulating the acetabulum



X-Y table



Cardan joint

**Figure 14.** Examples of bearing types used in biomechanical testing. Figure adapted from (Grisell, Moed and Bledsoe, 2010; D. Wähnert *et al.*, 2013).

- Cup simulating the acetabulum: Often used to apply force to the proximal end of the femur, allowing for vertical translation ( $d_y$ ) and rotation around the z-axis ( $r_z$ ) in 2D (Wright *et al.*, 2022).
- X-Y table: Allows translation along the x-axis ( $d_x$ ) while restricting translation along the y-axis ( $d_y$ ) and rotation around the z-axis ( $r_z$ ). When observing movement in 3D, this bearing also allows translation along the z-axis ( $d_z$ ) (Wendler *et al.*, 2022).
- Tilting table (also known as seesaw table): Allows rotation around the z-axis ( $r_z$ ) while restricting translations along both the x-axis ( $d_x$ ) and y-axis ( $d_y$ ) (Wähnert *et al.*, 2020).
- Cardan joint (also known as universal joint): Allows rotation around the z-axis ( $r_z$ ) while restricting translations along the x-axis ( $d_x$ ) and y-axis ( $d_y$ ). When observing movement in 3D, this bearing also allows rotation around x-axis ( $r_x$ ) (Steffensmeier *et al.*, 2022).

### 2.4.3 Specimen

The specimens used for testing can be either cadaveric bones or synthetic bones. Cadaveric bones closely replicate the actual biological and mechanical properties of human bones, providing a more accurate representation of clinical conditions. However, there is significant interspecimen variability in factors such as bone density, size, and mechanical properties, making it challenging to obtain consistent results. This variability often requires larger sample sizes to achieve statistically significant differences in implant performance (O'Neill *et al.*, 2012). Additionally, proper handling, storage, and preparation are critical when using cadaveric bones, as factors like thawing time, temperature, and moisture content can affect the bone's mechanical properties (Olson *et al.*, 2012).

On the other hand, synthetic bones offer uniformity in size, shape, and mechanical properties, reducing variability and allowing for more controlled and repeatable experiments. They can be engineered to simulate both normal and osteoporotic bones, enabling testing of different bone conditions. While synthetic bones can mimic certain properties of real bones, they may not fully replicate the complex anatomical and mechanical characteristics of human bone, such as variability in bone density and microstructure (Olson *et al.*, 2012).

#### 2.4.4 Outcomes

Many different outcomes can be measured during biomechanical testing. Typical outcome variables include stiffness, strength, and ultimate strength (Schorler *et al.*, 2016). Stiffness refers to a system's ability to resist changes in geometry and shape when subjected to external forces (Rivin, 2010). Strength is defined as the maximum load a system can withstand without failing (Leckie and Bello, 2009). Ultimate strength, on the other hand, is the maximum stress a material can sustain before starting to fail (Turner, 2006).

When a load is applied to an implant during testing, the implant undergoes deformation. Initially, it experiences elastic deformation, where the deformation is temporary and reversible; meaning, once the load is removed, the implant returns to its original shape. However, if the stress on the implant exceeds the yield strength of the material, the implant undergoes plastic deformation, resulting in permanent and irreversible changes (Pfeifer, 2009). Therefore, both elastic and plastic deformations are often measured during biomechanical testing to provide insight into the material's performance under stress and its durability in real-world applications (Schorler *et al.*, 2016).

The loads applied during testing are also the typical outcome variables in biomechanical testing, such as peak load, failure load, and yield load (Schorler *et al.*, 2016). Peak load is the maximum load applied during testing (Lin *et al.*, 2017; Ito *et al.*, 2021). According to Wendler *et al.* (2022), failure load is defined as the force to initiate fracture of the femur or failure of the fixation used. Yield load is the load at which the material enters the plastic region and the deformations become permanent (Roe, 2018).

Motion at the fracture site plays a crucial role in the healing process, as it generates strain and stress in the surrounding tissue, which act as signals that regulate the repair process of the fracture (Augat *et al.*, 2006). Limited amount of movement at the fracture site can stimulate secondary bone healing (Ghiasi *et al.*, 2017). However, excessive motion increases the cartilage callus size, which can lead to disruption of the bone remodelling (Burr, Bellido and White, 2015). Therefore, typical outcome variables in biomechanical testing include parameters like displacement, interfragmentary motion, intercycle fracture motion, deformation angle, and fracture gap movements (Schorler *et al.*, 2016). These variables help assess the mechanical environment and healing potential at the fracture site.

Another typical outcome variables include screw angulation, cycles to failure, subsidence, torque to failure, range of motion, and survival rate (Schorler *et al.*, 2016).

There is still a lack of standardization in the variables involved in biomechanical testing, including the applied loading (Schorler *et al.*, 2016; Wang *et al.*, 2019). In some implant testing, researchers aim to apply loads that resemble single-legged stance during gait to the bone-implant construct (Lever *et al.*, 2010; O'Connell *et al.*, 2018; Wisanuyotin *et al.*, 2023).

## **2.5 Femoral Loading during Gait**

The type of loading applied during preclinical testing is crucial, particularly in biomechanical testing where the load closely resembles physiological scenarios, such as walking (Schorler *et al.*, 2017). As mentioned before, many biomechanical tests employ loading protocols that aim to simulate gait, which will be discussed in this section (Karakasli, Satoğlu and Havitçioğlu, 2015; O'Connell *et al.*, 2018; Wisanuyotin *et al.*, 2023). Gait refers to the manner of walking (Kharb *et al.*, 2011). The walking pattern is studied as a gait cycle, which is defined as the sequence from one heel strike to the next heel strike of the same foot (Gage, DeLuca and Renshaw, 1996). The gait cycle is divided into two main phases: the stance phase and the swing phase. The stance phase, when the foot is on the ground, accounts for about 60% of the cycle and involves initial contact (heel strike), loading response (weight absorption), mid-stance (centre of gravity over the foot), terminal stance (heel lift), and pre-swing (toe-off). The swing phase, when the foot is in the air, makes up the remaining 40% and includes initial swing (foot lift-off), mid-swing (foot passing under the body), and terminal swing (preparing for the next heel strike) (Whittle, 2007; Kharb *et al.*, 2011; Björnsdóttir, 2014).

Femoral loading refers to the mechanical forces applied to the femur during various activities such as walking, running, jumping, or any weight-bearing activities. These forces can include axial load, shear load, torsional load, and bending load. There has been ongoing debate in the literature regarding how the femur is loaded during gait, with increasing evidence suggesting that the body has mechanisms to limit bending as well as stress, resulting in primarily compressive stress and strain distribution within the femur. This concept has been extensively reviewed by Pauwels (1980).

Pauwels (1980) analysed the stress on the lower limb during the single-limb support period of gait by initially modelling the lower limb as a simple column, then progressively incorporating ligaments and muscles to the model.

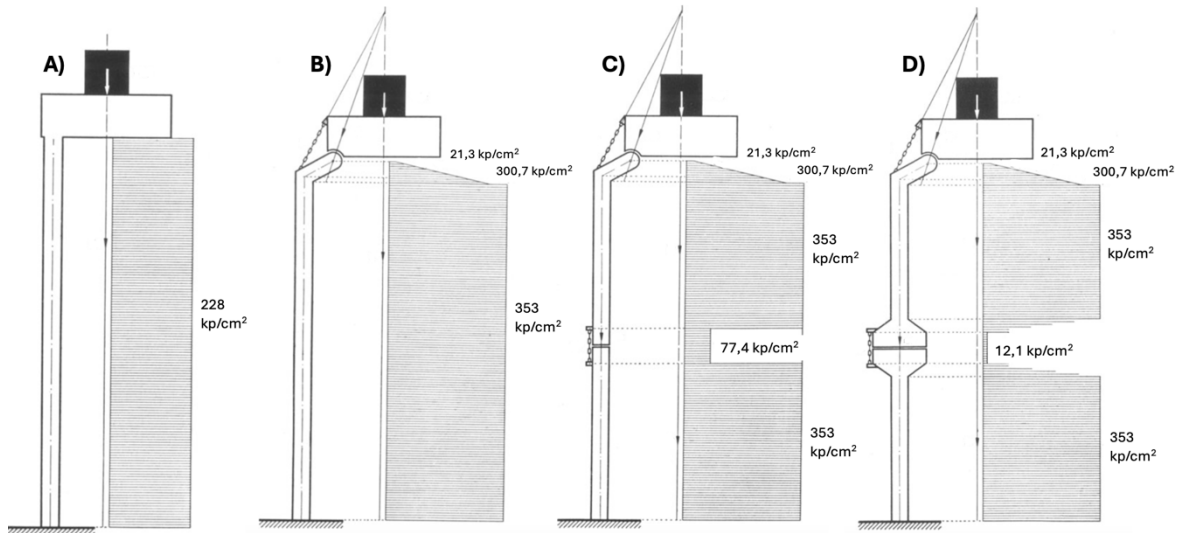


**Figure 15.** The first four models of the lower limb in the coronal plane developed by Pauwels to demonstrate various structures in the skeleton that reduce stress on the bone. The graph next to the column shows the stress experienced by the column and the stress value in  $\text{kp/cm}^2$ . First, the limb was modelled as a single column (A). Next, he added the hip joint and the abductors (B). Then, he added the knee joint and the lateral ligament (C). In the fourth model, he enlarged the articulation to match the width of the knee joint (D). Figure adapted from (Pauwels, 1980).

He initially demonstrated the limb in the coronal plane as a single column (Figure 15A). As shown in the graph next to the column, the stress remained constant from top to bottom. Then, he introduced the hip joint and a tension chain representing the abductors (Figure 15B). As a result, the upper part of the column experienced lower stress and smaller bending effect due to the shorter lever arm of the resultant compressive force. However, the stress increased in the lower portion of the column. Next, he added the knee joint and the lateral ligament (Figure 15C), which acted as a tension band, eliminating bending at the joint and resulting in pure compression. The articulation was enlarged to match the width of the knee joint (Figure 15D), which reduced both compressive stress at the joint and the tensile stress in the lateral ligament.

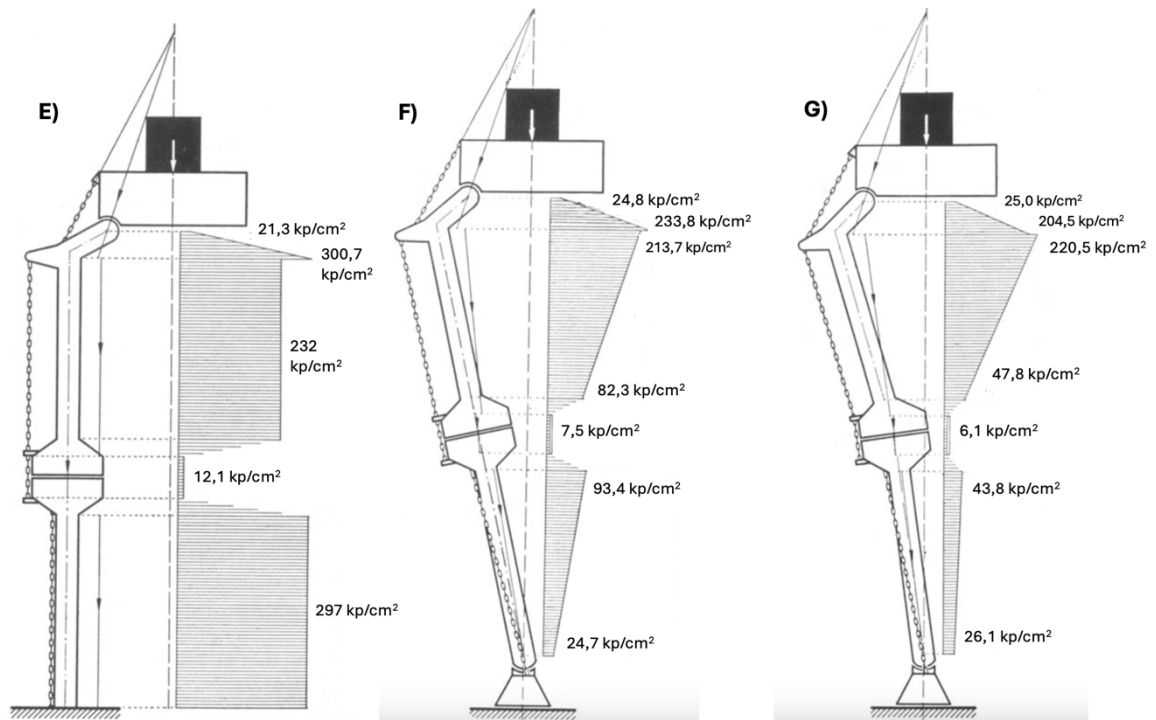


**Figure 16.** The last three models of the lower limb in the coronal plane developed by Pauwels to demonstrate various structures in the skeleton that reduce stress on the bone. The graph next to the column shows the stress experienced by the column and the stress value in  $\text{kp/cm}^2$ . He added the iliotibial band, the greater trochanter, and the flexor muscles (E). Then, an articulation was added to the lower end of the column and the column was inclined to the left around this joint (F). In the final model, he added an angulation at the middle joint (physiological valgum) (G). Figure adapted from (Pauwels, 1980).

Subsequently, he added the iliotibial band, the greater trochanter, and the flexor muscles (Figure 16E). The iliotibial band reduced the stress in the upper part of column, while the stress in the lower part of the column was reduced by the flexor muscles. The greater trochanter was added to enhance the counter bending effect of the chain. Finally, an articulation was added to the lower end of the column and the column was inclined to the left around this joint so that the load's line of action passed through the centre of the joint's rotation (Figure 16F). This inclination reduced stress on the column, particularly compressive stress in the middle of the joint. Additionally, an angulation at the middle joint (physiological valgum) further reduced stress on both the column and the middle joint (Figure 16G) (Pauwels, 1980).

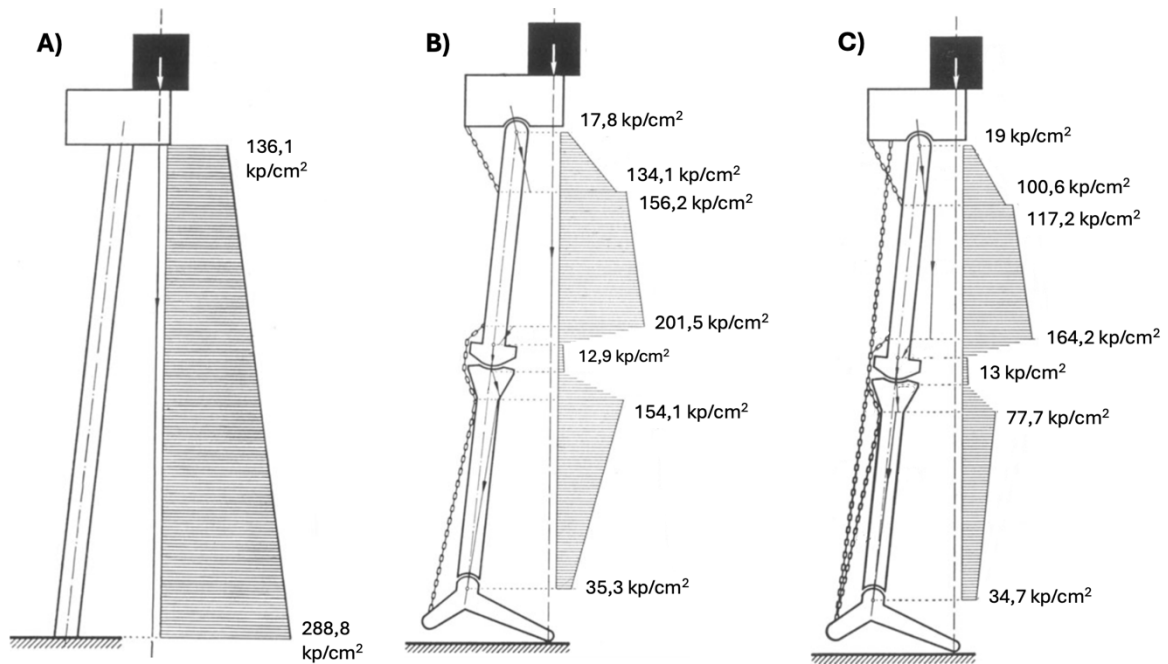


**Figure 17.** The first three models of the lower limb in the sagittal plane developed by Pauwels to demonstrate various structures in the skeleton that reduce stress on the bone. The graph next to the column shows the stress experienced by the column and the stress value in kp/cm<sup>2</sup>. First, the limb was modelled as an inclined column (A). Then, he introduced three joints and a monoarticular muscle (B). Next, he added biarticular muscles (C). Figure adapted from (Pauwels, 1980).

In the sagittal plane, Pauwels (1980) first modelled the lower limb as an inclined column. The stress progressively increased from top to bottom (Figure 17A). Then, three joints were introduced, each stabilized by a single chain (representing a monoarticular muscle) acting as a tension band (Figure 17B). These chains reduced stress in the portions of the column they spanned, progressively towards the joints. At the level of the joints, bending was eliminated, leaving only compressive stress. Next, two additional chains (representing biarticular muscles) were added (Figure 17C), further reducing stress on both the tibia and femur.

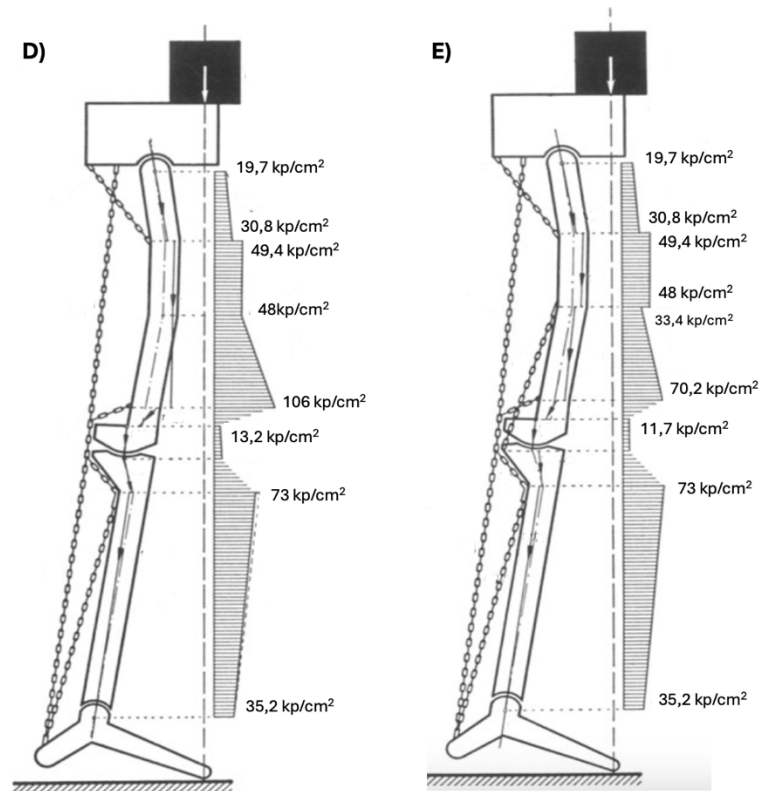


**Figure 18.** The last two models of the lower limb in the sagittal plane developed by Pauwels to demonstrate various structures in the skeleton that reduce stress on the bone. The graph next to the column shows the stress experienced by the column and the stress value in  $\text{kp/cm}^2$ . He bowed the femur forward and altered the shape of the articulation between the femur and tibia (D). In the last model, the short head of the biceps femoris was added (E). Figure adapted from (Pauwels, 1980).

By bowing the femur forward and altering the shape of the articulation between the femur and tibia (Figure 18D), the bending stress was minimized. Finally, the addition of another chain, spanning the lower part of the upper section including the joint (representing the short head of the biceps femoris) (Figure 18E), further reduced the stress (Pauwels, 1980).

Pauwels' (1980) findings revealed that muscles and ligaments play a crucial role in reducing bending stress in both the coronal and sagittal planes, therefore protecting bones from excessive bending moments. Acting as tension bands, muscles and ligaments help limit bending moments but increase compressive forces on bones (Pauwels, 1980).

Munih, Kralj and Bajd (1992) also confirmed this theory, showing that muscles help limit bending moments in the sagittal plane of the lower extremity. By measuring muscle activity in five subjects and applying a muscle optimization algorithm, they calculated the bending moments in the femur and tibia during two standing postures. Their results showed that the

muscles, that were active, significantly reduced the overall bending moment caused by joint reaction forces.

After presenting evidence that suggests a mechanism exists to limit bending and stress in the femur, the following highlights evidence indicating that the femur is primarily loaded in compression.

Taylor *et al.* (1996) conducted a study composed of two parts: a finite element analysis (FEA) and a radiological study. The study aimed to test the hypothesis that the femur is primarily loaded in compression. The finite element analysis revealed that a compressive stress distribution in the diaphyseal femur is achievable. While muscle forces such as those from the abductors, iliotibial tract, and iliopsoas helped reduce bending moments, they did not eliminate them entirely. The result from the FEA also showed negligible deflection of the femoral head under compressive loading. This was confirmed by the radiological study, which showed an average medial deflection of 1,25 mm and an average vertical deflection of 1,5 mm during one-legged stance, strongly supporting the idea that the femur is predominantly loaded in compression.

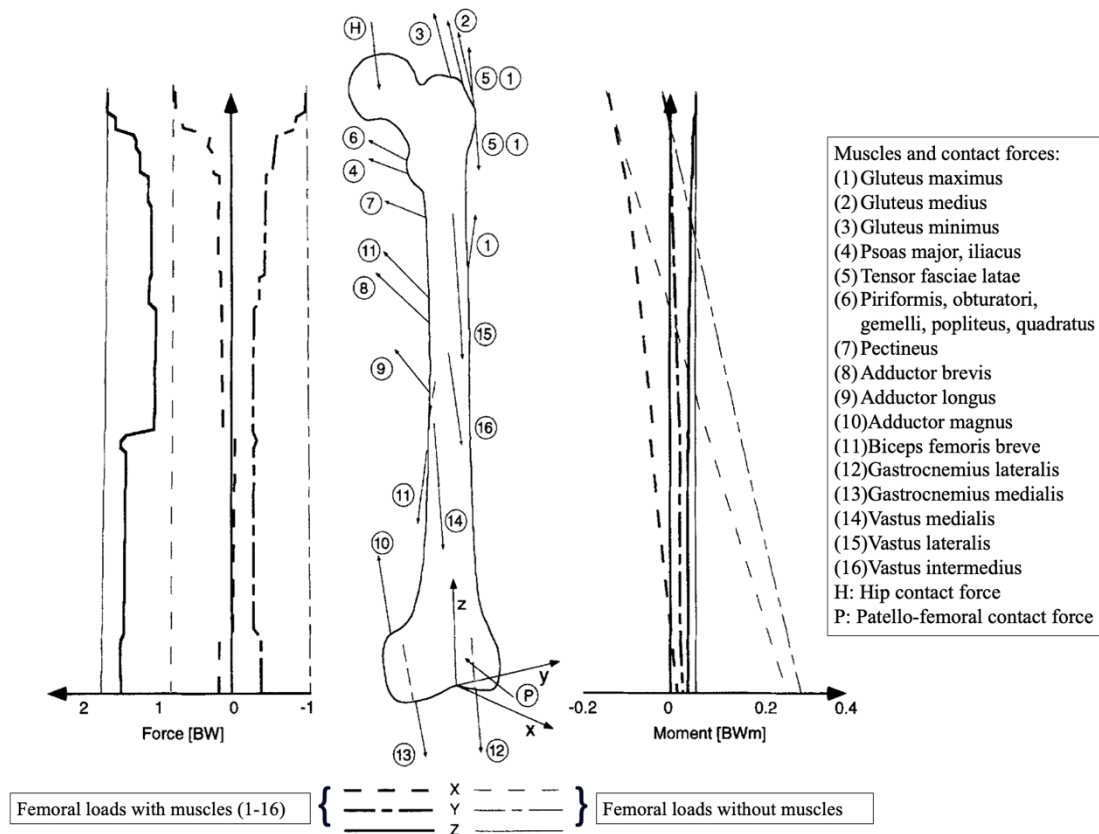


**Figure 19.** The model developed by Duda, Schneider and Chao (1997) to calculate the internal loads of the femur. The results of their research are shown in two graphs: the graph on the left shows the internal forces along the length of the femur and the graph on the right shows the internal moment along the length of the femur. The thin lines in both graphs represent the femoral loads with only hip contact considered (without muscles). Figure adapted from (Duda, Schneider and Chao, 1997).

Another study that demonstrated the femur is mainly loaded in compression during gait is the study by Duda, Schneider and Chao (1997). They developed a three-dimensional model to calculate the internal loads on the femur, taking into account all thigh muscles, body weight, and contact forces at the hip, patellofemoral, and knee joints. The thigh muscles included in this study can be seen in Figure 19. They found that muscle activity causes the internal loads in the femur to decrease from proximal to distal at the hip and from distal to proximal at the knee, indicating the significant role muscles play in balancing the femoral load. The femur is primarily subjected to axial loading rather than bending, with the highest shear forces occurring at its proximal and distal ends (Figure 19). During the gait cycle, the bending moments alternate, rather than being one-sided.

### **3 Chapter I: Finite Element Analysis**

This chapter of the thesis focuses on the finite element analysis (FEA) and analytical modelling to investigate the effects of proximal and distal displacement constraints on internal forces and moments, and the resulting stresses in intact bone (femur), a lateral plate, and an intramedullary nail. The first section provides a general overview of finite element analysis. Following that, the methodology is detailed, including an analysis of the proximal and distal constraints employed, along with an explanation of both the finite element model and the analytical model used. The subsequent section presents the results, where the internal forces, moments, and stresses in the bone (femur), lateral plate, and intramedullary nail are illustrated in graphs. This chapter ends with a discussion of the findings.

#### **3.1 Finite Element Analysis – an Overview**

Before discussing how finite element analysis was used to address the aim of the study, it is essential to outline the fundamental concepts of finite element analysis and the steps involved in the FEA.

Finite Element Analysis (FEA) is a computational method used to predict how structures react to different forces. It works by breaking down a complex shape into smaller, simpler parts called elements. The behaviour of these elements can be then easily calculated with basic (mechanic) formulas by computer systems. These elements are connected at points known as nodes. Together, these nodes and elements form a grid-like network called a mesh. This mesh represents the structure's shape and is programmed with the material properties, helping to predict how the structure will behave under various conditions. In orthopaedics, FEA is often used to predict how implants will react to various loads, compare different implants or fracture fixation models, and analyse the biomechanics of bones in human and animals. Additionally, it facilitates the investigation of mechanical properties such as structural modulus, stress distribution within complex structures, and compressive strength (Sriekha and Bashetty, 2010; Welch-Phillips *et al.*, 2020).

FEA involves three primary steps: model creation, solution phase, and validation. The process begins by generating a geometric model that represents the structure of interest. This can be accomplished using various techniques, such as laser scans, CAD software, MRI, or

CT scans. The geometric model is then converted into a mesh of finite elements. The type of elements used depends on the model's dimensions (e.g., triangles and rectangles for 2D models or tetrahedrons and prisms for 3D models). These elements are assigned material properties (e.g., shear modulus, Poisson's ratio, and Young's modulus) and mechanical properties, which depend on the geometry and material properties of the material (Panagiotopoulou, 2009).

Next, boundary conditions are applied (Panagiotopoulou, 2009). Boundary conditions are applied to the model to determine how it interacts with its surroundings or responds to forces. They control the nodal degrees of freedom (DOFs), specifying what motions or reactions are allowed or restricted at the nodes (Yang, 2018). There are two types of boundary conditions: essential and natural boundary conditions (Steinke, 2010). The essential boundary condition, also known as the displacement boundary condition, defines movement constraints on the model. Natural boundary conditions, or force boundary conditions, specify the forces or moments acting on the model (Grabowski *et al.*, 2022).

During the solution phase the finite element software calculates the resultant deformation of the nodal displacements and the consequent strain and stress values. The results are often displayed as numerical values and/or color-coded projections on the model geometry (Panagiotopoulou, 2009).

To achieve both accuracy and efficiency in the simulation results, it is necessary to perform a mesh convergence analysis on the finite element model (Wang, 2014). Mesh convergence involves refining the mesh and analysing its impact on the results.

To validate a FEA model, its results can be compared with experimental data from in vivo or in vitro studies. This validation ensures that the model accurately replicates the behaviour of the actual structure under similar conditions. While, this step is highly recommended, it may be considered optional (Panagiotopoulou, 2009).

An important consideration when conducting finite element analysis is large deformations. Large deformations refer to situations in which the structure deforms significantly due to the applied loads, making the original stiffness and geometry are no longer sufficient for accurate calculations. This occurs when loads and stiffness change with deformation,

resulting in calculations that must be performed iteratively to account for the continuous changes (Gebhardt, 2014).

## **3.2 Methodology-Finite Element Analysis and Analytical Modelling**

This section begins by explaining the selection process for the proximal and distal constraint combinations used in the finite element analysis. It then describes the finite element models employed in the study, followed by an overview of the analytical modelling approach used to address the study's aim.

Table 2 presents the possible combinations of proximal and distal displacement constraints in a 2D setup and evaluates their stability. For an explanation of stability and the coordinate system used, refer to 2.4.2 Proximal and Distal Constraints.

**Table 2.** Possible constraint combinations in 2D and their stability. The highlighted rows indicate the combinations simulated in the finite element analysis. “0” indicates that no movement is allowed along the axis, while “Free” indicates that movement along the axis is permitted.

No.	Proximal			Distal			Stability
	$d_y$	$d_x$	$r_z$	$d_y$	$d_x$	$r_z$	
1	Free	0	0	0	Free	Free	stable
2	Free	0	0	0	0	Free	stable
3	Free	0	0	0	0	0	stable
4	Free	0	0	0	Free	0	stable
5	Free	0	Free	0	Free	0	stable
6	Free	0	Free	0	0	0	stable
7	Free	0	Free	0	0	Free	stable
8	Free	0	Free	0	Free	Free	unstable
9	Free	Free	0	0	0	Free	stable
10	Free	Free	0	0	0	0	stable
11	Free	Free	0	0	Free	0	unstable
12	Free	Free	0	0	Free	Free	unstable
13	Free	Free	Free	0	0	0	stable
14	Free	Free	Free	0	Free	0	unstable
15	Free	Free	Free	0	0	Free	unstable
16	Free	Free	Free	0	Free	Free	unstable

Combinations 9 and 1 produce identical loading, as well as combinations 10 and 4, and combinations 13 and 5. This is because the location of the horizontal displacement constraint ( $d_x$ )—whether at the proximal or distal end—does not influence the overall loading. Finite element analysis was performed for combinations 1, 2, 3, 4, 5, 6, and 7.

Based on section 2.4.2 Proximal and Distal Constraints and the stability analysis of the possible proximal and distal constraint combinations in 2D (Table 2), twelve models were

developed, as shown in Figure 20. Each model has a different configuration of proximal and distal constraints, angular orientation of the bone, or point of loading. Table 3 shows the set of constraints applied to each model, detailing the proximal and distal constraints for  $d_x$ ,  $d_y$ , and  $r_z$ . All finite element analyses were executed using ANSYS 2024 R1 Student Version.

Finite element analysis (FEA) was performed to determine the distal reaction forces ( $F_{1x}$ ,  $F_{1y}$ ,  $M_{1z}$ ) (Figure 22) of the bone (femur) and the normal stress distribution along both the bone (femur) and lateral plate for the twelve models (Figure 20, Table 3).

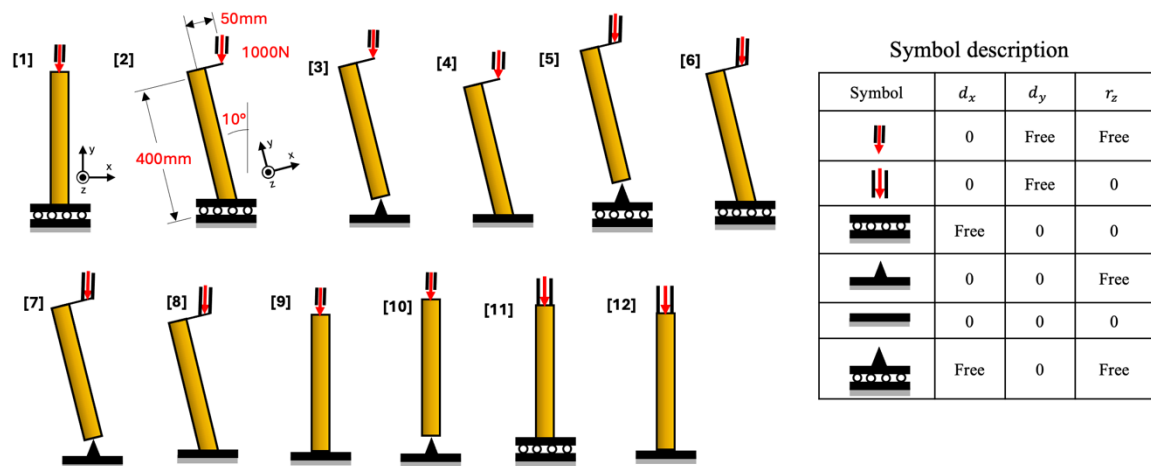


**Figure 20.** Twelve models developed for the study. The femur in models 1, 9, 10, 11, and 12 was oriented vertically, while in models 2 to 8 was oriented at a 10° angle. The coordinate system was aligned with the bone orientation. When the bone is vertical (as in models 1 and 9 to 12), the coordinate system is also vertical, as shown in model 1. However, in models where the femur is tilted 10° (models 2 to 8), the coordinate system is tilted 10° accordingly, as shown in model 2. The table next to the models shows the bearing symbols and their respective movements. “0” indicates that no movement is allowed along the axis, while “Free” indicates that movement along the axis is permitted.

**Table 3.** Displacement constraint sets for the twelve models.

Model No.	Proximal Constraints			Distal Constraints		
	$d_x$	$d_y$	$r_z$	$d_x$	$d_y$	$r_z$
1	0	free	free	free	0	0
2	0	free	free	free	0	0
3	0	free	free	0	0	free
4	0	free	free	0	0	0
5	0	free	0	free	0	free
6	0	free	0	free	0	0
7	0	free	0	0	0	free
8	0	free	0	0	0	0
9	0	free	free	0	0	0
10	0	free	free	0	0	free
11	0	free	0	free	0	0
12	0	free	0	0	0	0

First, the femur was modelled as a tube with an outer diameter of 30 mm, an inner diameter of 20 mm, and a length of 400 mm (Figure 21). The typical length of the human femoral shaft ranges from approximately 392 mm to 422 mm (Polguy *et al.*, 2013). A length of 400 mm was chosen for the model as it represents the midpoint of this range. The outer diameter of the human femoral mid-diaphysis is about 30 mm, which was used as the model's outer diameter (Pierre *et al.*, 2010). Since the exact inner diameter of the human femoral mid-diaphysis was unavailable, 20 mm was chosen arbitrarily.

The material assigned to the model was cortical bone ( $E = 1,7 \cdot 10^{10}$  Pa) ('Ansys 2024 R1 Student', 2024). The force exerted on the hip joint during walking ranges from approximately 2,4 to 3 times an individual's body weight (Bergmann, Graichen and Rohlmann, 1993; Bergmann *et al.*, 2001). The applied axial force was set at 1000 N, simulating the weight of a small person weighing approximately 30-40 kg.

In biomechanical testing, axial force can be applied either directly to the femur axis or to the femoral head. For models 1, 9, 10, 11, and 12, the force was applied directly to the femur axis. In the remaining models (models 2 to 8), the femur was angled at 10°, and the force was applied 50 mm from the femur axis to simulate the force being applied at the femoral head. Since the exact distance between the femoral shaft axis and the femoral head was unavailable, 50 mm was selected arbitrarily. The direction of hip contact force in the frontal plane during dynamic activities—such as slow walking, normal walking, fast walking, ascending and descending stairs, sitting down, standing up, and knee bends—ranges between 12° and 16°. During single-legged standing, the angle is approximately 7° (Bergmann *et al.*, 2001). The 10° angle was selected as it represents the midpoint of this range.

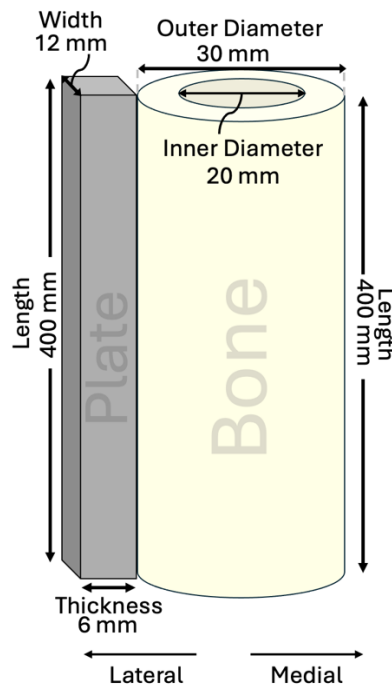


**Figure 21.** Plate placement and dimensions of the bone (femur) and lateral plate.

The plate was modelled with dimensions of 6 mm in thickness, 400 mm in length, and 12 mm in width. It was positioned on the lateral side of the bone (Figure 21). The thickness of 6 mm and width of 12 mm were selected as they represent the approximate size of bone plates commonly used for femur fractures. A length of 400 mm was chosen to simulate a plate covering the full length of the femoral diaphysis. The material assigned to the plate was construction steel, with a Young's modulus ( $E$ ) of  $2 \cdot 10^{11}$  Pa ('Ansys 2024 R1 Student', 2024).

For models 1, 9, 10, 11, and 12, the axial force was applied 18 mm from the plate's axis, simulating the force being applied to the femur axis. In the remaining models (models 2 to 8), the plate was angled at 10°, and the force was applied 68 mm from the plate's axis to simulate the axial force being applied at the femoral head. The applied axial force in all models for simulation of the plate was 1000 N, consistent with the FEA of the bone without the plate or nail.

Finite element analysis (FEA) was performed initially on the bone model alone (without the lateral plate or intramedullary nail) for each constraint set to obtain distal reaction forces ( $F_{1x}$ ,  $F_{1y}$ ,  $M_{1z}$ ) (Figure 22A) and the stress distribution (normal stress) along the bone. Then, FEA was conducted on the lateral plate model (without the bone) separately to obtain the reaction forces at the distal end of the bone ( $F_{1x}$ ,  $F_{1y}$ ,  $M_{1z}$ ) (Figure 22B) and the stress distribution (normal stress) along the plate. No Finite element model or analysis was created or conducted for the intramedullary nail.

The finite element analysis only considered small deformation, and no in vitro experiments using a material testing machine was conducted to validate the finite element model.

The distal boundary reaction forces ( $F_{1x}$ ,  $F_{1y}$ ,  $M_{1z}$ ) obtained from the finite element analysis were used to calculate the internal forces and moments  $F_{2x}(y)$ ,  $F_{2y}(y)$ ,  $M_{2z}(y)$  along the entire length  $y$  of the bone, plate, and nail, using Newton's second law in static equilibrium for a 2D system:

$$\Sigma F_x = m \cdot a_x = 0$$

$$\Sigma F_y = m \cdot a_y = 0$$

$$\Sigma M_z = I \cdot \alpha = 0$$

where:

- $\Sigma F_x$ : Sum of all forces along the x-axis,
- $\Sigma F_y$ : Sum of all forces along the y-axis,
- $\Sigma M_z$ : Sum of all moments along the z-axis,
- $m$ : Mass,

- $a_x$ : Acceleration in x-axis (equal to zero in static equilibrium),
- $a_y$ : Acceleration in y-axis (equal to zero in static equilibrium),
- $I$ : Moment of inertia,
- $\alpha$ : Angular acceleration (equal to zero in static equilibrium).

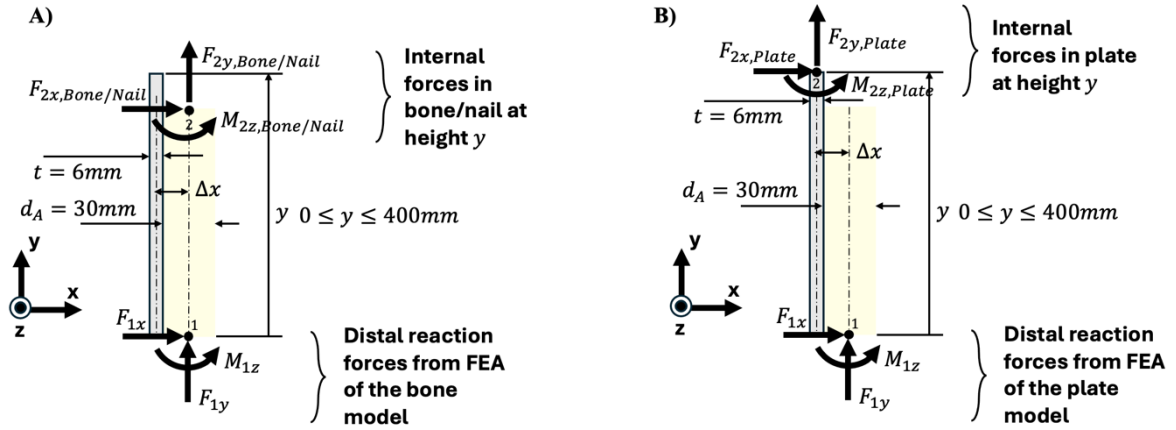


**Figure 22.** Free body diagrams of the bone-plate structure, from which three equations were derived to calculate the internal forces along the x-axis ( $F_{2x}(y)$ ), internal forces along the y-axis ( $F_{2y}(y)$ ), and internal moments along the z-axis ( $M_{2z}(y)$ ). A) shows the free body diagram for calculating  $F_{2x}(y)$ ,  $F_{2y}(y)$ ,  $M_{2z}(y)$  along the bone and nail. B) shows the free body diagram for calculating  $F_{2x}(y)$ ,  $F_{2y}(y)$ ,  $M_{2z}(y)$  along the plate.

From the free body diagrams (Figure 22), three equations were derived:

1. Calculation of the internal forces along the x-axis ( $F_{2x}(y)$ ) using the static equilibrium condition:

$$\sum F_x = m \cdot a_x \text{ (with } a_x = 0, \text{ because static)}$$

$$\sum F_x = 0$$

this gives

$$F_{1x} + F_{2x}(y) = 0 \Rightarrow F_{2x}(y) = -F_{1x}$$

2. Calculation of the internal forces along the y-axis ( $F_{2y}(y)$ ) using the static equilibrium condition:

$$\sum F_y = m \cdot a_y \text{ (with } a_y = 0, \text{ because static)}$$

$$\sum F_y = 0$$

this leads to

$$F_{1y} + F_{2y}(y) = 0 \Rightarrow F_{2y}(y) = -F_{1y}$$

3. Calculation of the internal moments along the z-axis ( $M_{2z}(y)$ ) using the static equilibrium condition:

$$\sum M_z = I \cdot \alpha \text{ (with } \alpha = 0, \text{ because static)}$$

$$\sum M_z = 0$$

this results in

$$M_{1z} + M_{2z}(y) + F_{1x} \cdot y + F_{1y} \cdot \Delta x = 0 \Rightarrow M_{2z}(y) = -M_{1z} - F_{1x} \cdot y - F_{1y} \cdot \Delta x$$

The formulas for calculating  $F_{2x}(y)$ ,  $F_{2y}(y)$ ,  $M_{2z}(y)$  along the plate were as follows:

$$F_{2x,Plate}(y) = -F_{1x,Plate}$$

$$F_{2y,Plate}(y) = -F_{1y,Plate}$$

$$M_{2z,Plate}(y) = -M_{1z,Plate} - F_{1x,Plate} \cdot y - F_{1y,Plate} \cdot \Delta x$$

where  $F_{1x,Plate}$ ,  $F_{1y,Plate}$ , and  $M_{1z,Plate}$  are the distal reaction forces from the FEA of the plate model. In this case,  $\Delta x$  is equal to 18 mm.

The formulas for calculating  $F_{2x}(y)$ ,  $F_{2y}(y)$ ,  $M_{2z}(y)$  along the bone were as follows:

$$F_{2x,Bone}(y) = -F_{1x,Bone}$$

$$F_{2y,Bone}(y) = -F_{1y,Bone}$$

$$M_{2z,Bone}(y) = -M_{1z,Bone} - F_{1x,Bone} \cdot y$$

in this case,  $F_{1x,Bone}$ ,  $F_{1y,Bone}$ , and  $M_{1z,Bone}$  are the distal reaction forces from the FEA of the bone model. When calculating  $M_{2z,Bone}(y)$ ,  $\Delta x$  was set to 0 because  $F_{1y}$  acted directly along the axis of rotation (Figure 22A). The same formulas,  $F_{2x,Bone}(y)$ ,  $F_{2y,Bone}(y)$ , and

$M_{2z,Bone}(y)$ , were also used to calculate  $F_{2x}(y)$ ,  $F_{2y}(y)$ , and  $M_{2z}(y)$  along the nail, as the nail was fixed along the bone's axis.

The stress along the bone, lateral plate, and intramedullary nail was also determined. The stress is the sum of axial stress and bending stress, calculated as:

$$\sigma = \sigma_{Axial} + \sigma_{Bending}$$
$$\sigma(y) = \frac{F_{2y}(y)}{A} + \frac{M_{2z}(y) \cdot k}{I}$$

where:

- $\sigma(y)$ : the stress along the length  $y$
- $F_{2y}(y)$ : the internal forces along the  $y$ -axis
- $A$ : the cross-sectional area
- $M_{2z}(y)$ : the internal moments along the  $z$ -axis
- $I$ : Moment of inertia
- $k$ : distance from the neutral plane

In this study, stress was calculated on both the lateral and medial sides. For the lateral side,  $k$  was taken as a negative value, while for the medial side,  $k$  was positive.

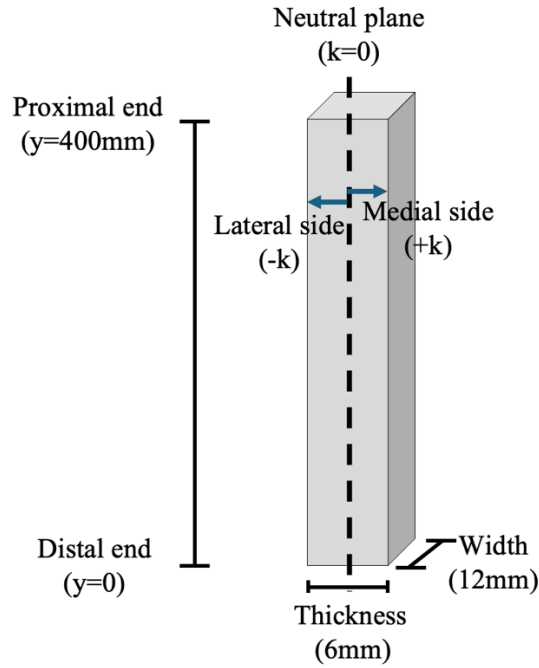


**Figure 23.** Dimensions and geometry of the lateral plate used in this study.

For the plate (Figure 23), which has a rectangular cross-section, the area  $A$  was calculated as:

$$A = \text{Width} \cdot \text{Thickness}$$

And the moment of inertia  $I$  as:

$$I = \frac{\text{Width} \cdot \text{Thickness}^3}{12}$$

The variable  $k$  was calculated as:

$$k = \frac{\text{Thickness}}{2}$$

Then, the stress was calculated as follows:

$$\sigma_{\text{Plate,Lateral side}}(y) = \frac{F_{2y,\text{Plate}}(y)}{\text{Width} \cdot \text{Thickness}} + \frac{M_{2z,\text{Plate}}(y) \cdot \left(\frac{-\text{Thickness}}{2}\right)}{\frac{\text{Width} \cdot \text{Thickness}^3}{12}}$$

$$\sigma_{Plate,Medial\ side}(y) = \frac{F_{2y,Plate}(y)}{Width \cdot Thickness} + \frac{M_{2z,Plate}(y) \cdot \left(\frac{Thickness}{2}\right)}{Width \cdot Thickness^3 \cdot 12}$$

where Width = 12 mm and Thickness = 6 mm.

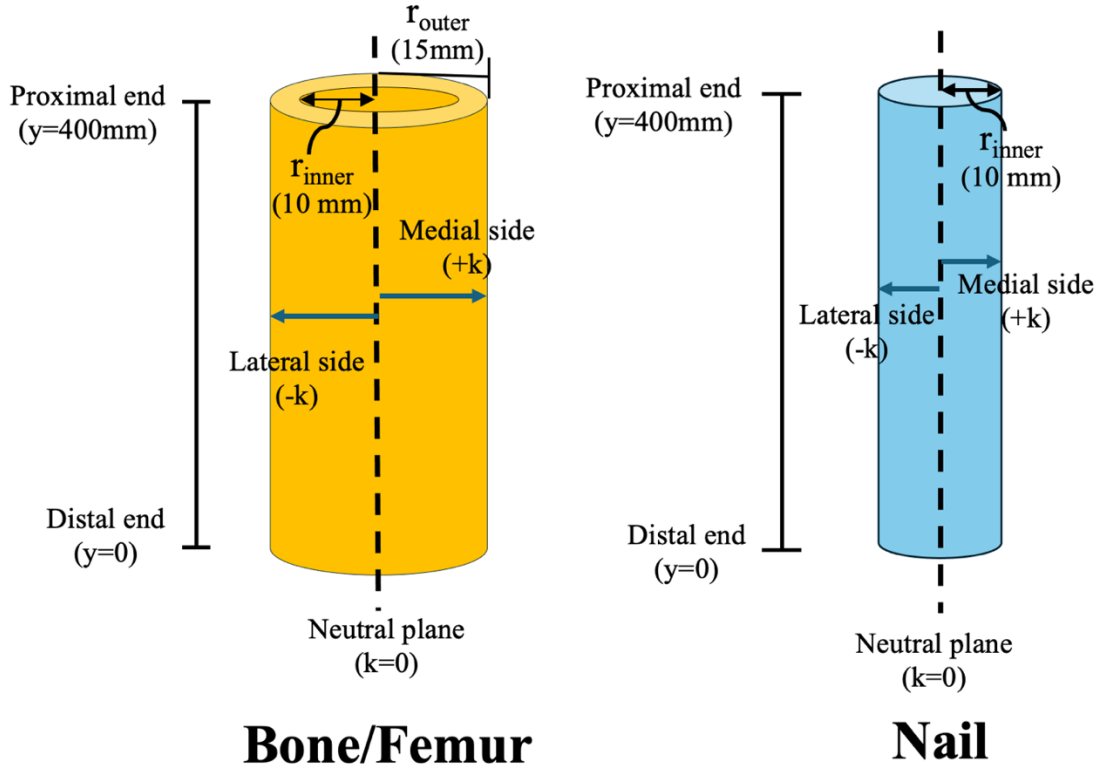


**Figure 24.** Dimensions and geometry of the bone and intramedullary nail used in this study.

For the bone/femur (Figure 24), modelled as a hollow cylinder, the area  $A$  was calculated using:

$$A = \pi \cdot r_{outer}^2 - \pi \cdot r_{inner}^2$$

And the moment of inertia  $I$  as:

$$I = \frac{\pi}{4} (r_{outer}^4 - r_{inner}^4)$$

The variable  $k$  was calculated as:

$$k = r_{outer}$$

The stress was then calculated as follows:

$$\sigma_{Bone,Lateral\ side}(y) = \frac{F_{2y,Bone}(y)}{\pi \cdot r_{outer}^2 - \pi \cdot r_{inner}^2} + \frac{M_{2z,Bone}(y) \cdot (-r_{outer})}{\frac{\pi}{4} (r_{outer}^4 - r_{inner}^4)}$$

$$\sigma_{Bone,Medial\ side}(y) = \frac{F_{2y,Bone}(y)}{\pi \cdot r_{outer}^2 - \pi \cdot r_{inner}^2} + \frac{M_{2z,Bone}(y) \cdot r_{outer}}{\frac{\pi}{4} (r_{outer}^4 - r_{inner}^4)}$$

where  $r_{inner} = 10$  mm and  $r_{outer} = 15$  mm.

For the intramedullary nail (Figure 24), the area  $A$  was calculated as:

$$A = \pi \cdot r_{inner}^2$$

And the moment of inertia  $I$  as:

$$I = \frac{\pi}{4} \cdot r_{inner}^4$$

The variable  $k$  was calculated as:

$$k = r_{inner}$$

Then, the stress was calculated as follows:

$$\sigma_{Nail,Lateral\ side}(y) = \frac{F_{2y,Nail}(y)}{\pi \cdot r_{inner}^2} + \frac{M_{2z,Nail}(y) \cdot (-r_{inner})}{\frac{\pi}{4} \cdot r_{inner}^4}$$

$$\sigma_{Nail,Medial\ side}(y) = \frac{F_{2y,Nail}(y)}{\pi \cdot r_{inner}^2} + \frac{M_{2z,Bone}(y) \cdot r_{inner}}{\frac{\pi}{4} \cdot r_{inner}^4}$$

where  $r_{inner} = 10$  mm.

Then, the absolute maximum stress value was derived from both lateral and medial stresses using the Excel formula =MAX(ABS(stress lateral);ABS(stress medial)). This formula returns the highest absolute value between the two stresses, ensuring that the largest magnitude, regardless of direction, is selected.

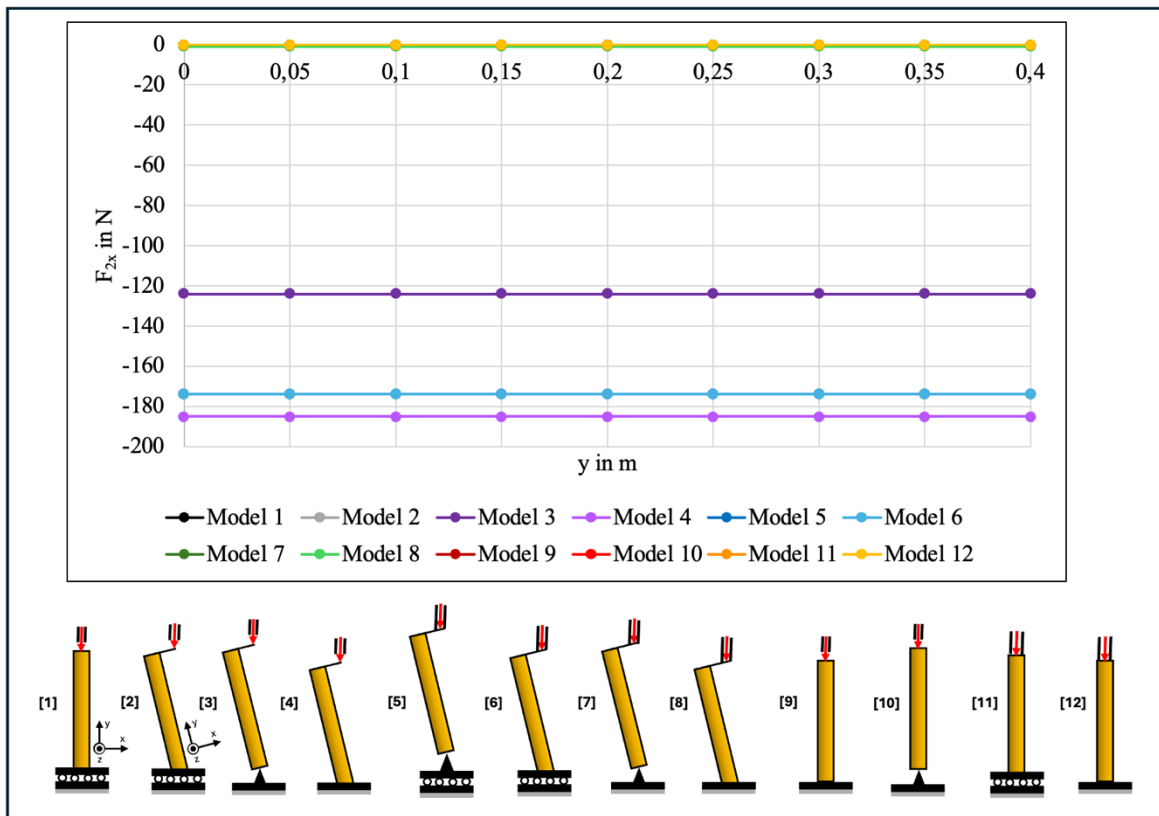
In an Excel spreadsheet,  $F_{2x}(y)$ ,  $F_{2y}(y)$ ,  $M_{2z}(y)$ , as well as the absolute maximum stress values in the bone, plate, and nail, were calculated and presented in graph form.

### **3.3 Results**

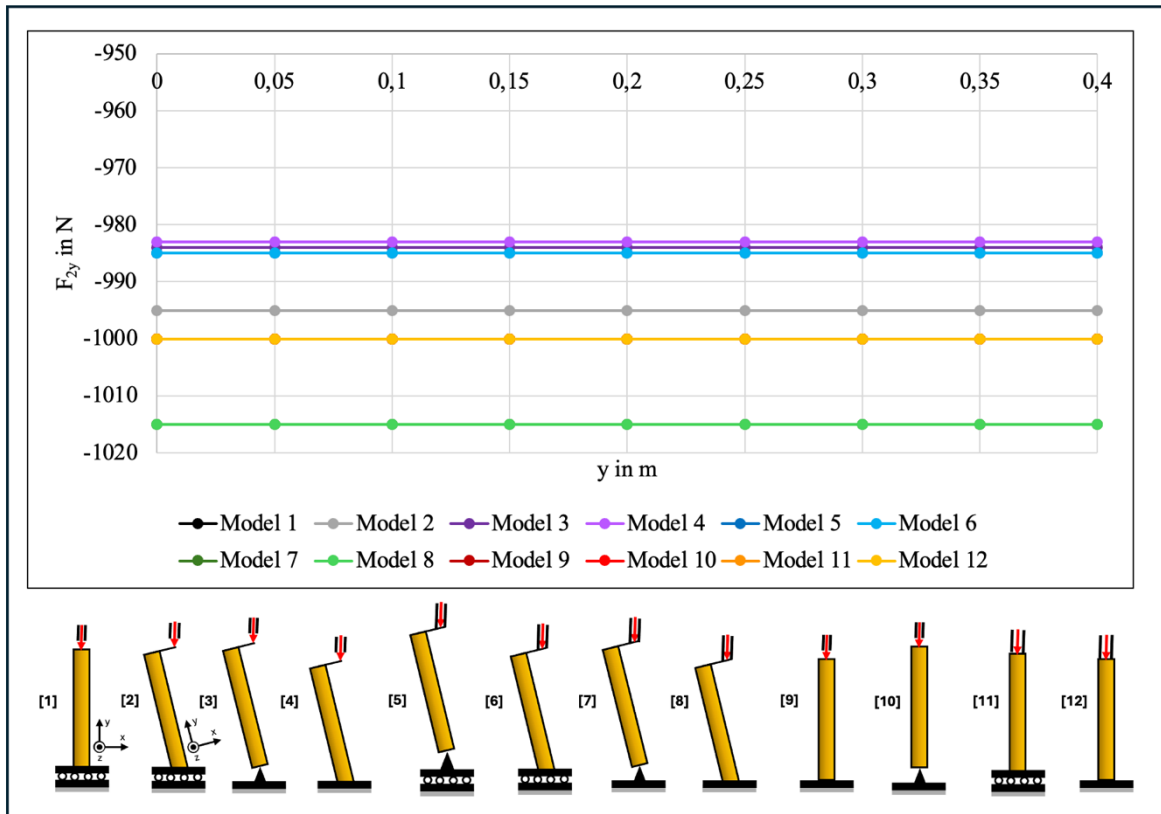
This section presents the graphs of the calculated internal forces, moments, and stress distribution. The analysis begins with the bone, followed by the lateral plate, and finally, the intramedullary nail. This approach allows for a detailed examination of how each component (bone, plate, and nail) responds to the applied compressive load in the different constraint sets.

### 3.3.1 Bone

The internal forces ( $F_{2x}$  and  $F_{2y}$ ) along the x- and y-axes for the bone in models 1 to 12 remained constant across the entire bone's length (Figure 25 and Figure 26). However, there were significant differences in the magnitude of shear forces ( $F_{2x}$ ) observed across some models. Models 2 to 6 exhibited moderate shear forces, with model 3 showing  $-124$  N, models 2, 5, and 6 showing  $-174$  N, and model 4 displaying the highest shear force at  $-185$  N. In contrast, model 8 also showed the presence of shear forces, but at a much smaller magnitude, around  $-1$  N, indicating that shear forces in this model were almost negligible. The remaining models (1, 7, 9, 10, 11, and 12) displayed no shear forces along the bone ( $F_{2x} = 0$  N), with their respective graphs overlapping in Figure 25.



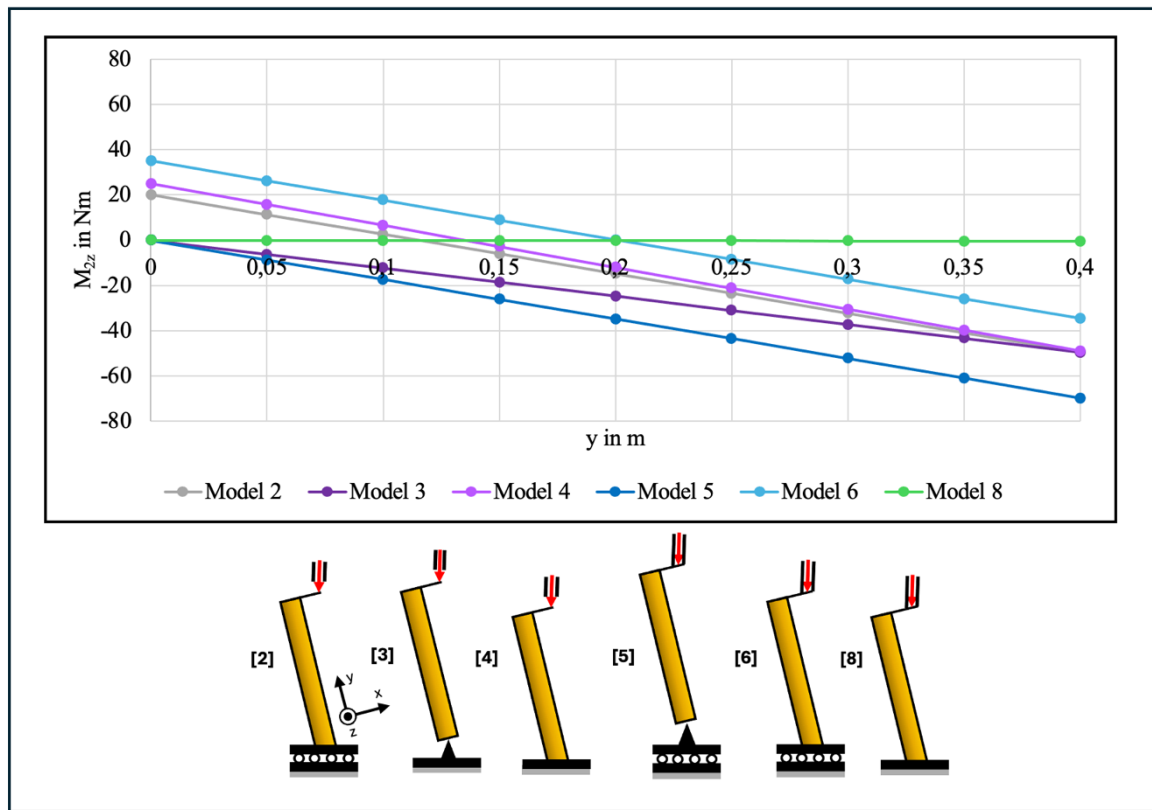
**Figure 25.** Results of the analytical modelling: Internal forces along the x-axis ( $F_{2x}$ ) in the bone for the models 1 to 12. The y-axis shows the internal forces along the x-axis ( $F_{2x}$ ) in newtons (N), while the x-axis represents the length along the bone ( $y$ ) in metres (m), with  $y = 0$  m at the distal end and  $y = 0,4$  m at the proximal end. Below the graph, the twelve models are displayed. The graphs for models 1, 7, 9, 10, 11, and 12 overlap due to their similar  $F_{2x}$  values and the graph for model 8 is obscured by these graphs. Similarly, the graphs for models 2, 5, and 6 overlap due to their similar  $F_{2x}$  values. The graphs for models 3 (dark purple) and 4 (light purple) are clearly visible in the combined graph.



**Figure 26.** Results of the analytical modelling: Internal forces along the y-axis ( $F_{2y}$ ) in the bone for models 1 to 12. The y-axis shows the internal forces along the y-axis ( $F_{2y}$ ) in newtons (N), while the x-axis represents the length along the bone (y) in metres (m), where  $y = 0$  m is the distal end and  $y = 0,4$  m is the proximal end. The twelve models are shown below the graph. The graphs of models 7 and 8 overlap due to their similar  $F_{2y}$  values. Models 1, 9, 10, 11, and 12 also show overlapping graphs. Similarly, the graphs of models 5 and 6 overlap. The graphs for model 2 (grey), 3 (dark purple), and 4 (light purple) are clearly visible in the merged graph.

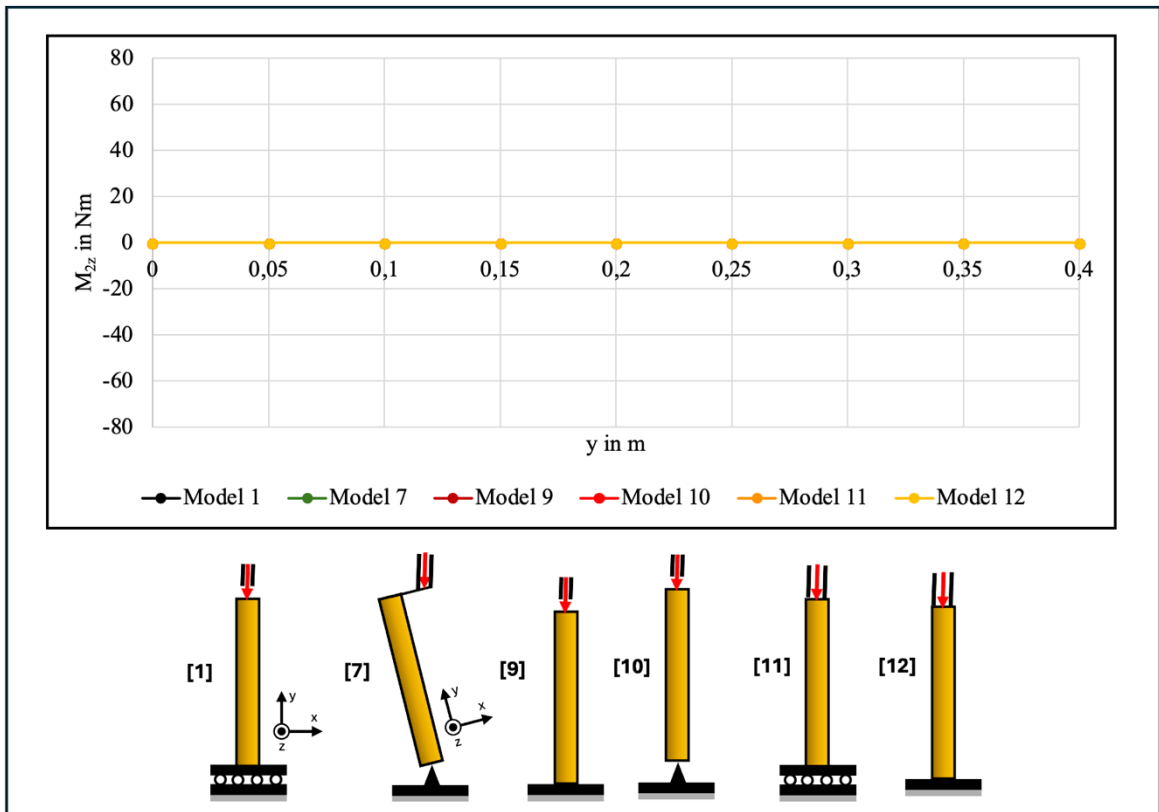
For the internal forces along the y-axis ( $F_{2y}$ ), all models also demonstrated constant magnitudes along the bone's length, which were considerably higher than the shear forces (Figure 26). Models 7 and 8 showed the highest internal forces along the y-axis ( $F_{2y} = -1015$  N), slightly exceeding the applied load of 1000 N. Followed by models 1, 9, 10, 11, and 12 with  $F_{2y} = -1000$  N, with their graphs overlapping in Figure 26. In contrast, the  $F_{2y}$  values of models 2, 3, 4, 5, and 6 were lower than the applied force of 1000 N (model 2 = -995 N, model 3 = -984 N, model 4 = -983 N, models 5, 6 = -985 N). The forces along the y-axis were dominated by compressive forces, as expected in a static single-legged stance scenario, which these models aimed to simulate.

The internal moments ( $M_{2z}$ ) along the bone in models 1 to 12 can be grouped into two categories: non-constant (Figure 27) and constant (Figure 28).



**Figure 27.** Results of the analytical modelling: Internal moments ( $M_{2z}$ ) along the bone for model 2, 3, 4, 5, 6, and 8 (non-constant group). The y-axis shows the internal moments ( $M_{2z}$ ) in newton-metres (Nm), while the x-axis represents the length along the bone (y) in metres (m), where  $y = 0$  m is the distal end and  $y = 0,4$  m is the proximal end. The models are shown below the graph. Model 8 (light green) shows minimum variation in  $M_{2z}$  along the bone, while the other models (2 (grey), 3 (dark purple), 4 (light purple), 5 (dark blue), and 6 (light blue)) exhibit significant variation in  $M_{2z}$  along the bone.

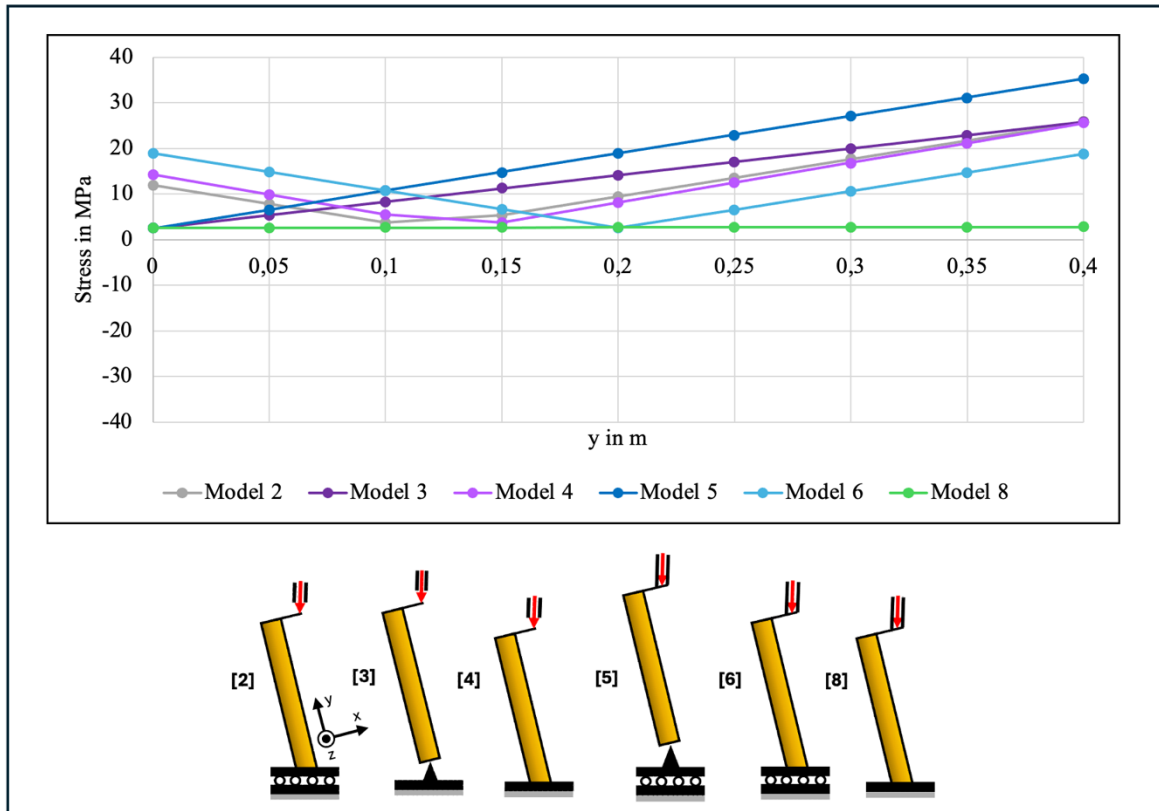
Models 2, 3, 4, 5, 6, and 8 fell under the non-constant group, where the internal moments varied along the bone's length. The  $M_{2z}$  values along the bone's length varied significantly for models 2, 3, 4, 5, and 6 (Figure 27). However, model 8 showed minimal variation in the internal moment, with very low magnitudes. For example, at  $y = 0,05$  m, the internal moment was approximately  $-0,05$  Nm, and at  $y = 0,15$  m, the internal moment increased only slightly to  $-0,15$  Nm.



**Figure 28.** Results of the analytical modelling: Internal moments ( $M_{2z}$ ) along the bone for models 1, 7, 9, 10, 11, and 12 (constant group). The y-axis shows the internal moments ( $M_{2z}$ ) in newton-metres (Nm), while the x-axis corresponds to the length along the bone ( $y$ ) in metres (m), where  $y = 0$  m is the distal end and  $y = 0,4$  m is the proximal end. The corresponding models are shown below the graph. The internal moments along the bone for these models are approximately 0 Nm. Due to the similarity in their internal moments, their graphs overlap.

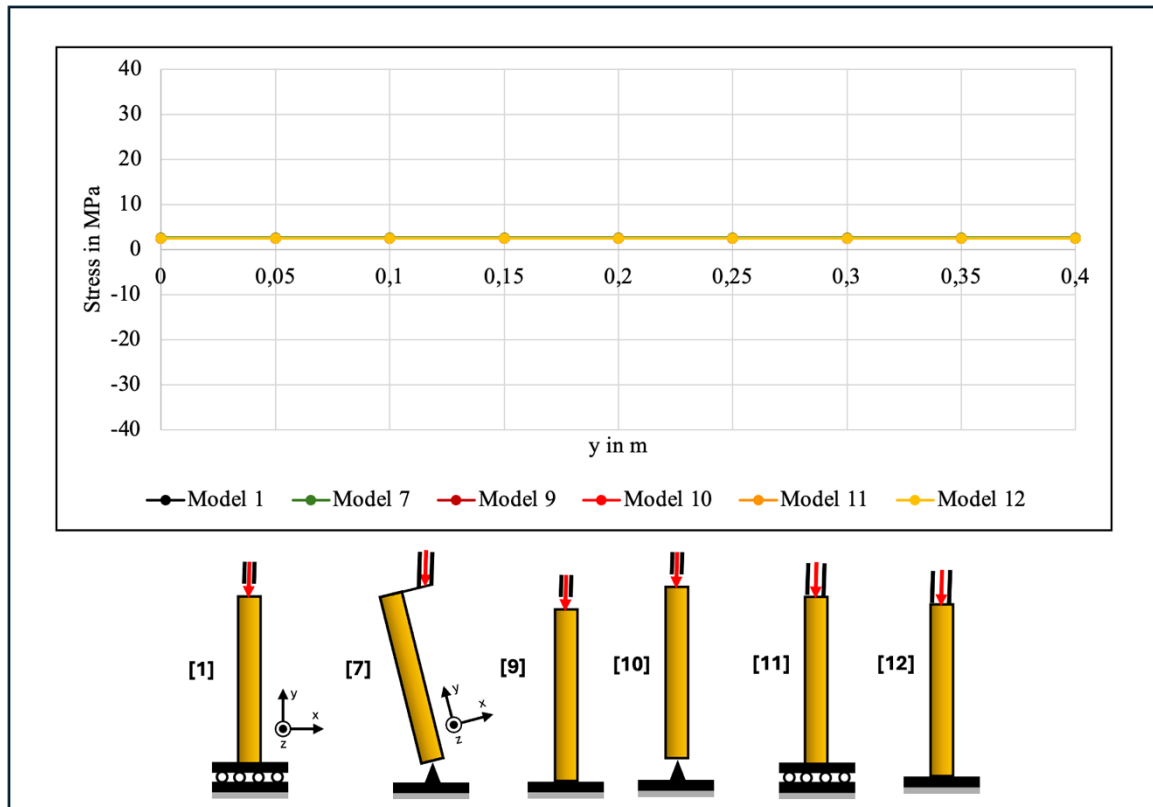
In contrast, models 1, 7, 9, 10, 11, and 12 exhibited constant internal moments along the bone, with low magnitudes. The graphs for these models were very similar and were plotted on top of each other in Figure 28. Due to this overlap, they appear as a single graph, which is why only one curve seems visible.

Figure 29 and Figure 30 illustrate the absolute maximum stress values along the bone.



**Figure 29.** Results of the analytical modelling: Absolute maximum stress values along the bone for models 2, 3, 4, 5, 6, and 8 (non-constant group). The y-axis represents the absolute maximum stress values in megapascals (MPa), while the x-axis corresponds to the length along the bone (y) in metres (m), with  $y = 0$  m as the distal end and  $y = 0,4$  m as the proximal end. The corresponding models are shown below the graph. Model 8 (light green) shows minimum variation in stress values along the bone's length, making the graph appears nearly constant. The other models (models 2 (grey), 3 (dark purple), 4 (light purple), 5 (dark blue), and 6 (light blue)) exhibit significant variation in stress values along the bone's length.

Models 2, 3, 4, 5, 6, and 8 exhibited non-constant stress distribution along the bone's length. This non-constant stress distribution aligned with the non-constant internal moments previously noted in these models. In models 3, 5, and 8, stress values increased from the distal ( $y = 0$  m) to the proximal ( $y = 0,4$  m) end. Model 8 exhibited minimal variation in stress distribution, making it appear nearly constant. Models 2, 4, and 6, on the other hand, showed a pattern where stress initially decreases before rising again toward the proximal end.



**Figure 30.** Results of the analytical modelling: Absolute maximum stress values along the bone for models 1, 7, 9, 10, 11, and 12 (constant group). The y-axis represents the absolute maximum stress values in megapascals (MPa), while the x-axis corresponds to the length along the bone (y) in metres (m), with y = 0 m as the distal end and y = 0,4 m as the proximal end. The corresponding models are shown below the graph. The graphs for these models overlap due to their similar stress distributions along the bone.

In contrast, Models 1, 7, 9, 10, 11, and 12 displayed a constant stress distribution along the bone, which aligns with the observation of constant internal moments in these models. In Figure 30, the graphs of these models overlap due to their similar behaviour. The stress values in these models remained low, around  $-2,5$  MPa.

**Table 4.** Results from the finite element analysis of the bone model: Minimum and maximum normal stress values in the bone.

Model	Max Stress in MPa	Min Stress in MPa
1	-2,5391	-2,5567
2	20,246	-26,078
3	20,502	-26,401
4	20,186	-26,003
5	29,697	-35,886
6	14,027	-19,04
7	-2,5359	-2,6389
8	-2,4831	-2,6851
9	-2,539	-2,5568
10	-2,5391	-2,5567
11	-2,5391	-2,5567
12	-2,5391	-2,5567

The minimum and maximum normal stress values in the bone, obtained from the finite element analysis, indicate that models 1, 7 to 12 exhibited lower stress levels, far below the cortical bone's yield strength (75,9–136,6 MPa; see 2.3 Femoral Shaft & Diaphyseal Fracture) (Table 4). This suggests that the femur could handle the applied load (1000 N), which resembles hip contact force during gait of a small person, without risk of failure or fracture. In contrast, Models 2 to 6 generated higher maximum stress values, ranging from 14,027 MPa to 29,697 MPa, and minimum stresses from -19,04 MPa to -35,886 MPa. Although these values did not exceed the yield strength of cortical bone (75,9–136,6 MPa), they were significantly higher than expected for a one-legged stance phase of gait, which should involve moderate physiological loading.

### 3.3.2 Plate

Similar to the internal forces ( $F_{2x}$  and  $F_{2y}$ ) observed in the bone, the internal forces along the plate remained constant along its entire length in all models (Figure 31 and Figure 32). Model 4 showed the highest shear force at  $F_{2x} = -251$  N, followed by models 2, 5, and 6 at  $-174$  N, model 3 at  $-124$  N, model 7 at  $69$  N, and model 9 at  $-67,377$  N. On the other hand, models 1, 8, 10, 11, and 12 displayed no shear forces along the plate ( $F_{2x} = 0$  N).

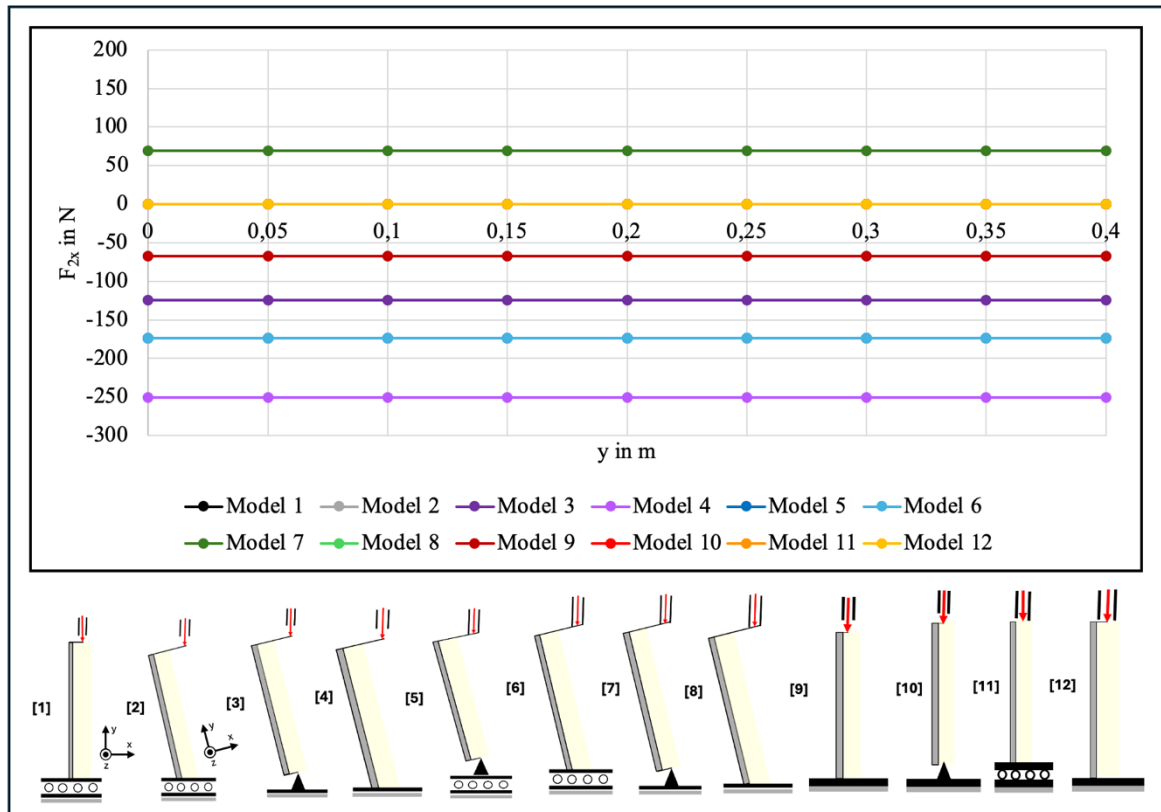


**Figure 31.** Results from the analytical modelling: Internal forces in the x-axis ( $F_{2x}$ ) along the lateral plate for models 1 to 12. The y-axis shows the internal forces in the x-axis ( $F_{2x}$ ) in newtons (N), and the x-axis represents the length along the plate ( $y$ ) in metres (m), where  $y = 0$  m is the distal end and  $y = 0,4$  m is the proximal end. The twelve models are shown below the graph. The graphs for models 2, 5, and 6 overlap due to their similar  $F_{2x}$  values. Similarly, the graphs for models 1, 8, 10, 11, and 12 overlap. The graphs for models 3 (dark purple), 4 (light purple), 7 (dark green), and 9 (dark red) are clearly visible in the combined graph.

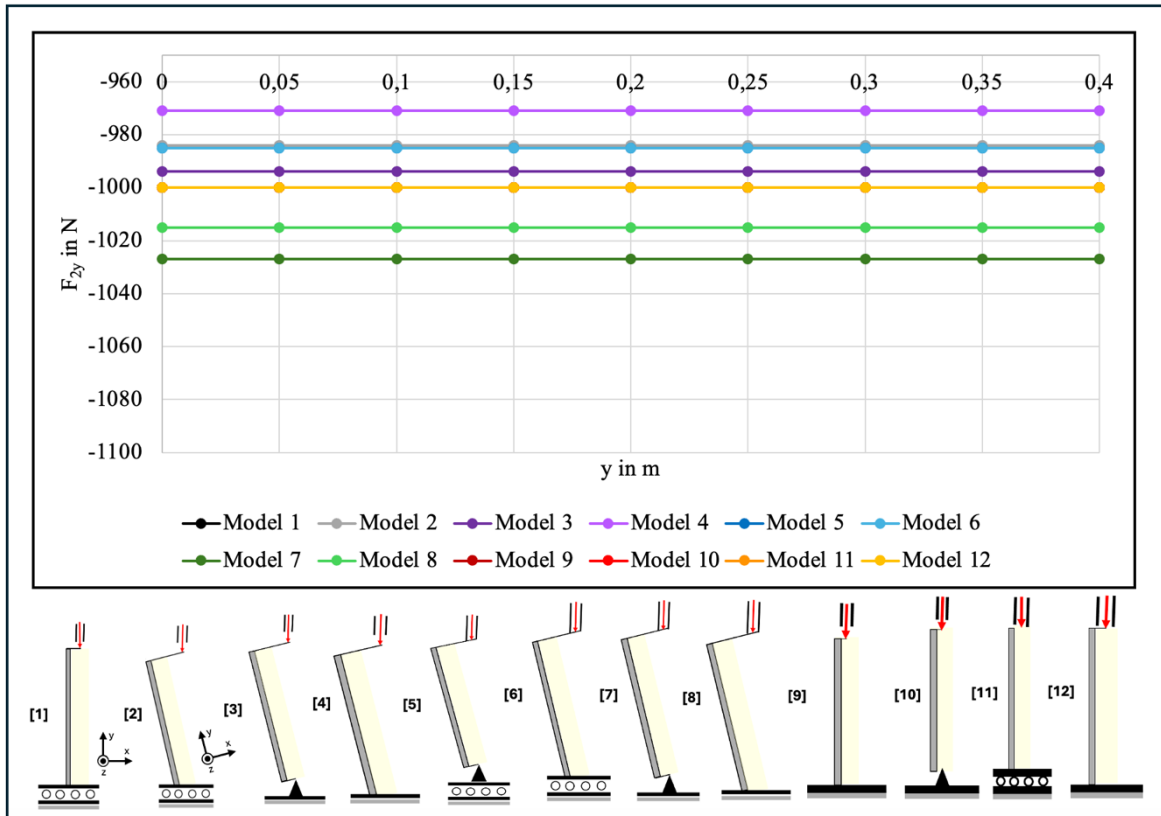


**Figure 32.** Results from the analytical modelling: Internal forces in the y-axis ( $F_{2y}$ ) along the lateral plate for models 1 to 12. The y-axis shows the internal forces in the y-axis ( $F_{2y}$ ) in newtons (N), while the x-axis corresponds to the length along the plate ( $y$ ) in metres (m), where  $y = 0$  m is the distal end and  $y = 0,4$  m is the proximal end. The twelve models are shown below the graph. The graphs for models 1, 9, 10, 11, and 12 overlap due to their similar  $F_{2y}$  values. Similarly, the graphs for models 5 and 6 overlap, partially obscuring the graph for model 2. The graphs for models 3 (dark purple), 4 (light purple), 7 (dark green), 8 (light green) are clearly visible in the combined graph.

For the forces along the y-axis ( $F_{2y}$ ), all models demonstrated constant magnitudes, which were considerably higher than the shear forces. Similar to the bone, the forces along the y-axis were compressive forces. Models 1, 9, 10, 11, and 12 exhibited the same  $F_{2y}$  values of  $-1000$  N, causing their graphs to overlap in Figure 32. Models 5 and 6 showed  $F_{2y}$  values of  $-985$  N, and their graphs also overlapped. Model 2 showed  $F_{2y} = -984$  N, causing its graph to be partially obscured by the graphs of models 5 and 6. The graphs for the remaining models (model 3 =  $-994$  N, model 4 =  $-971$  N, model 7 =  $-1027$  N, and model 8 =  $-1015$  N) are clearly visible in Figure 32.

When examining internal moments ( $M_{2z}$ ), the models can be grouped into those with non-constant (Figure 33) and constant (Figure 34) internal moments.

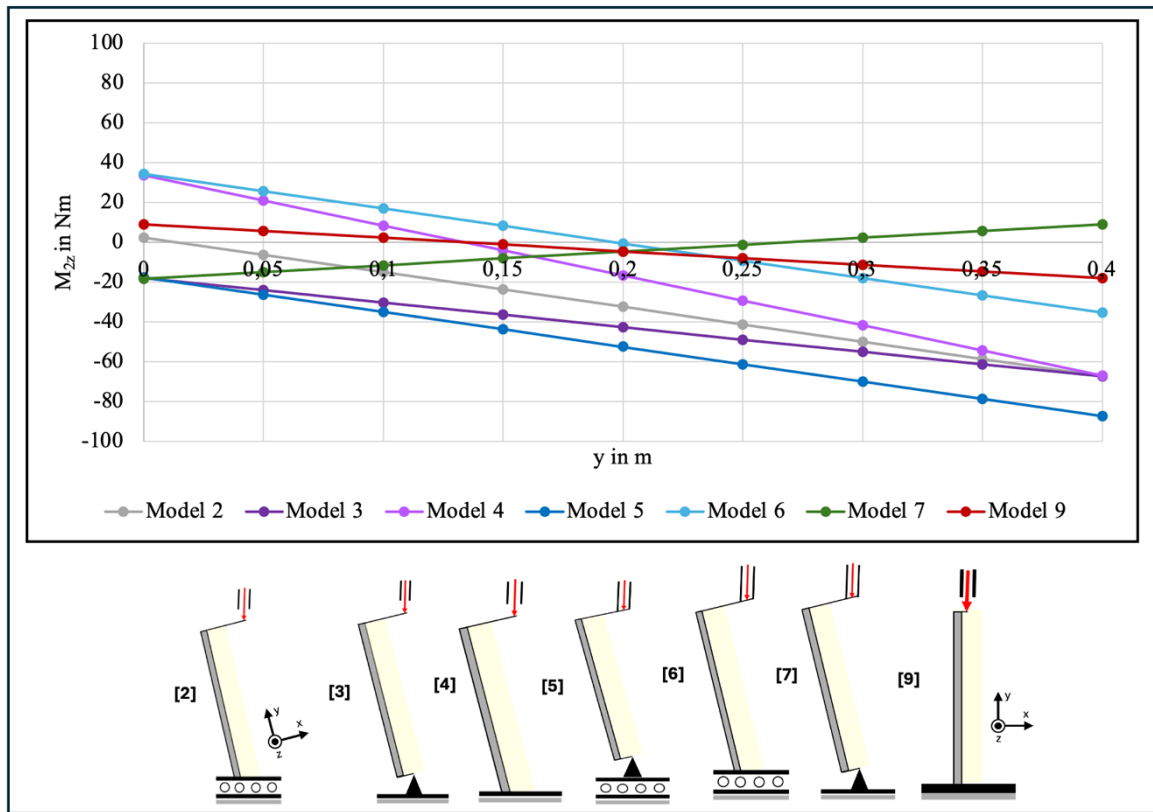


**Figure 33.** Results from the analytical modelling: Internal moments in the z-axis ( $M_{2z}$ ) along the lateral plate for models 2, 3, 4, 5, 6, 7, and 9 (non-constant group). The y-axis shows the internal moments in the z-axis ( $M_{2z}$ ) in newton-metres (Nm), while the x-axis corresponds to the length along the plate (y) in metres (m), where  $y = 0$  m is the distal end and  $y = 0,4$  m is the proximal end. The corresponding models are shown below the graph. Compared to models 2 (grey), 3 (dark purple), 4 (light purple), 5 (dark blue), and 6 (light blue), models 7 (dark green) and 9 (dark red) exhibit lower  $M_{2z}$  values along the lateral plate.

The internal moments in models 2, 3, 4, 5, 6, 7, and 9 varied along the plate, with models 2 to 6 experiencing significant variation of bending moments along the plate's length (Figure 33). Models 7 and 9 exhibited minimal variation of bending moments along the plate compared to models 2 to 6.

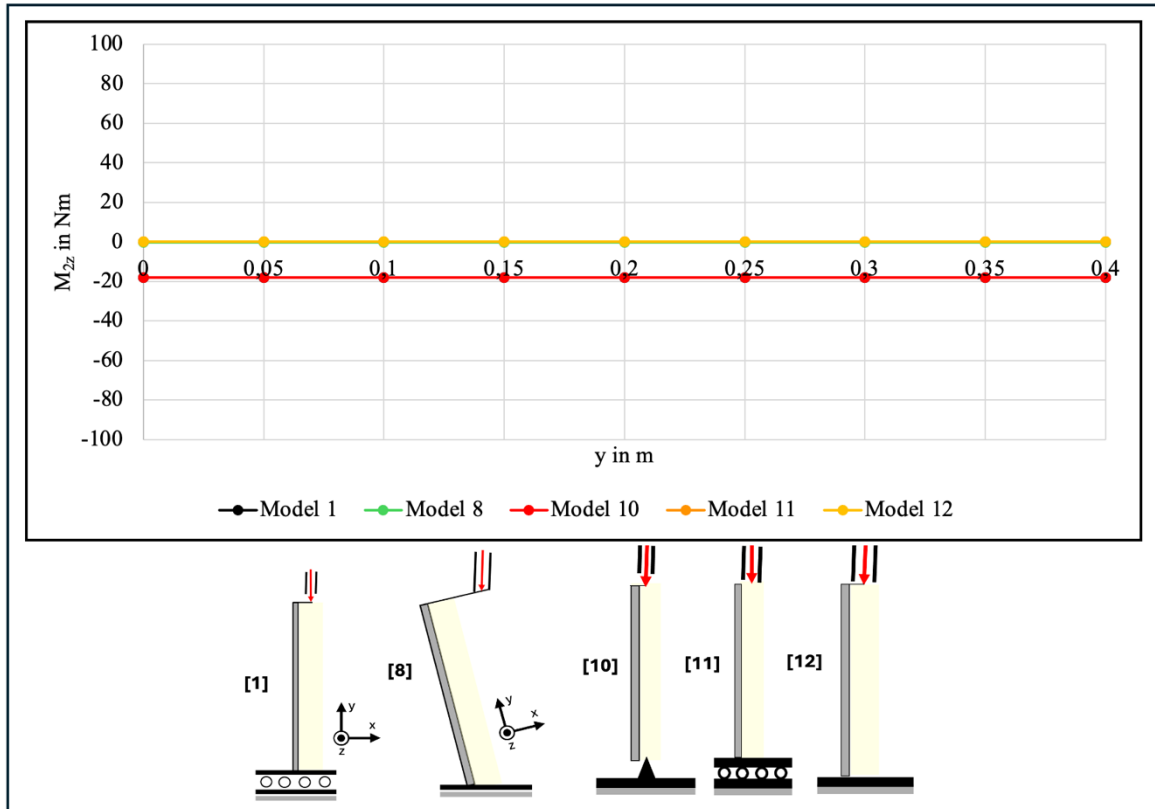


**Figure 34.** Results from the analytical modelling: Internal moments in the z-axis ( $M_{2z}$ ) along the lateral plate for models 1, 8, 10, 11, and 12 (constant group). The y-axis shows the internal moments in the z-axis ( $M_{2z}$ ) in newton-metres (Nm), while the x-axis represents the length along the plate (y) in metres (m), where  $y = 0$  m is the distal end and  $y = 0,4$  m is the proximal end. The corresponding models are shown below the graph. Due to their similar  $M_{2z}$  values along the plate, the graphs for models 1 and 10 overlap. Similarly, the graphs for models 11 and 12 overlap, partially obscuring the graph for model 8.

In contrast, models 1, 8, 10, 11, and 12 maintained constant internal moments along the plate with low magnitudes. Models 1 and 10 exhibited identical internal moments along the plate ( $M_{2z} = -18$  Nm), resulting in overlapping graphs in Figure 34. Model 8, with a much smaller internal moment of  $M_{2z} = -0,27$  Nm, is less visible in Figure 34 because it is partially obscured by the graphs of models 11 and 12, which exhibited no internal moments ( $M_{2z} = 0$  Nm). Additionally, the graphs for models 11 and 12 overlap one another.

The stress distribution along the plate mirrors the behaviour of the bending moments. Models 1, 8, 10, 11, and 12 showed constant stress distributions (Figure 36), while Models 2, 3, 4, 5, 6, 7, and 9 exhibited non-constant stress distributions (Figure 35).

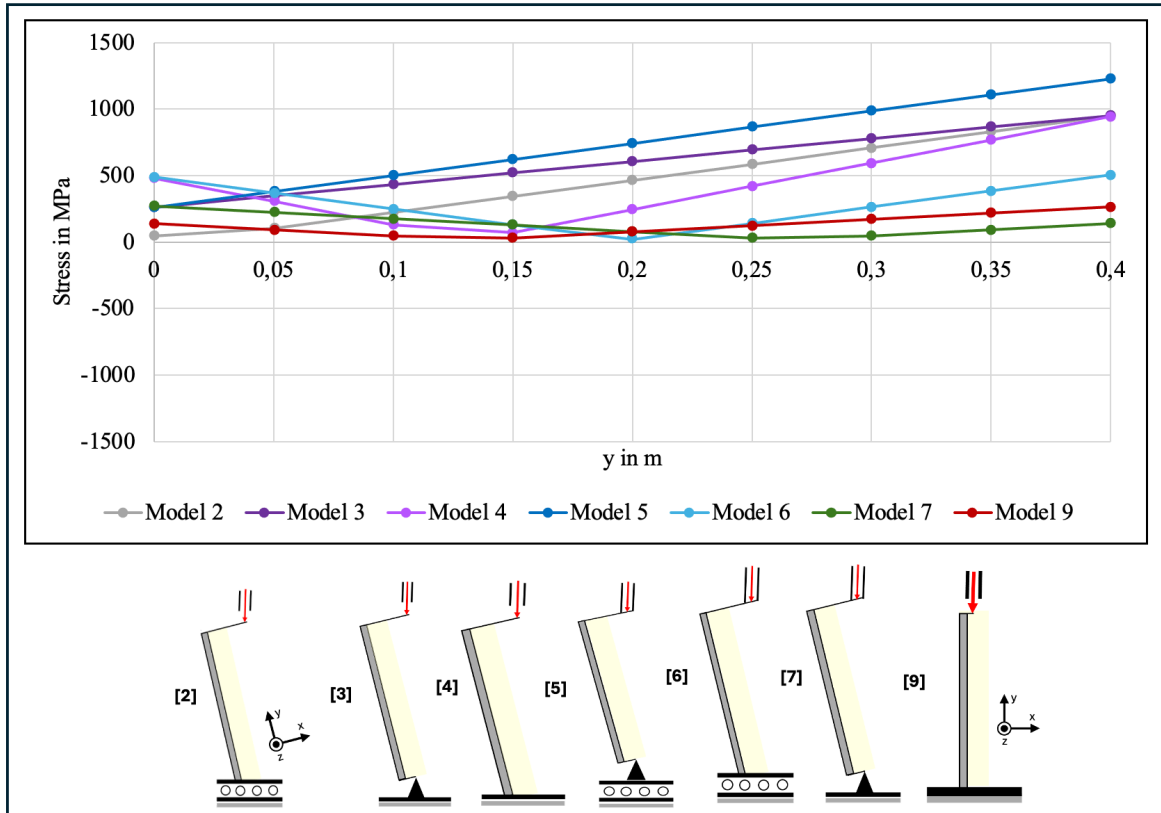


**Figure 35.** Results from the analytical modelling: Absolute maximum value of stress along the lateral plate for models 2, 3, 4, 5, 6, 7, and 9 (non-constant group). The y-axis shows the stress values in megapascals (MPa), while the x-axis corresponds to the length along the plate (y) in metres (m), where  $y = 0$  m is the distal end and  $y = 0,4$  m is the proximal end. The corresponding models are shown below the graph.

Models 2, 3, and 5 exhibited increasing stress from the distal to the proximal end, while models 4, 6, 7, and 9 showed stress patterns that decreased initially before rising again toward the proximal end. Models 7 and 9 showed minimal stress variation along the plate compared to models 2 to 6.

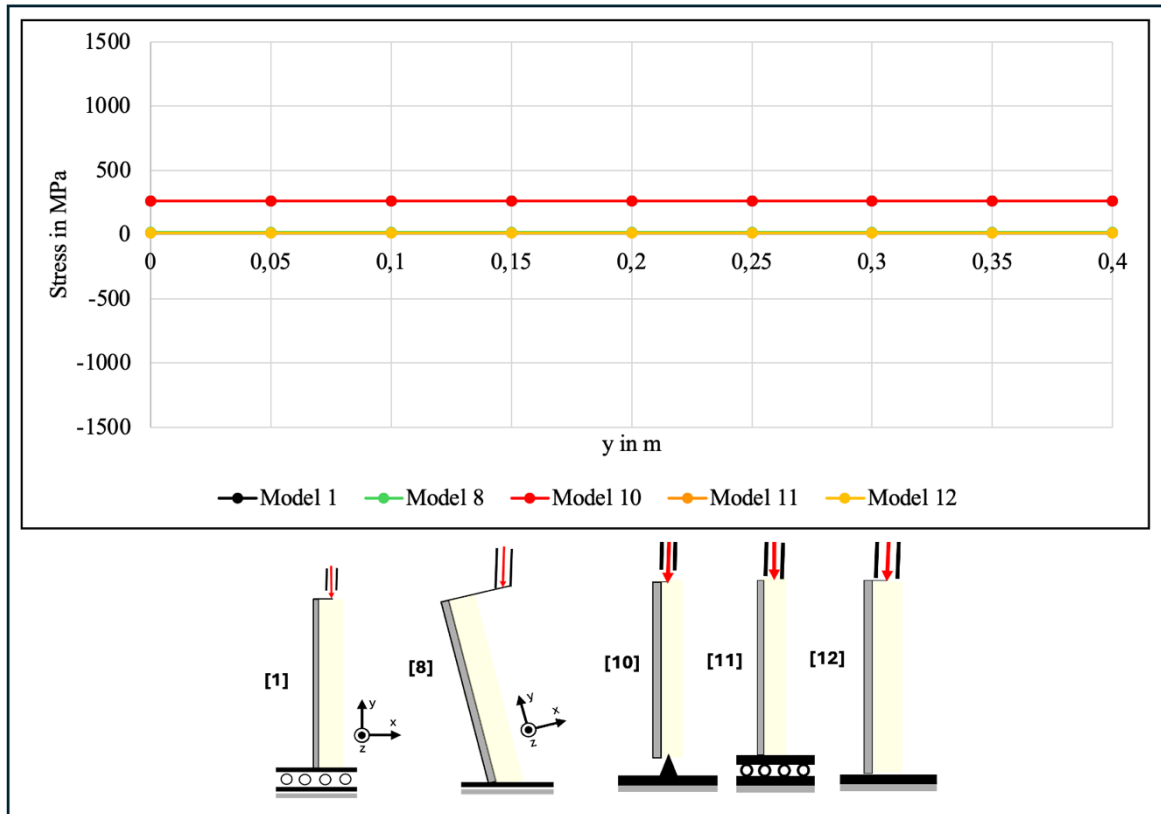


**Figure 36.** Results from the analytical modelling: Absolute maximum value of stress along the lateral plate for models 1, 8, 10, 11, and 12 (constant group). The y-axis shows the stress values in megapascals (MPa), while the x-axis corresponds to the length along the plate (y) in metres (m), where  $y = 0$  m is the distal end and  $y = 0,4$  m is the proximal end. The corresponding models are shown below the graph. Due to their similar stress values along the plate, the graphs for models 1 and 10 overlap. Similarly, the graphs for models 11 and 12 overlap, partially obscuring the graph for model 8.

Models 11 and 12 exhibited the same stress along the lateral plate (13,89 MPa), with their graphs overlapping in Figure 36. Similarly, models 1 and 10 shared an identical stress value of 263,89 MPa, and their graphs also overlap in Figure 36. Model 8, which had a stress value of 17,85 MPa, is partially obscured by the overlapping graphs of models 11 and 12, making it less visible in Figure 36.

The stress values in models 2, 3, 4, and 5 exceeded the typical strength limits for plate materials like stainless steel 316L (Yield strength: 1000 MPa), Ti-6Al-4V ELI (Yield strength: 795–875 MPa), and Ti-6Al-7Nb (Yield strength: 880–950 MPa) (Table 5), potentially leading to failure in osteosynthesis plates. Model 6 exhibited considerably high stress, almost half the yield strength of these implant materials. In contrast, models 1, 7, 8, 9, 10, 11, and 12 maintained lower stress levels (Table 5), remaining within the material's strength limits.

**Table 5.** Results from the finite element analysis of the plate model: Minimum and maximum normal stress values in the plate.

Model	Max Stress in MPa	Min Stress in MPa
1	256,54	-284,31
2	991,81	-1019,2
3	1000,8	-1028,4
4	977,84	-1004,8
5	1295,6	-1322,9
6	507,49	-534,84
7	263,37	-291,92
8	-13,983	-14,223
9	256,3	-284,08
10	256,54	-284,31
11	-13,889	-13,889
12	-13,889	-13,889

### 3.3.3 Nail

The internal forces ( $F_{2x}$  and  $F_{2y}$ ) along the nail were constant throughout its length. Since the nail is implanted in the bone axis, the  $F_{2x}$  and  $F_{2y}$  showed similar values to those in the bone (Figure 25 and Figure 26). Models 2, 5, and 6 displayed shear forces of  $-174$  N, while model 4 exhibited the highest shear force of  $-185$  N. Model 3 showed  $F_{2x}$  of  $-124$  N. In contrast, models 1, 7, 9, 10, 11, and 12 showed no shear forces along the nail ( $F_{2x} = 0$  N). Model 8 also showed the presence of shear force, but at a much smaller magnitude, around  $-1$  N.

Models 7 and 8 exhibited the highest internal forces along the y-axis ( $F_{2y} = -1015$  N), followed by models 1, 9, 10, 11, and 12 with  $F_{2y} = -1000$  N. Model 2 showed  $F_{2y} = -995$  N. Models 3 and 4 showed  $F_{2y}$  values of  $-984$  N and  $-983$  N, respectively, while models 5 and 6 both exhibited  $F_{2y} = -985$  N.

The internal moments ( $M_{2z}$ ) along the nail also had the same values as the internal moments along the bone (Figure 27 and Figure 28), categorized into two groups: constant and non-constant. Models 2, 3, 4, 5, 6, and 8 exhibited non-constant internal moments, with models 2 to 6 showing significant variation of internal moments along the nail, while model 8 displayed only slight variations, almost appearing constant. The remaining models (1, 7, 9, 10, 11, and 12) demonstrated constant and low internal moments along the nail.

The stress values along the nail differed from those in the bone, primarily due to differences in cross-sectional geometry. Stress levels in the nail were higher than in the bone but remained lower than the stress observed along the plate. The stress distribution along the nail could be divided into two groups: non-constant (Figure 37) and constant (Figure 38).

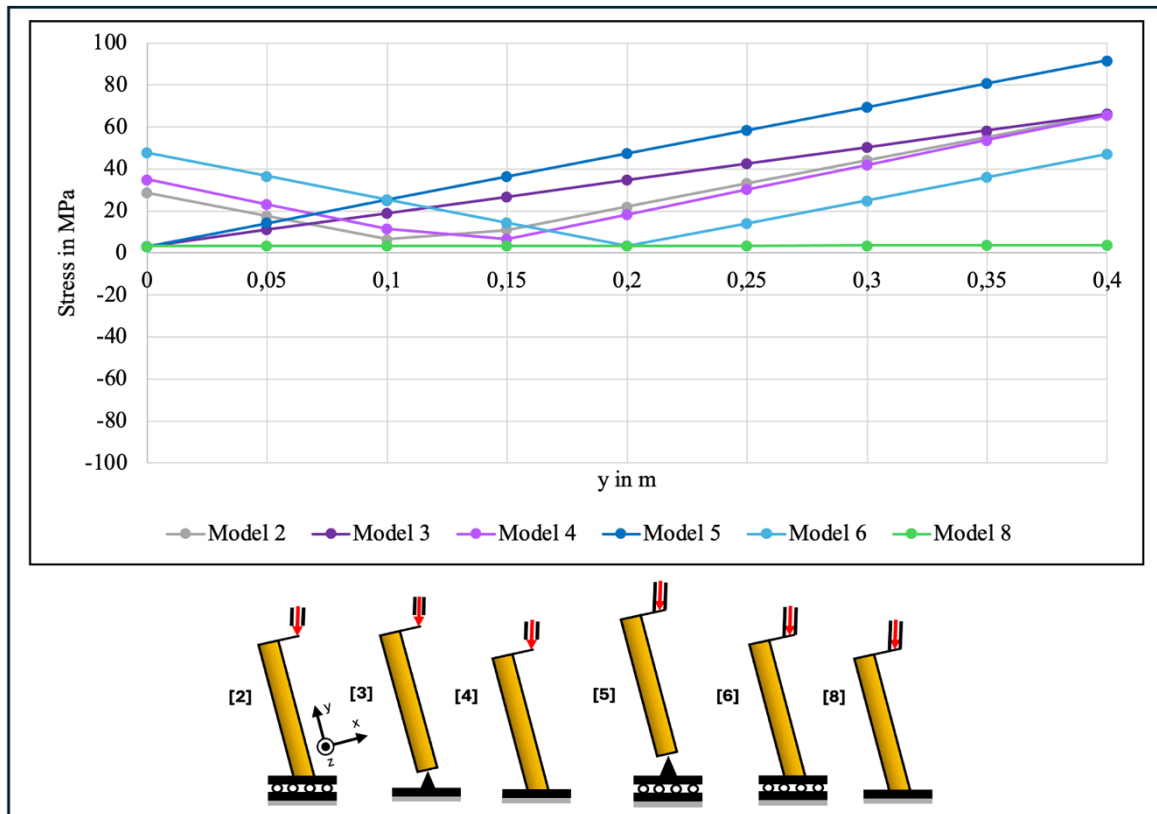


**Figure 37.** Results from the analytical modelling: Absolute maximum value of stress along the nail for models 2, 3, 4, 5, 6, and 8 (non-constant group). The y-axis shows the stress in megapascals (MPa), while the x-axis corresponds to the length along the nail ( $y$ ) in metres (m), with  $y = 0$  m as the distal end and  $y = 0,4$  m as the proximal end. The corresponding models are shown below the graphs. The stress values in model 8 (light green) vary only slightly along the nail's length, which is why the graph seems constant. In contrast, the stress values in models 2 (grey), 3 (dark purple), 4 (light purple), 5 (dark blue), and 6 (light blue) vary significantly along the nail's length.

Models 2, 3, 4, 5, 6, and 8 exhibited non-constant stress distribution along the nail's length. In models 3, 5, and 8, stress increased from the distal end to the proximal end. However, model 8 displayed minimal variation in stress along the nail compared to the others (models 2, 3, 4, 5, and 6), making it appear almost constant in Figure 37. Models 2, 4, and 6 showed a pattern where stress initially decreases before increasing toward the proximal end.

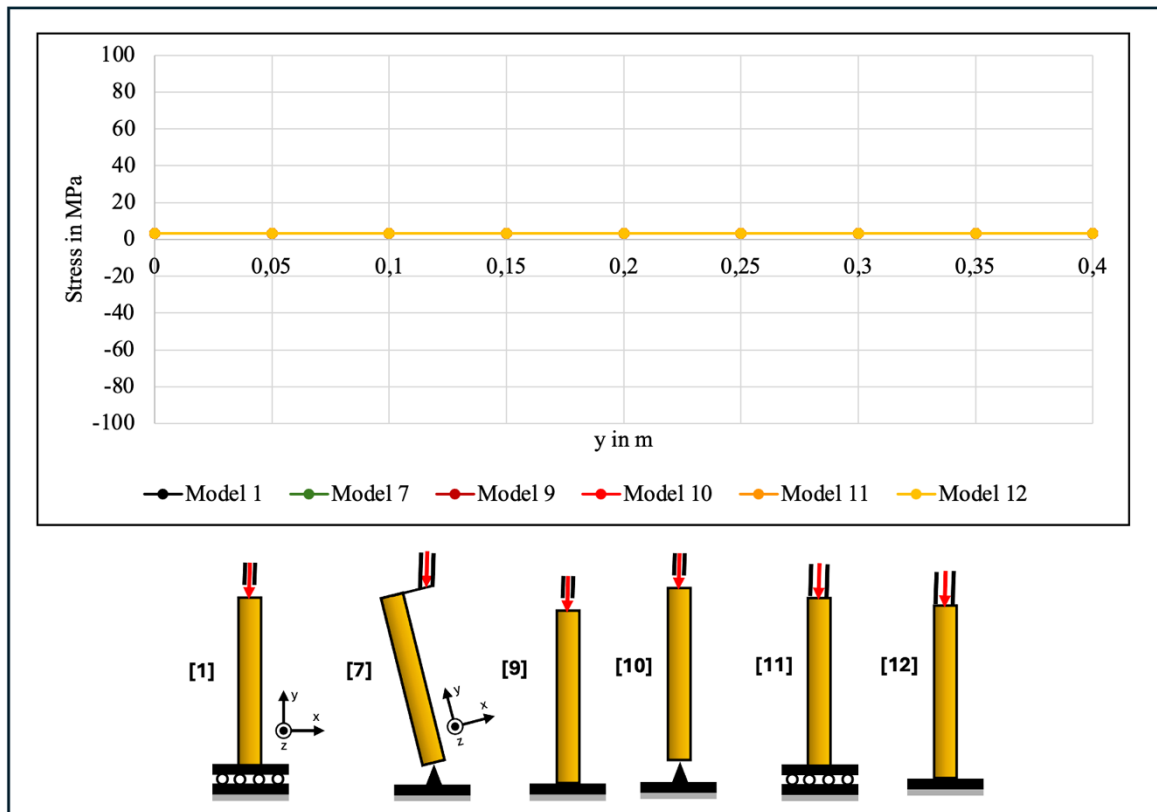


**Figure 38.** Results from the analytical modelling: Absolute maximum value of stress along the nail for models 1, 7, 9, 10, 11, and 12 (constant group). The y-axis shows the stress in megapascals (MPa), while the x-axis represents the length along the nail ( $y$ ) in metres (m), with  $y = 0$  m as the distal end and  $y = 0,4$  m as the proximal end. The corresponding models are displayed below the graphs. The graphs for models 1, 9, 10, 11, and 12 overlap due to similar stress values along the nail's length, obscuring the graph for model 7.

The remaining models (1, 7, 9, 10, 11, and 12) fell into the constant stress distribution group, with a low stress magnitude of approximately 3,183 MPa for models 1, 9, 10, 11, and 12, and slightly higher, at 3,23 MPa, for model 7. In Figure 38, the graphs for models 1, 9, 10, 11, and 12 overlap with one another, and the graph for model 7 is obstructed by these models. It is important to note that no minimum or maximum normal stress values were obtained from the finite element analysis for the nails.

### 3.4 Discussion

The results indicate that the internal forces, moments, and stress distribution along the bone, plate, and nail are influenced by the proximal and distal displacement constraints during biomechanical testing. The internal forces along the x- and y-axes ( $F_{2x}$  and  $F_{2y}$ ) remained

constant across all models for the bone, plate, and nail, suggesting that variations in stress distribution are primarily driven by differences in bending moments.

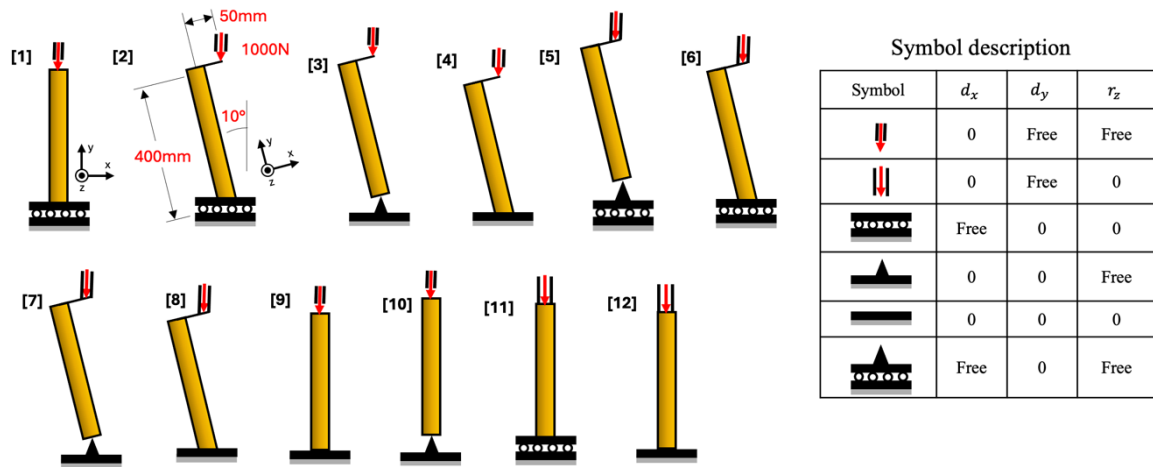


**Figure 39.** The twelve models developed for the study. Reproduced from Section 3.2 Methodology-Finite Element Analysis and Analytical Modelling, Figure 20.

Models 2 to 6 (Figure 39) exhibited high and non-constant bending moments and stress in the bone. Although these stress values did not exceed the yield strength of cortical bone (75,9–136,6 MPa), they are considerably higher than what is expected during moderate physiological loading, such as one-legged stance during gait. In contrast, models 1 and 7 to 12 (Figure 39) demonstrated lower stress values, ranging between  $-2,5$  MPa to  $-2,6$  MPa, aligning with Pauwels' (1980) theory that nature incorporates a safety factor to reduce stress.

The yield strength represents the point at which the bone begins to undergo plastic deformation, meaning that any changes to its shape become permanent. Avoiding this threshold is crucial, as it represents the bone's limit under load before irreversible damage occurs. In this study, an applied force of 1000 N was used, and for this load, the stresses in all models remained below the cortical bone's yield strength. This load was chosen to replicate the force exerted on the femur during gait of a small individual weighing around 30-40 kg. However, in reality, people vary widely in weight, bone geometry, and activity levels; some activities, like jumping, exert significantly higher loads on the femur. Thus, the 1000 N load serves as a simplified representation, allowing the study to estimate the loading and stress distribution along the bone.

Additionally, stress increases linearly with applied load, which means as the force acting on the femur increases, so does the stress. The force exerted on the femur during walking ranges from approximately 2,4 to 3 times an individual's body weight (Bergmann, Graichen and Rohlmann, 1993; Bergmann *et al.*, 2001). This implies that individuals with higher body weights would experience higher stress in their femurs while walking, potentially leading to fractures if the stress exceeds the cortical bone's yield strength. However, in reality, people with higher body weights do not typically fracture their femurs from walking alone. This observation implies that the stress on the bone during walking is lower than initially expected, which aligns with findings from Pauwels (1980), who proposed that the muscle activity helps limit stress in the femur.

For the plate, models 2 to 6 showed high stress values with non-constant stress distribution along the plate, especially in models 2, 3, 4, and 5, where the stress exceeded the typical strength limit for plate materials (under 1000 MPa). The maximum stress for model 6 obtained from the finite element analysis was  $-534,84$  MPa. While this did not exceed the typical strength limit for plate material, it was considerably high. Models 7 and 9 also exhibited non-constant stress and internal moment, though their values were significantly lower than those in models 2 to 6. In contrast, models 1, 8, 10, 11, and 12 demonstrated constant and low internal moment and stress along the plate.

Similarly, the nail follows the same pattern as the bone, where models 2 to 6 exhibited high and non-constant internal moment and stress, whereas the internal moment and stress for models 1, 7, 9, 10, 11, and 12 remained low and constant. Model 8 exhibited non-constant internal moment and stress, but the variations in these values along the nail's length were minimal. For example, at  $y = 0,1$  m, the stress was approximately 3,36 MPa, and at  $y = 0,2$  m, the stress increased only slightly to 3,49 MPa. This indicates that while the internal moment and stress did fluctuate, the magnitude of change was relatively low, suggesting a more stable and predictable loading condition compared to models 2 to 6.

The internal moments along the bone for models 1, 7, 9, 10, 11, and 12 were 0 Nm. Model 8 exhibited non-constant internal moments. However, it showed minimal variation in internal moments, and the values remained very low along the bone's length, allowing it to be considered as constant. Due to the constant loading along the bone, these models (1, 7, 8,

9, 10, 11, and 12) produce predictable loading along the bone's length. Although these models do not fully align with the findings from Taylor *et al.* (1996) and Duda, Schneider and Chao (1997)—which suggest that bending moment in the femur are minimized (not entirely eliminated) due to muscle activity—these models may be more suitable for plate testing. This is because they offer predictable loading along the bone's length compared to models 2 to 6, which exhibited non-constant internal moments along the bone's length.

However, only in models 1, 8, 10, 11, and 12 were the internal moments along the plate constant. With these characteristics (constant and predictable loading along the bone and plate), models 1, 8, 10, 11, and 12 eliminate the sensitivity of the outcomes to the plate positioning. The predictable and quantified loading in these models enables more reliable assessments of the plate strength, especially in models 1, 10, 11, and 12, which offer simpler configurations. In models 2 to 6, the load on the plate varies significantly along its length. Due to this variation, it needs to be considered that not the mechanically weakest part of the plate experiences the highest burden – and by that an analysis of the mechanical stability might be misleading if the plate is positioned slightly different. By maintaining constant and measurable loads, it becomes easier to evaluate whether the plate will perform adequately or fail under physiological conditions. However, models 11 and 12 exhibited zero bending in the plate, making them unsuitable for testing, as plates need to undergo bending to assess their structural integrity and failure risk.

On the assumption that Taylor *et al.* (1996) and Duda, Schneider and Chao (1997) are correct that the femur is primarily subjected to axial loading with limited bending moments due to muscles, models 1 and 10 are suggested to be the most appropriate for testing osteosynthesis plates under gait conditions compared to the other models developed in this study (Figure 39).

The following discusses which models may be suitable for testing intramedullary nails under gait conditions. Since the intramedullary nail is implanted in the femur's axis, the bending moment experienced by the nail should closely match the bending moment experienced by the bone. According to Pauwels (1980), Munih, Kralj and Bajd (1992), Taylor *et al.* (1996), and Duda, Schneider and Chao (1997), the bending moments experienced by the femur are minimized by muscle activity, suggesting that realistic testing scenarios should involve low

bending moments in the bone. Models 1, 7, 8, 9, 10, 11, and 12 showed low and constant internal moments along the bone compared to models 2 to 6. As mentioned earlier, models 1, 7, 9, 10, 11, and 12 do not fully align with the theories of Pauwels (1980), Munih, Kralj and Bajd (1992), Taylor *et al.* (1996), and Duda, Schneider and Chao (1997), but these models produced constant and predictable loading along the bone and nail, which can be beneficial for implant testing. In models 2 to 6, the bending moment along the intramedullary nail varies significantly. Due to this variation, stress concentrations may occur in different regions along the nail's length. As a result, an analysis of the nail's mechanical stability might produce inconsistent and potentially misleading outcomes.

Additionally, screws—the most common failure points in nail constructs—are generally tested under axial loading, as in models 1, 7, 8, 9, 10, 11, and 12, which experience axial compression along the nail's length. Plates are subjected to greater bending moment than nails due to their position, which introduces greater moment arm for the axial load (Nwagbara, 2019). The analytical modelling results for models 1, 7, 8, 9, 10, 11, and 12 align with this theory, further supporting that these models may represent realistic scenarios for nail testing. However, models 7 and 8, where the femur is oriented at an angle, might be more challenging to set up, whereas models 1, 9, 10, 11, and 12, with the femur positioned vertically, may allow for easier setup (Figure 39).

## **4 Chapter II: Literature Review**

This section focuses on a comprehensive literature review to determine which biomechanical test setups were employed in studies related to femoral diaphyseal implants. Similar to the structure of Chapter I: Finite Element Analysis, this chapter is divided into methodology, results, and discussion. In this chapter, the test setup from each paper focusing on human mid-shaft femur fractures was matched with the twelve models/constraint sets developed in Chapter I, and its suitability and effectiveness for addressing the study's objectives were also reviewed.

### **4.1 Methodology**

The PRISMA-P guidelines were introduced in 2015 to standardize and improve the quality of systematic review protocols. PRISMA-P stands for “Preferred Reporting Items for

Systematic Reviews and Meta-Analyses Protocols”. These guidelines are designed to ensure systematic review protocols are thoroughly documented and transparent (Moher *et al.*, 2015). The PRISMA-P checklist comprises 17 items (26 including sub-items) that outline the essential components of a systematic review or meta-analysis protocol (*PRISMA for systematic review protocols (PRISMA-P)*, no date).

Following the PRISMA-P guidelines, a systematic search was performed on PubMed and Scopus on April 23, 2024, using the keywords “(biomechanical testing) AND ((femur) OR (femoral)) AND (fixation) AND (human) AND (implant)”. For the review, studies were included based on the following criteria:

- The study includes biomechanical testing using either cadaveric human femurs or synthetic human femurs,
- The study involves implants for human femur,
- The publication is available in English or German,
- The study was published between January 1, 2004, and April 23, 2024,
- Studies that only use finite element analysis for virtual fracture recreation and biomechanical analysis were excluded,
- Studies categorized as reviews, conference abstracts, case reports, letters, or author comments were excluded.

At first, studies in German or English retrieved from PubMed and Scopus using the mentioned keywords were first screened for duplicates. After removing duplicates, the titles and abstracts of the remaining studies were imported into Excel, where they were further screened by both the author and a second supervisor to ensure they met the defined criteria. Any disagreements between reviewers were resolved through discussion. The studies were then categorized into six groups: hip endoprosthesis, knee endoprosthesis, femoral distal fractures, femoral proximal fractures, femoral mid-shaft fractures, and special cases.

Papers within the mid-shaft fractures group underwent further detailed analysis. The following details were extracted from the paper: aim of the study, AO fracture type, fracture

description, picture of the fracture, implant description, picture of the implant, number of specimen used, specimen type, outcome parameter, stop criteria, measuring instrument, load type, applied load (force and moment in x, y and z directions), static or dynamic load, load cycle for dynamic test, angle of the femur (frontal plane and sagittal plane), picture of the setup, degrees of freedom of distal and proximal ends, findings, and limitations. This information was organized and saved in an Excel spreadsheet.

As the focus of this work lies on gait and is based on results of Taylor *et al.* (1996) and Duda, Schneider and Chao (1997), axial compression test setup from each paper was then compared and categorized based on its similarity to the twelve models/constraint sets. Each of the 19 papers (see 4.2 Result) in the mid-shaft fractures group conducted at least one axial compression test. The suitability and effectiveness of these axial compression test setups for addressing the study's objectives were reviewed and discussed.

## **4.2 Result**

Figure 40 presents a visual overview of the article selection process, highlighting each stage of the screening process and the number of papers included at each step. The results are presented in two tables: Table 6 provides information regarding the test setups extracted from studies investigating femoral mid-shaft plate osteosynthesis, while Table 7 summarizes the test setups from studies focusing on intramedullary nails for mid-shaft fracture fixation.

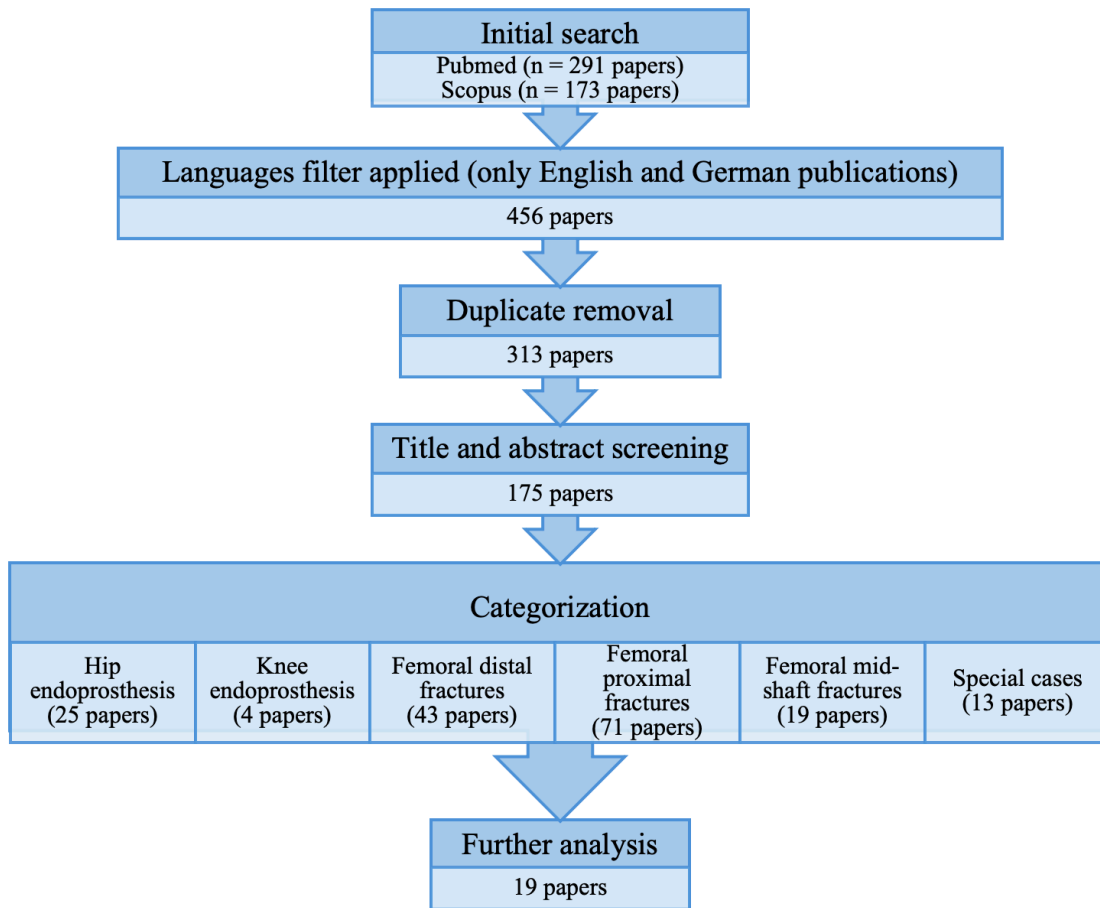


**Figure 40.** The process of article selection and the number of papers included at each stage.

Out of the 15 papers focusing on osteosynthesis plates, one paper used a setup similar to model 8, which showed constant and low bending moments and stress in the plate. The bending moments and stress distribution along the bone in this model are not constant; however, the magnitude and variation in both are minimal. As result, the bending moment and stress appear nearly constant along the bone.

Two papers used a setup similar to model 9, where the axial forces were applied to the bone axis. This model resulted in low and constant bending moments and stress in the bone, but low and non-constant bending moments and stress in the plate.

Five papers employed a setup like model 4, which generated high and non-constant bending moments and stress in both the plate and bone. Among these, papers 10 and 11 (see Table 6) also tested the femurs in a forward flexion orientation. This specific setup does not correspond to any of the twelve models analysed in Chapter I. Consequently, these setups

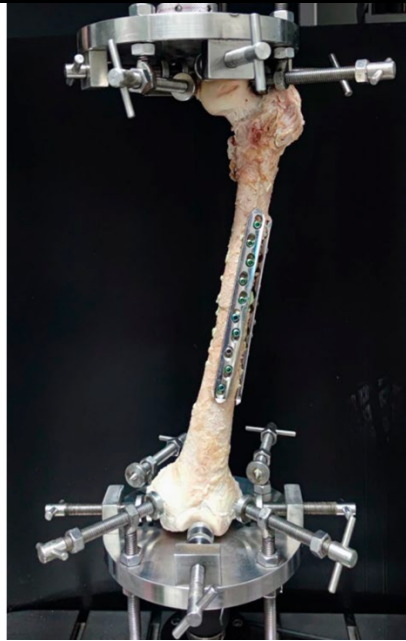
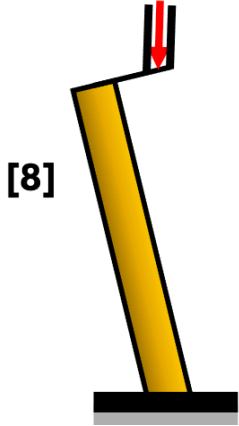
could not be categorized into the twelve models/constraint sets. One paper used a setup similar to model 3, which behaved similarly to model 4, and one paper's setup was unknown.

In three of the reviewed papers (papers 2, 3, and 4, see Table 6) axial force was applied to the proximal end of the femur using a flat plate. However, the studies did not specify the exact movements allowed at the proximal end, leading to two possible interpretations based on the friction between the flat plate and the femur. If the friction was large enough to prevent movement along the x-axis ( $d_x$ ) and rotation in the z-axis ( $r_z$ ), the setup would be comparable to model 8. If the friction was insufficient to stop movement in the x-axis ( $d_x$ ) and rotation in the z-axis ( $r_z$ ), the setup would align with model 2, which resulted in higher and non-constant bending moments and stress along the plate and bone.

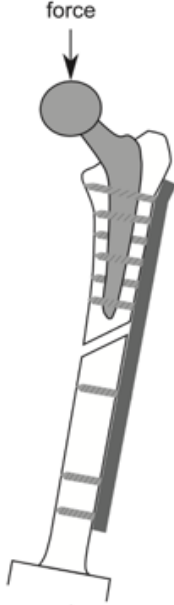
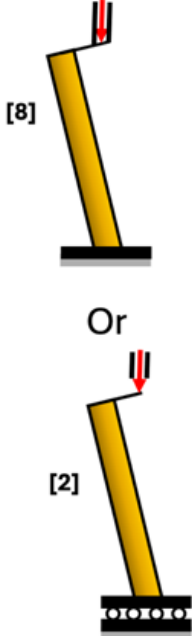
Two papers (papers 5 and 7, see Table 6) placed the femoral head under a pre-shaped mould attached to the machine actuator. If the friction between the mould and the femoral head prevents rotation in the z-axis ( $r_z$ ), the setup resembled model 7, which exhibited low and constant bending moments and stress along the bone, but non-constant and low stress and bending moments along the plate, similar to model 9. On the other hand, if the femoral head was able to rotate in the z-axis ( $r_z$ ), the setup would resemble model 3. Model 3 demonstrated high and non-constant bending moments and stress distribution in both the plate and the bone.

Among the four papers focused on intramedullary nails, one paper (paper 2, see Table 7) conducted two axial compression tests: the first test employed a setup similar to model 12, while the second test used a setup comparable to model 8. Both setups generated low bending moments and stress in the bone and nail. Model 8 exhibited non-constant but minimal variation in internal moment and stress along the bone and nail, resulting in a nearly constant distribution. One paper used a setup similar to model 4, resulting in high and non-constant bending moments and stress along both the bone and the nail. The setups in the remaining two papers were not described.

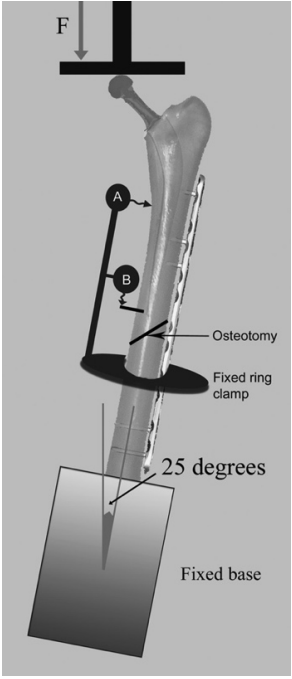
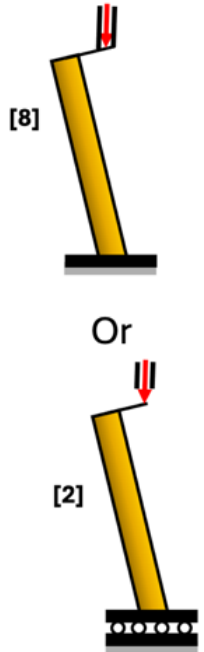
**Table 6.** Results from the literature review: Parameters regarding the biomechanical test setup extracted from studies focusing on femoral mid-shaft plate osteosynthesis.

No.	Title	Aim of the Study	Angle of the femur in °		Picture of the setup	Finite Element Model
			Frontal Plane	Sagittal Plane		
1	Effect of bone cement augmentation with different configurations of the dual locking plate for femoral allograft fixation: finite element analysis and biomechanical study (Wisanyotin <i>et al.</i> , 2023).	to investigate the effect of bone cement augmentation with different configurations of dual locking plates used for femoral allograft fixation.	15			 [8]

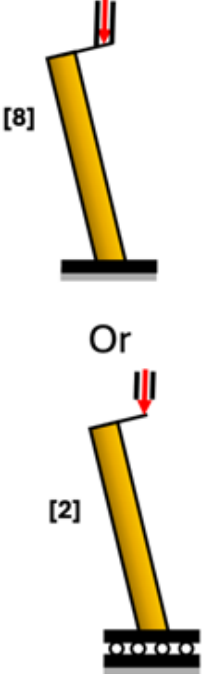
**Table 6.** Results from the literature review: Parameters regarding the biomechanical test setup extracted from studies focusing on femoral mid-shaft plate osteosynthesis. (Continued)

2	Biomechanical evaluation of fracture fixation constructs using a variable-angle locked periprosthetic femur plate system (Hoffmann <i>et al.</i> , 2014).	to compare the biomechanically stability and strength of three fixation constructs and identify the most desirable construct.	10			
---	---	---	----	--	---	---

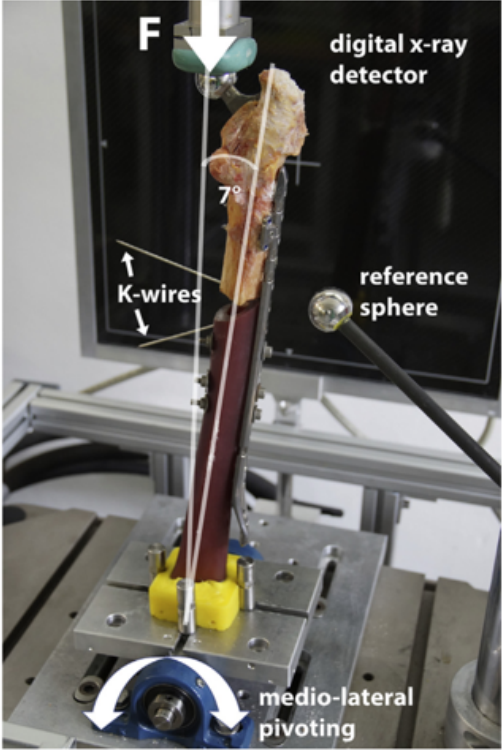
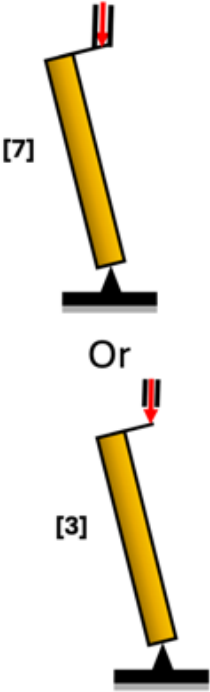
**Table 6.** Results from the literature review: Parameters regarding the biomechanical test setup extracted from studies focusing on femoral mid-shaft plate osteosynthesis. (Continued)

3	<p>Fixation of periprosthetic femoral shaft fractures associated with cemented femoral stems: a biomechanical comparison of locked plating and conventional cable plates (Fulkerson <i>et al.</i>, 2006).</p>	<p>to compare the stiffness and strength of locked plating to the Ogden construct for fixation of fractures occurring at the distal tip of well-fixed cemented femoral stems.</p>	25		
---	---	---	----	--	---

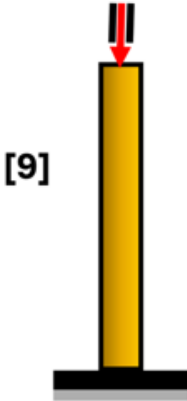
**Table 6.** Results from the literature review: Parameters regarding the biomechanical test setup extracted from studies focusing on femoral mid-shaft plate osteosynthesis. (Continued)

4	<p>Unstable Vancouver B1 periprosthetic femoral fracture fixation: A biomechanical comparison between a novel C-shaped memory alloy implant and cerclage wiring (Oh <i>et al.</i>, 2024).</p>	<p>to compare the biomechanical stability of the novel, C-clip implant with traditional cerclage wiring in fixation of a synthetic femoral fracture model of VB1 PFF</p>	25		
---	---	--	----	---	---

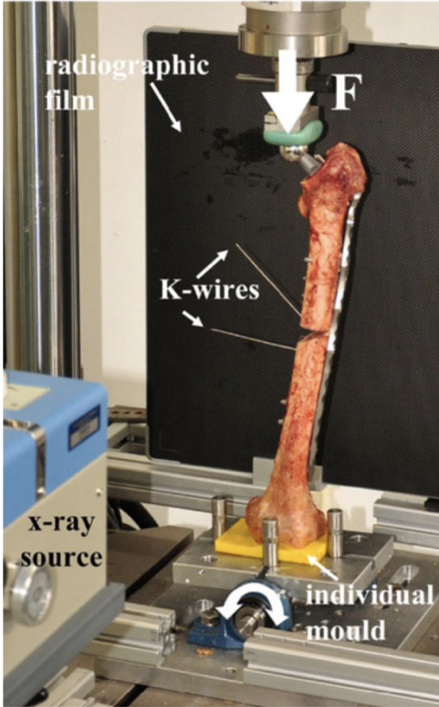
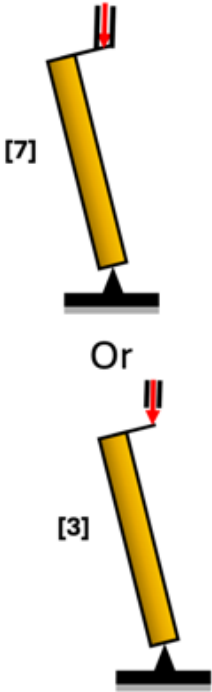
**Table 6.** Results from the literature review: Parameters regarding the biomechanical test setup extracted from studies focusing on femoral mid-shaft plate osteosynthesis. (Continued)

5	<p>Periprosthetic fracture fixation in Vancouver B1 femoral shaft fractures: A biomechanical study comparing two plate systems (Wähnert <i>et al.</i>, 2020).</p>	<p>to investigate the biomechanical characteristics of this newly developed plate and hinge construct in comparison to the standard LCP with LAP for the treatment of periprosthetic fractures in a Vancouver B1 fracture model</p>	7		
---	---	---	---	--	--

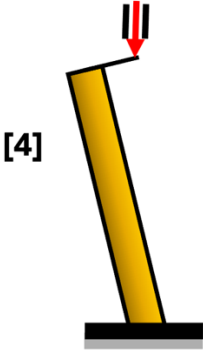
**Table 6.** Results from the literature review: Parameters regarding the biomechanical test setup extracted from studies focusing on femoral mid-shaft plate osteosynthesis. (Continued)

6	Comparison of five methods for locked-plate fixation of complex diaphyseal fractures (Pierret <i>et al.</i> , 2022).	Primary objective: to compare five constructs for locking-plate fixation of a complex femoral-diaphysis fracture model. Secondary objective: was to compare sub-groups of monocortical screw constructs, with the goal of identifying the construct most appropriate for diaphyseal-fracture fixation with prosthetic material within the intramedullary canal.	0	 <p>A photograph showing a femoral model (a yellowish, anatomically realistic bone) mounted vertically in a biomechanical testing machine. The machine is grey and black, with a red and white cylindrical component at the top. The femur is held in place by a metal fixture. The machine has yellow warning triangles at the base.</p>	 <p>A schematic diagram of a femoral model. It is a vertical yellow cylinder representing the bone, resting on a black base. A red arrow points downwards from the top of the cylinder, indicating an axial load. The number [9] is written to the left of the cylinder.</p>
---	--	---	---	---	---

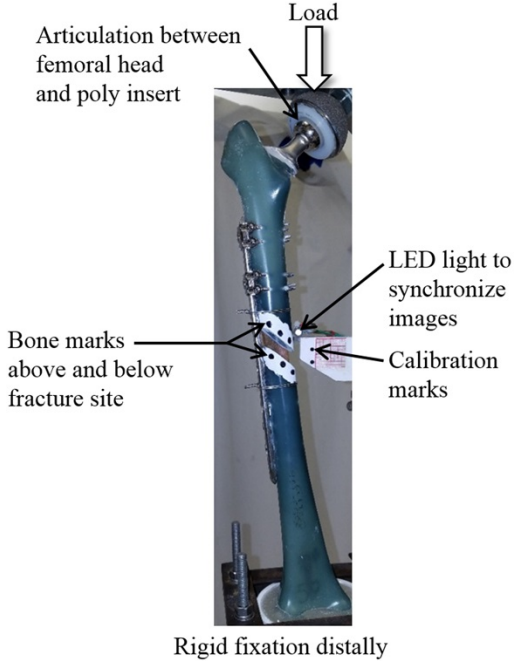
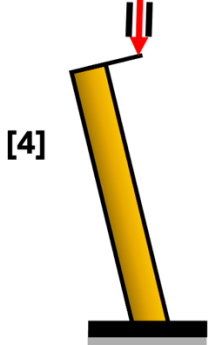
**Table 6.** Results from the literature review: Parameters regarding the biomechanical test setup extracted from studies focusing on femoral mid-shaft plate osteosynthesis. (Continued)

7	Biomechanical comparison of two angular stable plate constructions for periprosthetic femur fracture fixation (Dirk Wähnert <i>et al.</i> , 2013).	to investigate the currently two most popular internal fixation plate systems especially designed for periprosthetic femoral fractures: the fixed angle locking attachment plate (LAP®, Depuy Synthes®, Solothurn, Switzerland) and the variable angle non-contact bridging plate (NCB®, Zimmer GmbH, Winterthur, Switzerland).	7		
---	--	---	---	--	---

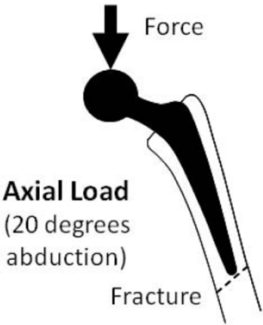
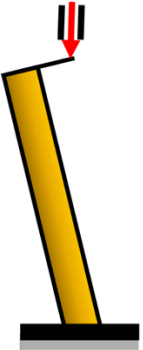
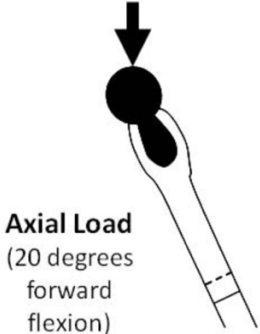
**Table 6.** Results from the literature review: Parameters regarding the biomechanical test setup extracted from studies focusing on femoral mid-shaft plate osteosynthesis. (Continued)

8	Comparison of different fixation techniques for periprosthetic fractures: a biomechanical study of a new implant (Konya <i>et al.</i> , 2021).	to determine the biomechanical comparison between different fixation techniques using our newly designed implants (the implant combines the plate with the U nail)	8		
---	--	--	---	---	---

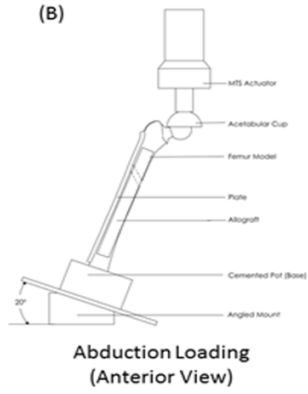
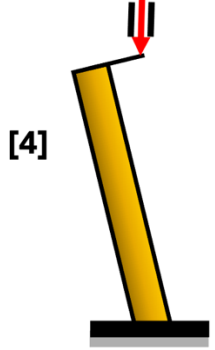
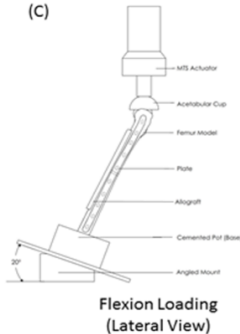
**Table 6.** Results from the literature review: Parameters regarding the biomechanical test setup extracted from studies focusing on femoral mid-shaft plate osteosynthesis. (Continued)

9	<p>Biomechanical Evaluation of Osteoporotic Proximal Femur Fractures with Proximal Bicortical Fixation and Allograft Struts (O’Connell <i>et al.</i>, 2018).</p>	<p>to evaluate the strength of proximal bicortical fixation using a novel osteoporotic synthetic bone model of Vancouver B1 PFF and to assess the influence of strut allograft augmentation. The secondary aim was to evaluate whether the strut position, either medial or anterior, influenced the strength of the construct.</p>	5		
---	--	---	---	--	---

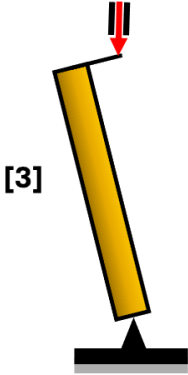
**Table 6.** Results from the literature review: Parameters regarding the biomechanical test setup extracted from studies focusing on femoral mid-shaft plate osteosynthesis. (Continued)

10	<p>The biomechanical analysis of three plating fixation systems for periprosthetic femoral fracture near the tip of a total hip arthroplasty (Lever <i>et al.</i>, 2010).</p>	<p>to assess the biomechanical performance immediately following surgery of 3 cable-plate and screw-plate fixation systems used to repair periprosthetic femur fractures near the tip of a total hip arthroplasty.</p>	20	 <p><b>Axial Load</b> (20 degrees abduction) Fracture</p>	<p>[4]</p> 
			20	 <p><b>Axial Load</b> (20 degrees forward flexion)</p>	<p>Not applicable</p>

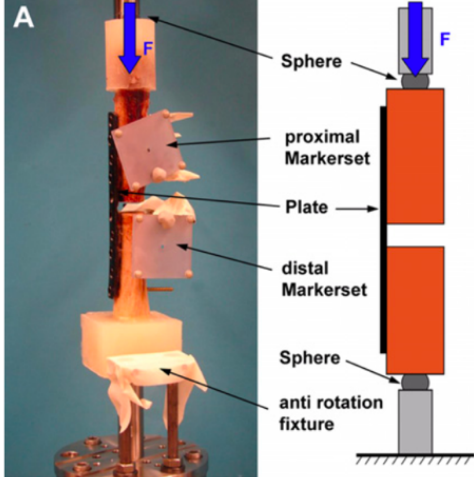
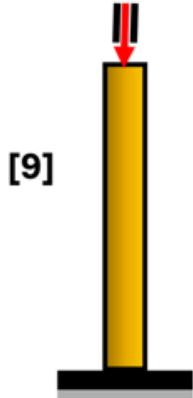
**Table 6.** Results from the literature review: Parameters regarding the biomechanical test setup extracted from studies focusing on femoral mid-shaft plate osteosynthesis. (Continued)

11	Do Transcortical Screws in a Locking Plate Construct Improve the Stiffness in the Fixation of Vancouver B1 Periprosthetic Femur Fractures? A Biomechanical Analysis of 2 Different Plating Constructs (Lochab <i>et al.</i> , 2017).	to compare the biomechanical performance of a conventional locking plate construct applied to the lateral femur with an anterior cortical strut allograft versus a locking plate with 2 LAP applied to the lateral femur without an anterior cortical strut allograft	20		 <p>(B) Abduction Loading (Anterior View)</p>	 <p>[4]</p>
			20		 <p>(C) Flexion Loading (Lateral View)</p>	Not applicable

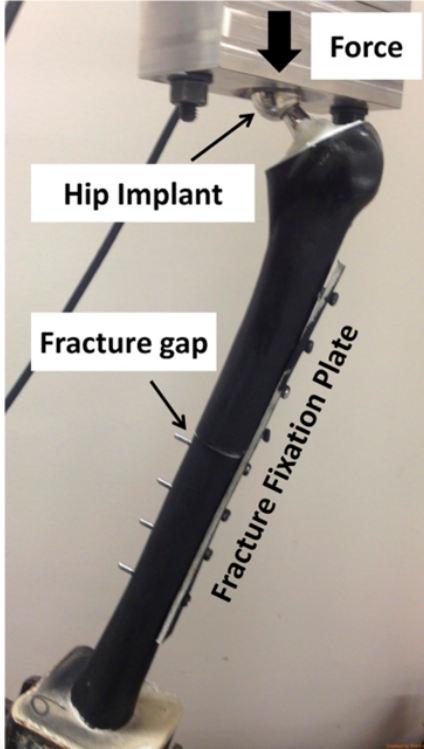
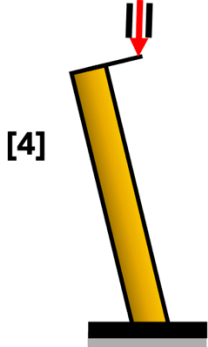
**Table 6.** Results from the literature review: Parameters regarding the biomechanical test setup extracted from studies focusing on femoral mid-shaft plate osteosynthesis. (Continued)

12	<p>Can plate osteosynthesis of periprosthetic femoral fractures cause cement mantle failure around a stable hip stem? A biomechanical analysis (Giesinger <i>et al.</i>, 2014).</p>	<p>to investigate cement mantle integrity and implant stability of a polished tapered stem in a PFF model under dynamic loading.</p>	7		N/A	
----	---	--	---	--	-----	---

**Table 6.** Results from the literature review: Parameters regarding the biomechanical test setup extracted from studies focusing on femoral mid-shaft plate osteosynthesis. (Continued)

<p>13</p>	<p>Biomechanical investigation of an alternative concept to angular stable plating using conventional fixation hardware (Windolf <i>et al.</i>, 2010).</p>	<p>to evaluate the biomechanical performance of a newly proposed crossed-screw concept ("Fence") utilizing conventional (non-locked) implants in comparison to conventional LC-DCP (limited contact dynamic compression plate) and LCP (locking compression plate) stabilization, in a human cadaveric diaphyseal gap model.</p>	<p>0</p>		
-----------	--	--	----------	---	---

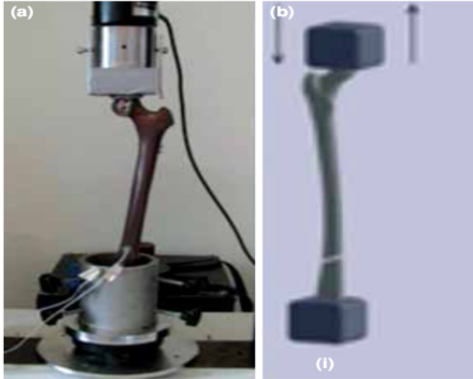
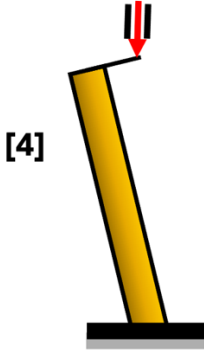
**Table 6.** Results from the literature review: Parameters regarding the biomechanical test setup extracted from studies focusing on femoral mid-shaft plate osteosynthesis. (Continued)

14	<p>Biomechanical analysis of a new carbon fiber/flax/epoxy bone fracture plate shows less stress shielding compared to a standard clinical metal plate (Bagheri <i>et al.</i>, 2014).</p>	<p>to determine the biomechanical performance of the current CF/Flax/Epoxy composite plate in fixing a Vancouver B1 fracture versus a standard clinically used metal bone plate</p>	15		
----	---	---	----	--	---

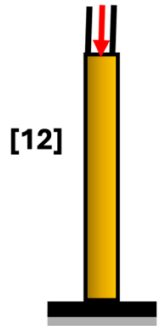
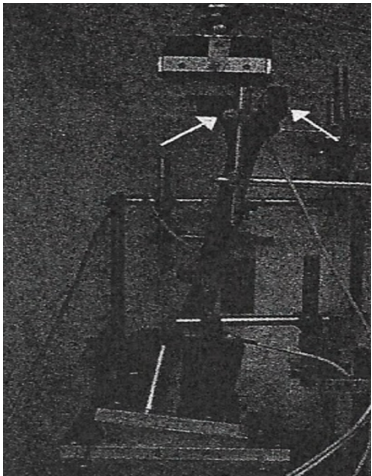
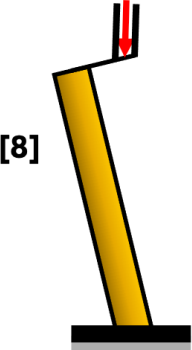
**Table 6.** Results from the literature review: Parameters regarding the biomechanical test setup extracted from studies focusing on femoral mid-shaft plate osteosynthesis. (Continued)

15	Plate fixation of periprosthetic femur fractures: What happens to the cement mantle? (Konstantinidis <i>et al.</i> , 2017).	(1) to examine whether damage of the cement mantle follows screw insertion (2) to determine the influence of three variables on the incidence of crack formation in the cement layer: screw type, cement mantle thickness, and position of the screw relative to the cement mantle and the prosthetic stem.	10		N/A	N/A
----	---	--	----	--	-----	-----

**Table 7.** Results from the literature review: Parameters regarding the biomechanical test setup extracted from studies focusing on intramedullary nails for mid-shaft fracture fixation.

No.	Title	Aim of the Study	Angle of the femur in °		Picture of the setup	Finite Element Model
			Frontal Plane	Sagittal Plane		
1	A new intramedullary sustained dynamic compression nail for the treatment of long bone fractures: a biomechanical study (Karakasli, Satoğlu and Havitçioğlu, 2015).	report an experimental assessment of the implant design (a new intramedullary sustained dynamic compressive nail (SDCN)) and compared it with the statically fixed standard intramedullary nail (SIMN)	N/A	N/A		 <p>[4]</p>

**Table 7.** Results from the literature review: Parameters regarding the biomechanical test setup extracted from studies focusing on intramedullary nails for mid-shaft fracture fixation. (Continued)

2	Increasing stability by pre-bending the nails in elastic stable intramedullary nailing: a biomechanical analysis of a synthetic femoral spiral fracture model (Kaiser <i>et al.</i> , 2012).	to determine the effects on stability of pre-bending the nails	0	N/A	 <p>[12]</p>
			9		 <p>[8]</p>

**Table 7.** Results from the literature review: Parameters regarding the biomechanical test setup extracted from studies focusing on intramedullary nails for mid-shaft fracture fixation. (Continued)

3	Modification of elastic stable intramedullary nailing with a 3rd nail in a femoral spiral fracture model - results of biomechanical testing and a prospective clinical study (Kaiser <i>et al.</i> , 2014).	to analyze the effect of a 3rd ESIN on stiffness, which is a valid stability parameter in biomechanical testing	9		N/A	N/A
			0		N/A	N/A
4	Biomechanical Analysis of Retrograde Flexible Intramedullary Nail Constructs in a Simulated Pediatric Femur Fracture Model (Bland <i>et al.</i> , 2019).	to compare the rotational and bending stiffness of 2 different FIMN constructs and 2 different materials in a simulated pediatric femur fracture model	7		N/A	N/A

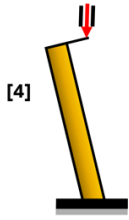
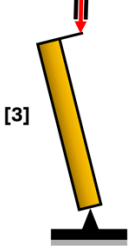
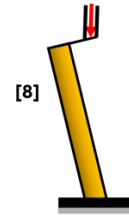
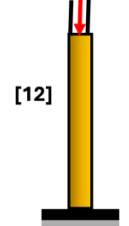
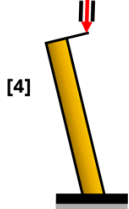
### 4.3 Discussion

The results from the literature review highlight significant variations in biomechanical test setups used in the literature to evaluate femoral diaphyseal implants. Table 8 summarizes the number of papers and corresponding models that align with the study's axial compression test setups.

**Table 8.** Results from the literature review: Number of papers and corresponding models similar to the axial compression test setups.

Model	Amount of paper
<b>Plate</b>	
<p>[8]</p>	1
<p>[8] Or [2]</p>	3
<p>[7] Or [3]</p>	2
<p>[9]</p>	2

**Table 8.** Results from the literature review: Number of papers and corresponding models similar to the axial compression test setups. (Continued)

Model	Amount of paper
 <p>[4]</p>	5
 <p>[3]</p>	1
N/A	1
<b>Nail</b>	
 <p>[8]</p>	1 (this paper conducted a second test where the setup is similar to 12)
 <p>[12]</p>	1 (same paper as model 8)
 <p>[4]</p>	1
N/A	2

Model 4 was used by five papers focusing on plate osteosynthesis for femoral mid-shaft fractures, making it the most used model. Model 9 was used by two papers and models 3 and 8 were each used by one paper.

Five papers did not provide a clear description of the test setup they employed for their axial compression tests, leading to two possible models that their setups might resemble. Among these, three papers likely used a setup similar to models 8 or 2, while the remaining two papers likely used a setup resembling models 7 or 3.

Results from the finite element analysis revealed that models 2, 3, and 4 exhibited high and non-constant bending moments along both the bone and plate. As discussed in Chapter I: Finite Element Analysis, plate positioning in these models is crucial, as improper placement can lead to localised stress concentrations that may influence test outcomes.

The studies using models 3 and 4, as well as those assumed to use models 2 and 3 due to unclear descriptions of the test setups, did not specify the exact height positioning of the plate (e.g., precise distance from anatomical landmarks like the lesser trochanter). Instead, they mostly only provided pictures of the implant fixation. Without detailed information on implant placement, comparing results across studies or replicating experiments becomes challenging, as slight positioning differences might influence the outcomes. For studies using models with high and non-constant bending moments and stress distributions in the bone and plate, such as models 2, 3, and 4, the lack of clear implant positioning details makes it difficult for other researchers to accurately replicate the setup and obtain comparable results.

For instance, in paper 14 (see Table 6), plate stress was measured among six specimens. Paper 14 used a setup similar to model 4, which exhibited non-constant and high variations in bending moment and stress along the plate. Differences in plate positioning across specimens could have led to inconsistent stress measurements, making it unreliable to compare results among the samples. Specimens with plates fixed in areas experiencing high bending moments would show higher plate stress compared to those with plates fixed in areas experiencing lower bending moments.

Paper 9 (see Table 6) assessed failure load using 30 specimens divided into three groups of ten. If plates were positioned in high-stress areas, the axial load needed to break them would be lower than for plates placed in low-stress areas, affecting result reliability.

Models with low bending moments and stress along the lateral plate (models 7, 8, and 9) were used in fewer studies. Specifically, three studies employed these models, and another five studies may have used them; however, due to unclear setup descriptions, this cannot be confirmed with certainty. It is important to note that, although models 7 and 9 exhibit non-constant bending moments and stress distributions along the plate, the variation is minimal and unlikely to significantly impact overall outcomes. Therefore, slight adjustments in plate positioning (e.g., more proximal or distal placement) could influence load distribution, but the effect may not be substantial enough to meaningfully alter implant performance in biomechanical testing.

Models 7 and 8 may be harder to replicate by other research groups, due to the femur being oriented at an angle. In contrast, model 9, with the femur oriented vertically, likely facilitates more consistent test replication. Compared to models 2, 3, and 4, these models (models 7, 8, and 9) may be more suitable for plate testing because the outcomes are less dependent on implant placement. This may make it possible to compare results with other studies using similar setups and allows other research groups to replicate the test more easily to validate the outcomes.

Only two papers, focusing on nails for mid-shaft fractures, provided descriptions or images of their axial compression test setups. One paper conducted two axial compression tests: the first test setup resembled model 8 and the second test resembled model 12. Another paper used a test setup similar to model 4. Model 8 and 12 exhibited low bending moments along the bone and nail, which may provide more realistic testing scenarios, as Taylor *et al.* (1996) and Duda, Schneider and Chao (1997) suggest that the bending moments in the femur during gait are minimized by muscle activity. Since the nail is fixed in the femur axis, it should ideally experience similar loading conditions as the bone. In contrast, model 4 exhibited non-constant and high bending moments along the bone and the nail, which may not replicate realistic testing scenarios for nails accurately.

In comparison to models 8 and 4, model 12 offers a simpler configuration, with the femur oriented vertically, making the test setup easier to replicate accurately by other research groups. Due to the non-constant loading of the nail and bone in model 4, researchers should be cautious when comparing results with other studies, as stress concentrations may occur in different regions along the nail's length, potentially affecting the reliability of outcomes. Paper 1 (see Table 7) used a setup similar to model 4 and measured strain using strain gauges. Due to the non-constant bending moment of the nail and bone, the strain level may vary based on where the strain gauges are fixed. If the strain gauges are fixed in an area where the nail or bone experiences high bending, the recorded strain will also be high. This variability can complicate the comparison of results across studies.

## 5 Discussion

This study aims to evaluate how proximal and distal displacement constraints applied to the femur during biomechanical testing impact the internal forces, moments, and stresses within the bone, as well as within implants like intramedullary nails and osteosynthesis plates.

This study focuses on femoral loading during gait, an activity that researchers frequently attempt to replicate in biomechanical testing (Lever *et al.*, 2010; O'Connell *et al.*, 2018; Wisanuyotin *et al.*, 2023). According to Duda, Schneider and Chao (1997), the femur is primarily loaded in compression during gait, with limited bending moments due to muscle activity. A study conducted by Taylor *et al.* (1996) also supports this theory, demonstrating that a compressive stress distribution in the diaphyseal femur is achievable and the muscles activity helps limit the bending moments experienced by the femur. Pauwels' (1980) analysis of stress in the lower limb during the single-limb support phase of gait revealed that muscles and ligaments help limit bending stress in the bone, which aligns with Duda's finding. Additionally, a study conducted by Munih, Kralj and Bajd (1992) also confirmed that the muscles significantly reduce the overall bending moment caused by joint reaction forces during standing in the femur and tibia. Based on this evidence, the most realistic loading scenario for biomechanical testing of the femur under gait conditions would result in an axial loading of the bone. However, it is important to note that the exact loading conditions in vivo have not yet been assessed in detail, and the uncertainty regarding the precise loading conditions that occur in the femur during gait remains.

Among the twelve models developed in this study, models 2 to 6 exhibited non-constant and high bending moments and stress along the bone, plate, and nail. As a result, these models may not be suitable for testing osteosynthesis plate, as they lack predictable loading along the bone's length, resulting in setups where the outcomes are sensitive to the implant's position.

The bending moments along the bone for models 1, 7, 9, 10, 11, and 12 were 0 Nm, while model 8 exhibited non-constant but minimum variation in bending moments along the bone. Although these models do not fully align with the theories of Taylor *et al.* (1996) and Duda, Schneider and Chao (1997)—who suggest that muscle activity helps to minimize (but not completely eliminate) bending moments in the femur—these models produce predictable loading along the bone's length compared to models 2 to 6. Additionally, models 1, 8, 10, 11, and 12 exhibited constant bending moments along the plate. The constant and predictable loading along the bone and plate in these models (1, 8, 10, 11, and 12) eliminate the sensitivity of test outcomes to variations in plate positioning. Models 1, 10, 11, and 12, with the femur in a vertical orientation, offer simpler setups. However, models 11 and 12 exhibited zero bending moments in the plate, making them unsuitable for testing, as plates need to undergo bending to properly assess their structural integrity and failure risk. On the assumption that Taylor *et al.* (1996) and Duda, Schneider and Chao (1997) are correct that the femur is primarily loaded in compression with limited bending moments during gait, models 1 and 10 are suggested as the most appropriate for plate testing under gait conditions due to their simple setup and ability to produce predictable and quantified loading. The constant and predictable loading along the bone's length in these models reduces the sensitivity of the test outcomes to plate positioning.

For testing intramedullary nails, models 1, 7, 8, 9, 10, and 12 are suggested to be the most appropriate due to their low bending moments in the bone compared to models 2 to 6. Since the intramedullary nail is implanted in the femur's axis, the bending moment experienced by the nail should closely match the bending moment experienced by the femur. According to Pauwels (1980), Munić, Kralj and Bajd (1992), Taylor *et al.* (1996), and Duda, Schneider and Chao (1997), the bending moments experienced by the femur are minimized by muscle activity, suggesting that realistic testing scenarios should involve low bending moments in the bone. The constant loading of the nail and bone in these models produces predictable

loading along the bone and nail's length and reduces the likelihood of stress concentration that could influence test outcomes.

Furthermore, the analytical modelling results for these models indicated that the bending moment in the nail is lower than in the plate. This aligns with the theory that nails experience lower bending than plates due to its position in the femur axis, further supporting the idea that these models (1, 7, 8, 9, 10, and 12) may represent realistic scenarios for nail testing. However, models 7 and 8, where the femur is oriented at an angle, may be more challenging to set up compared to models 1, 9, 10, and 12.

These results from the finite element analysis indicate that the proximal and distal displacement constraints affect the internal forces, moments, and stresses in the bone and implants, emphasizing the need for careful consideration when selecting test setups. It is important to acknowledge that while this study focuses on simulating gait, there are other activities—such as stumbling—that are more complex to reproduce in testing environments and can lead to implant failure. Additionally, the finely coordinated muscle forces that are necessary to ensure axial loading, may be damaged during bone fracture. This could influence choices of the biomechanical test setups.

The literature review reveals significant variations in biomechanical testing setups for evaluating femoral diaphyseal implants. Out of 19 papers focused on mid-shaft femur fractures, seven papers employed test setups similar to models 3 and 4, which exhibited high and non-constant bending moments and stress along the bone and implants. As discussed in Chapter I: Finite Element Analysis, the implant position in these models can potentially influence the test outcomes. These papers also did not clearly specify where the implants were fixed, making it almost impossible for other researchers to compare the results or replicate the tests.

Four papers used models 8, 9, and 12, which exhibited low and constant loading and stress along the bone and implants, thereby eliminating the sensitivity of the outcomes to the implant positioning. Five papers lacked clear descriptions of their testing setups, making it difficult to accurately categorize them into the twelve models; these setups could correspond either to models with high and non-constant loading and stress along the bone and implants

or to models with low and constant loading and stress. The remaining three papers did not provide any information or pictures of their test setups.

The variations in biomechanical test setups, combined with the lack of clear descriptions for both test setups and implant positioning, suggest that results from many biomechanical tests may be difficult to verify and that some studies may have used unsuitable and ineffective test setups for addressing their objectives. These variations further emphasize the need for standardized testing setups for evaluating femoral implants for mid-shaft fractures.

## **5.1 Limitations**

First, the study focused on a limited range of physiological loads, specifically a one-legged stance during gait. Dynamic activities, like running and jumping, which generate higher loads, strains, and stresses on the implant, were not included. This focus may limit the applicability of the findings for studies aiming to test implants under a broader range of activities beyond gait. However, many biomechanical test setups attempt to replicate the one-legged stance of gait, making femoral loading during gait an appropriate focus for the finite element analysis (FEA).

The finite element analysis (FEA) in this study considered only small deformations. Incorporating large deformation analysis could be valuable for observing how shape changes in the bone, plate, and nail impact stress distribution, deformation patterns, and distal reaction forces, particularly under high-load conditions. Such shape alterations could influence the stress and strain responses and thus alter the study's outcomes. Some of the models used in this study had rigid constraints, while others had less rigid constraints. In setups with rigid constraints, large deformations are not expected. In contrast, setups with less rigid constraints allow for greater deformation, making large deformation analysis necessary. Additionally, models exhibiting higher bending moments along the bone and implants tend to produce higher strain levels, making large deformations have higher impact on these models. The models recommended by the study for implant testing demonstrated low bending moments, resulting in lower strain levels, where large deformations have a minimal effect.

Additionally, the finite element models used in the study were simplified and did not fully capture the complexity of the femur and plate geometries. The simplified bone and plate geometries limit the accuracy of the stress and bending moment predictions.

A further limitation is the lack of experimental validation for the FEA results. Conducting experimental validation could have enhanced the reliability of the FEA findings by comparing simulated outcomes with actual biomechanical test data, thus strengthening confidence in the model's accuracy.

Additionally, this study only considered movements in 2D, whereas in real-world scenarios, the femur and implants experience motion and forces in three dimensions during activities like walking or running. For instance, during gait, the hip contact force has multiple directional components, but only the vertical component ( $F_y$ ) was applied in the finite element analysis.

Lastly, the study considered displacement constraints only in 2D, while in actual biomechanical testing, displacement constraints are applied in 3D. This limitation restricts the ability to evaluate the appropriateness of certain test setups found in the literature review chapter. For example, setups with the femur oriented in forward flexion, where the femur is angled in sagittal plane, could not be reviewed due to the study's 2D approach.

## **6 Conclusion**

Diaphyseal femur fractures, also known as femoral shaft fractures, are among the most common injuries in orthopaedic practice (Denisiuk and Afsari, 2023). Intramedullary nails and osteosynthesis plates are two common treatments for diaphyseal femur fractures. Both implants need to undergo preclinical testing to ensure their safety, durability, and effectiveness. Preclinical testing can be categorized into two types: biomechanical testing and mechanical testing for regulatory purposes (Schorler *et al.*, 2017). This study focuses on biomechanical testing, which involves fixing the implants to cadaveric or synthetic bones, which are osteotomized to simulate specific types of fractures. The bone-implant construct is then subjected to loading conditions, which closely resemble physiological scenarios (Schorler *et al.*, 2017).

Biomechanical test setups in studies on implants for diaphyseal femur fractures show considerable variation, particularly in the design of the distal and proximal test fixtures used to hold the femurs during testing. This study aims to investigate how proximal and distal displacement constraints of the femur during biomechanical testing impact internal forces, moments, and stresses within the bone, osteosynthesis nails, and laterally mounted plates. Initially, finite element analysis and analytical modelling were used to examine these effects. Subsequently, a literature review of studies on implants for femoral mid-shaft fractures was conducted to evaluate the suitability and effectiveness of the biomechanical test setups used in these studies to address their objectives.

Many biomechanical tests for implants attempt to replicate the one legged-stance phase during gait. According to Taylor *et al.* (1996) and Duda, Schneider and Chao (1997), during gait, the femur is primarily loaded in axial compression, with muscle activity limiting bending moments. Studies conducted by Pauwels (1980) and Munih, Kralj and Bajd (1992) also revealed that muscles and ligaments play a crucial role in reducing bending stresses in bones and help limit bending moments in the femur. These theories are also supported by the observation that, although stress increases linearly with applied load, which means people with higher body weights would experience higher stress in their femurs while walking, potentially leading to fractures if the stress exceeds the cortical bone's yield strength. In reality, people with higher body weights do not typically fracture their femurs from walking alone. This suggests that the stress on the femur during walking is lower than initially expected. Together, these theories support the idea that realistic loading to be applied to the femur during biomechanical testing to replicate gait may be axial compression.

In the first chapter, twelve finite element models were created with different sets of proximal/distal constraints. The results indicate that proximal and distal displacement constraints affect internal forces, moments, and stresses in the bone, nails, and plates. This finding highlights the importance of carefully selecting proximal and distal displacement constraints in biomechanical testing, as certain setups can influence test outcomes by introducing additional variables, such as implant positioning. For instance, models 2 to 6 developed in this study exhibited non-constant loading along the bone and implants, resulting in setups where the outcomes are sensitive to the implant's position.

In the second chapter, a review of studies on mid-shaft femoral fractures revealed significant variations in biomechanical test setups. Setups where the outcomes are sensitive to the implant's position/placement are difficult to replicate unless precise implant placement details are provided, which may prevent other research groups from verifying the results. This review also revealed that many papers may have employed unsuitable and ineffective test setups to address their study's objectives.

In conclusion, the results of this study showed that proximal and distal displacement constraints have a significant effect on the internal loads, moments, and stress distribution along the bone, plate, and nail during biomechanical testing. The literature review further revealed variations in biomechanical test setups used in studies focusing on implants for femur mid-shaft fractures. These variations suggest that researchers need to be more cautious when comparing results across studies. It also emphasizes the urgent need for standardization in biomechanical testing setups to ensure more reliable and comparable results across studies.

## Bibliography

- Abdelaal, A.H.K. *et al.* (2016) 'The linea aspera as a guide for femoral rotation after tumor resection: is it directly posterior? A technical note', *Journal of Orthopaedics and Traumatology*, 17(3), pp. 255–259. Available at: <https://doi.org/10.1007/s10195-016-0399-6>.
- About ISO (no date) ISO. Available at: <https://www.iso.org/about> (Accessed: 25 October 2024).
- Agarwal-Harding, K.J. *et al.* (2015) 'Estimating the Global Incidence of Femoral Fracture from Road Traffic Collisions: A Literature Review', *JBJS*, 97(6), p. e31. Available at: <https://doi.org/10.2106/JBJS.N.00314>.
- 'Ansys 2024 R1 Student' (2024). Ansys.
- AO Foundation (2018) *AO/OTA Fracture and Dislocation Classification* [Brochure]. Switzerland.
- Arfken, G.B. *et al.* (1984) 'chapter 12 - ROTATION OF A RIGID BODY', in G.B. Arfken *et al.* (eds) *University Physics*. Academic Press, pp. 230–255. Available at: <https://doi.org/10.1016/B978-0-12-059860-1.50017-5>.
- Arndt, K.-D., Brüggemann, H. and Ihme, J. (2021) 'Einfache Beanspruchungen', in K.-D. Arndt, H. Brüggemann, and J. Ihme (eds) *Festigkeitslehre für Wirtschaftsingenieure: Mit Verständnisfragen, vielen Beispielen und Aufgaben mit kleinschrittigen Lösungen*. Wiesbaden: Springer Fachmedien, pp. 41–155. Available at: [https://doi.org/10.1007/978-3-658-33548-9\\_2](https://doi.org/10.1007/978-3-658-33548-9_2).
- ASTM Fact Sheet - Overview - About Us* (no date) ASTM INTERNATIONAL. Available at: <https://www.astm.org/about/overview/fact-sheet.html> (Accessed: 25 October 2024).
- Attum, B. and Pilson, H. (2023) 'Intertrochanteric Femur Fracture', in *StatPearls*. Treasure Island (FL): StatPearls Publishing. Available at: <http://www.ncbi.nlm.nih.gov/books/NBK493161/> (Accessed: 23 October 2024).
- Augat, P. *et al.* (2006) 'Shear movement at the fracture site delays healing in a diaphyseal fracture model', *Journal of Orthopaedic Research*, 21(6), pp. 1011–1017. Available at: [https://doi.org/10.1016/S0736-0266\(03\)00098-6](https://doi.org/10.1016/S0736-0266(03)00098-6).
- Augat, P. and von Rüden, C. (2018) 'Evolution of fracture treatment with bone plates', *Injury*, 49, pp. S2–S7. Available at: [https://doi.org/10.1016/S0020-1383\(18\)30294-8](https://doi.org/10.1016/S0020-1383(18)30294-8).

- Baar, S. (2022) 'Biegebeanspruchung', in S. Baar (ed.) *Lohmeyer Baustatik 2: Bemessung und Sicherheitsnachweise*. Wiesbaden: Springer Fachmedien, pp. 99–174. Available at: [https://doi.org/10.1007/978-3-658-32240-3\\_4](https://doi.org/10.1007/978-3-658-32240-3_4).
- Bäcker, H.C. *et al.* (2022) 'Breakage of intramedullary femoral nailing or femoral plating: how to prevent implant failure', *European Journal of Medical Research*, 27(1), p. 7. Available at: <https://doi.org/10.1186/s40001-021-00630-7>.
- Bagheri, Z.S. *et al.* (2014) 'Biomechanical Analysis of a New Carbon Fiber/Flax/Epoxy Bone Fracture Plate Shows Less Stress Shielding Compared to a Standard Clinical Metal Plate', *Journal of Biomechanical Engineering*, 136(091002). Available at: <https://doi.org/10.1115/1.4027669>.
- Baig, M.A. and Bacha, D. (2023) 'Histology, Bone', in *StatPearls*. Treasure Island (FL): StatPearls Publishing. Available at: <http://www.ncbi.nlm.nih.gov/books/NBK541132/> (Accessed: 23 October 2024).
- Baleani, M. *et al.* (2024) 'Tensile Yield Strain of Human Cortical Bone from the Femoral Diaphysis Is Constant among Healthy Adults and across the Anatomical Quadrants', *Bioengineering*, 11(4), p. 395. Available at: <https://doi.org/10.3390/bioengineering11040395>.
- Barber, C.C. *et al.* (2021) 'A systematic review of the use of titanium versus stainless steel implants for fracture fixation', *OTA International*, 4(3), p. e138. Available at: <https://doi.org/10.1097/OI9.0000000000000138>.
- Barth, T. *et al.* (2022) 'Additive manufactured versus traditional osteosynthesis plates - a finite element analysis', *Transactions on Additive Manufacturing Meets Medicine*, 4(1), pp. 644–644. Available at: <https://doi.org/10.18416/AMMM.2022.2209644>.
- Bazyar, P. *et al.* (2023) 'An Overview of Selected Material Properties in Finite Element Modeling of the Human Femur', *Biomechanics*, 3(1), pp. 124–135. Available at: <https://doi.org/10.3390/biomechanics3010012>.
- Bergmann, G. *et al.* (2001) 'Hip contact forces and gait patterns from routine activities', *Journal of Biomechanics*, 34(7), pp. 859–871. Available at: [https://doi.org/10.1016/S0021-9290\(01\)00040-9](https://doi.org/10.1016/S0021-9290(01)00040-9).
- Bergmann, G., Graichen, F. and Rohlmann, A. (1993) 'Hip joint loading during walking and running, measured in two patients', *Journal of Biomechanics*, 26(8), pp. 969–990. Available at: [https://doi.org/10.1016/0021-9290\(93\)90058-M](https://doi.org/10.1016/0021-9290(93)90058-M).

- Betts, J.G. *et al.* (2022) *Anatomy and Physiology 2e*. OpenStax. Available at: <https://openstax.org/books/anatomy-and-physiology-2e/pages/11-6-appendicular-muscles-of-the-pelvic-girdle-and-lower-limbs> (Accessed: 23 October 2024).
- Bhanushali, A. *et al.* (2022) ‘Outcomes of early versus delayed weight-bearing with intramedullary nailing of tibial shaft fractures: a systematic review and meta-analysis’, *European Journal of Trauma and Emergency Surgery*, 48(5), pp. 3521–3527. Available at: <https://doi.org/10.1007/s00068-022-01919-w>.
- Björnsdóttir, M. (2014) *Influence of Muscle Forces on Stresses in the Human Femur*. Available at: <https://www.diva-portal.org/smash/get/diva2:839895/FULLTEXT01.pdf>.
- Bland, D.C. *et al.* (2019) ‘Biomechanical Analysis of Retrograde Flexible Intramedullary Nail Constructs in a Simulated Pediatric Femur Fracture Model’, *Journal of Pediatric Orthopedics*, 39(1), pp. 22–27. Available at: <https://doi.org/10.1097/BPO.0000000000000946>.
- Bluemel, J. *et al.* (2015) *The Nonhuman Primate in Nonclinical Drug Development and Safety Assessment*. Available at: <https://doi.org/10.1016/C2013-0-04736-6> (Accessed: 23 October 2024).
- Böge, A. (2011) ‘Festigkeitslehre’, in A. Böge (ed.) *Technische Mechanik: Statik – Dynamik – Fluidmechanik – Festigkeitslehre*. Wiesbaden: Vieweg+Teubner Verlag, pp. 261–384. Available at: [https://doi.org/10.1007/978-3-8348-8107-6\\_5](https://doi.org/10.1007/978-3-8348-8107-6_5).
- Burr, D.B., Bellido, T. and White, K.E. (2015) ‘6 - Bone structure and function’, in M.C. Hochberg *et al.* (eds) *Rheumatology (Sixth Edition)*. 6th edn. Philadelphia: Mosby, pp. 42–55. Available at: <https://doi.org/10.1016/B978-0-323-09138-1.00006-1>.
- Chang, A. *et al.* (2023) ‘Anatomy, Bony Pelvis and Lower Limb: Femur’, in *StatPearls Treasure Island (FL): StatPearls Publishing*. Available at: <http://www.ncbi.nlm.nih.gov/books/NBK532982/> (Accessed: 23 October 2024).
- Chang, C.-M. *et al.* (2017) ‘An anatomical study of the proximal aspect of the medial femoral condyle to define the proximal-distal condylar length’, *Tzu Chi Medical Journal*, 29(2), p. 104. Available at: [https://doi.org/10.4103/tcmj.tcmj\\_30\\_17](https://doi.org/10.4103/tcmj.tcmj_30_17).
- Chao, A.H., McCann, G.A. and Fowler, J.M. (2014) ‘Alternatives to commonly used pelvic reconstruction procedures in gynecologic oncology’, *Gynecologic Oncology*, 134(1), pp. 172–180. Available at: <https://doi.org/10.1016/j.ygyno.2014.04.059>.

- Chen, H. *et al.* (2024) ‘A modified testing method based on ASTM F382 considering the practical physiological loading and boundary conditions applying on bone plates’, *Measurement*, 241. Available at: <https://doi.org/10.1016/j.measurement.2024.115691>.
- Cheung, G. *et al.* (2004) ‘Finite element analysis of a femoral retrograde intramedullary nail subject to gait loading’, *Medical Engineering & Physics*, 26(2), pp. 93–108. Available at: <https://doi.org/10.1016/j.medengphy.2003.10.006>.
- Clarke, B. (2008) ‘Normal Bone Anatomy and Physiology’, *Clinical Journal of the American Society of Nephrology*, 3(Supplement\_3), p. S131. Available at: <https://doi.org/10.2215/CJN.04151206>.
- Coon, M.S. and Best, B.J. (2023) ‘Distal Femur Fractures’, in *StatPearls*. Treasure Island (FL): StatPearls Publishing. Available at: <http://www.ncbi.nlm.nih.gov/books/NBK551675/> (Accessed: 23 October 2024).
- Cornelius, C.-P. *et al.* (2014) ‘The Comprehensive AOCMF Classification System: Glossary of Common Terminology’, *Craniomaxillofacial Trauma & Reconstruction*, 7(1), pp. 136–140. Available at: <https://doi.org/10.1055/s-0034-1390072>.
- Cowan, P.T., Launico, M.V. and Kahai, P. (2024) ‘Anatomy, Bones’, in *StatPearls*. Treasure Island (FL): StatPearls Publishing. Available at: <http://www.ncbi.nlm.nih.gov/books/NBK537199/> (Accessed: 23 October 2024).
- Davidovits, P. (2013) ‘Basic Concepts in Mechanics’, in P. Davidovits (ed.) *Physics in Biology and Medicine (Fourth Edition)*. Boston: Academic Press (Complementary Science), pp. 275–287. Available at: <https://doi.org/10.1016/B978-0-12-386513-7.00019-9>.
- Denisiuk, M. and Afsari, A. (2023) ‘Femoral Shaft Fractures’, in *StatPearls*. Treasure Island (FL): StatPearls Publishing. Available at: <http://www.ncbi.nlm.nih.gov/books/NBK556057/> (Accessed: 23 October 2024).
- Downey, P.A. and Siegel, M.I. (2006) ‘Bone Biology and the Clinical Implications for Osteoporosis’, *Physical Therapy*, 86(1), pp. 77–91. Available at: <https://doi.org/10.1093/ptj/86.1.77>.
- Duda, G.N., Schneider, E. and Chao, E.Y.S. (1997) ‘Internal forces and moments in the femur during walking’, *Journal of Biomechanics*, 30(9), pp. 933–941. Available at: [https://doi.org/10.1016/S0021-9290\(97\)00057-2](https://doi.org/10.1016/S0021-9290(97)00057-2).
- Egol, K.A. *et al.* (2004) ‘Biomechanics of Locked Plates and Screws’, *Journal of Orthopaedic Trauma*, 18(8), p. 488.

- El Beaino, M. *et al.* (2019) 'Biomechanical Evaluation of Dual Plate Configurations for Femoral Shaft Fracture Fixation', *BioMed Research International*, 2019(1), p. 5958631. Available at: <https://doi.org/10.1155/2019/5958631>.
- ElHawary, H. *et al.* (2021) 'Bone Healing and Inflammation: Principles of Fracture and Repair', *Seminars in Plastic Surgery*, 35(03), pp. 198–203. Available at: <https://doi.org/10.1055/s-0041-1732334>.
- Eveleigh, R. (1997) *A biomechanical evaluation of intramedullary nails during simulated fracture healing*. Doctoral Thesis. University of Bath. Available at: <https://researchportal.bath.ac.uk/en/studentTheses/a-biomechanical-evaluation-of-intramedullary-nails-during-simulat> (Accessed: 24 October 2024).
- Eveleigh, R.J. (1995) 'A review of biomechanical studies of intramedullary nails', *Medical Engineering & Physics*, 17(5), pp. 323–331. Available at: [https://doi.org/10.1016/1350-4533\(95\)97311-C](https://doi.org/10.1016/1350-4533(95)97311-C).
- Fice, J. and Chandrashekar, N. (2012) 'TAPERED FRACTURE FIXATION PLATE REDUCES BONE STRESS SHIELDING: A COMPUTATIONAL STUDY', *Journal of Mechanics in Medicine and Biology*, 12. Available at: <https://doi.org/10.1142/S021951941200506X>.
- Fong, E.L.S., Chan, C.K. and Goodman, S.B. (2011) 'Stem cell homing in musculoskeletal injury', *Biomaterials*, 32(2), pp. 395–409. Available at: <https://doi.org/10.1016/j.biomaterials.2010.08.101>.
- Fulkerson, E. *et al.* (2006) 'Fixation of Periprosthetic Femoral Shaft Fractures Associated With Cemented Femoral Stems: A Biomechanical Comparison of Locked Plating and Conventional Cable Plates', *Journal of Orthopaedic Trauma*, 20(2), pp. 89–93. Available at: <https://doi.org/10.1097/01.bot.0000199119.38359.96>.
- Gage, J.R., DeLuca, P.A. and Renshaw, T.S. (1996) 'Gait analysis: principle and applications with emphasis on its use in cerebral palsy', *Instructional Course Lectures*, 45, pp. 491–507.
- Gautam, D. and Rao, V.K.P. (2019) 'Classification of diaphysis based on the mechanical response of femur bone', *Vibroengineering Procedia*, 29, pp. 182–188. Available at: <https://doi.org/10.21595/vp.2019.21133>.
- Gebhardt, C. (2014) 'Praxisbuch FEM mit ANSYS Workbench', in *Praxisbuch FEM mit ANSYS Workbench*. Carl Hanser Verlag GmbH & Co. KG, p. I–IX. Available at: <https://doi.org/10.3139/9783446439566.fm>.

- Gervais, B. *et al.* (2016) ‘Failure analysis of a 316L stainless steel femoral orthopedic implant’, *Case Studies in Engineering Failure Analysis*, 5–6, pp. 30–38. Available at: <https://doi.org/10.1016/j.csefa.2015.12.001>.
- Ghiasi, M.S. *et al.* (2017) ‘Bone fracture healing in mechanobiological modeling: A review of principles and methods’, *Bone Reports*, 6, pp. 87–100. Available at: <https://doi.org/10.1016/j.bonr.2017.03.002>.
- Giannoudis, P.V., Pape, H.C. and Schütz, M. (no date a) *Simple, oblique, proximal 1/3 fractures*, *AO SURGERY REFERENCE*. Available at: <https://surgeryreference.aofoundation.org/orthopedic-trauma/adult-trauma/femoral-shaft/simple-oblique-middle-1-3-fractures/definition> (Accessed: 24 October 2024).
- Giannoudis, P.V., Pape, H.C. and Schütz, M. (no date b) *Simple, spiral, middle 1/3 fractures*, *AO SURGERY REFERENCE*. Available at: <https://surgeryreference.aofoundation.org/orthopedic-trauma/adult-trauma/femoral-shaft/simple-spiral-middle-1-3-fractures/definition> (Accessed: 24 October 2024).
- Giannoudis, P.V., Pape, H.C. and Schütz, M. (no date c) *Simple, transverse, middle 1/3 fractures*, *AO SURGERY REFERENCE*. Available at: <https://surgeryreference.aofoundation.org/orthopedic-trauma/adult-trauma/femoral-shaft/simple-transverse-middle-1-3-fractures/definition> (Accessed: 24 October 2024).
- Giannoudis, P.V., Pape, H.C. and Schütz, M. (no date d) *Wedge, intact, middle 1/3 fractures*, *AO SURGERY REFERENCE*. Available at: <https://surgeryreference.aofoundation.org/orthopedic-trauma/adult-trauma/femoral-shaft/wedge-intact-middle-1-3-fractures/definition#> (Accessed: 24 October 2024).
- Giesinger, K. *et al.* (2014) ‘Can Plate Osteosynthesis of Periprosthetic Femoral Fractures Cause Cement Mantle Failure Around a Stable Hip Stem? A Biomechanical Analysis’, *The Journal of Arthroplasty*, 29(6), pp. 1308–1312. Available at: <https://doi.org/10.1016/j.arth.2013.12.015>.
- Grabowski, K. *et al.* (2022) ‘Recent advances in MXene-based sensors for Structural Health Monitoring applications: A review’, *Measurement*, 189, p. 110575. Available at: <https://doi.org/10.1016/j.measurement.2021.110575>.
- Grisell, M., Moed, B.R. and Bledsoe, J.G. (2010) ‘A Biomechanical Comparison of Trochanteric Nail Proximal Screw Configurations in a Subtrochanteric Fracture Model’, *Journal of Orthopaedic Trauma*, 24(6), p. 359. Available at: <https://doi.org/10.1097/BOT.0b013e3181c6b17f>.

- Gurevitch, O., Slavin, S. and Feldman, A.G. (2007) ‘Conversion of red bone marrow into yellow – Cause and mechanisms’, *Medical Hypotheses*, 69(3), pp. 531–536. Available at: <https://doi.org/10.1016/j.mehy.2007.01.052>.
- Haddad, B. *et al.* (2022) ‘Femoral neck shaft angle measurement on plain radiography: is standing or supine radiograph a reliable template for the contralateral femur?’, *BMC Musculoskeletal Disorders*, 23(1), p. 1092. Available at: <https://doi.org/10.1186/s12891-022-06071-5>.
- Hak, D.J. *et al.* (2010) ‘The Influence of Fracture Fixation Biomechanics on Fracture Healing’, *Orthopedics*, 33(10), pp. 752–755. Available at: <https://doi.org/10.3928/01477447-20100826-20>.
- Hamill, J. and Knutzen, K.M. (2006) *Biomechanical Basis of Human Movement*. Lippincott Williams & Wilkins.
- Harten, U. (ed.) (2009) ‘Mechanik starrer Körper’, in *Physik: Einführung für Ingenieure und Naturwissenschaftler*. Berlin, Heidelberg: Springer, pp. 31–92. Available at: [https://doi.org/10.1007/978-3-540-89101-7\\_2](https://doi.org/10.1007/978-3-540-89101-7_2).
- Harty, M. (1984) ‘The Anatomy of the Hip Joint’, in R.G. Tronzo (ed.) *Surgery of the Hip Joint: Volume 1*. New York, NY: Springer, pp. 45–74. Available at: [https://doi.org/10.1007/978-1-4612-5224-5\\_3](https://doi.org/10.1007/978-1-4612-5224-5_3).
- Helguero, C.G., Ramírez, E.A. and Amaya, J.L. (2019) ‘Engineering interface inside the operative room: design and simulation of a fracture-plate bending machine’, *Procedia CIRP*, 79, pp. 655–660. Available at: <https://doi.org/10.1016/j.procir.2019.02.053>.
- Helmig, K., Kakish, S. and DeCoster, T. (2022) ‘Reaming Errors in Intramedullary Nailing’, *Western Journal of Orthopaedics*, 11(1). Available at: <https://digitalrepository.unm.edu/wjo/vol11/iss1/17>.
- Helmy, N. *et al.* (2008) ‘Muscle Function and Functional Outcome Following Standard Antegrade Reamed Intramedullary Nailing of Isolated Femoral Shaft Fractures’, *Journal of Orthopaedic Trauma*, 22(1), p. 10. Available at: <https://doi.org/10.1097/BOT.0b013e31815f5357>.
- Henle, P. (2008) ‘8 - Untere Extremität’, in I. Steinbrück and D. Baumhoer (eds) *Intensivkurs Anatomie*. Munich: Urban & Fischer, pp. 393–436. Available at: <https://doi.org/10.1016/B978-3-437-43670-3.50011-3>.
- Heyland, M. *et al.* (2017) ‘Stahl oder Titan bei der Osteosynthese’, *Der Unfallchirurg*, 120(2), pp. 103–109. Available at: <https://doi.org/10.1007/s00113-016-0289-7>.

- Hirtler, L., Kainberger, F. and Röhrich, S. (2022) ‘The intercondylar fossa—A narrative review’, *Clinical Anatomy*, 35(1), pp. 2–14. Available at: <https://doi.org/10.1002/ca.23773>.
- Hoffmann, M.F. *et al.* (2014) ‘Biomechanical evaluation of fracture fixation constructs using a variable-angle locked periprosthetic femur plate system’, *Injury*, 45(7), pp. 1035–1041. Available at: <https://doi.org/10.1016/j.injury.2014.02.038>.
- Hulse, R. and Cain, J. (1991a) ‘Bending Stress’, in R. Hulse and J. Cain (eds) *Structural Mechanics*. London: Macmillan Education UK, pp. 116–138. Available at: [https://doi.org/10.1007/978-1-349-11897-7\\_5](https://doi.org/10.1007/978-1-349-11897-7_5).
- Hulse, R. and Cain, J. (1991b) ‘Direct Stress’, in R. Hulse and J. Cain (eds) *Structural Mechanics*. London: Macmillan Education UK, pp. 98–115. Available at: [https://doi.org/10.1007/978-1-349-11897-7\\_4](https://doi.org/10.1007/978-1-349-11897-7_4).
- Inacio, J.V. *et al.* (2022) ‘Boundary Conditions Matter—Impact of Test Setup on Inferred Construct Mechanics in Plated Distal Femur Osteotomies’, *Journal of Biomechanical Engineering*, 144(081009). Available at: <https://doi.org/10.1115/1.4053875>.
- Intramedullary nailing: Basic technique* (no date) *AO SURGERY REFERENCE*. Available at: <https://surgeryreference.aofoundation.org/orthopedic-trauma/adult-trauma/basic-technique/basic-principles-of-im-nailing> (Accessed: 23 October 2024).
- Ito, K. *et al.* (2021) ‘Biomechanical Properties of Double-Row Transosseous Rotator Cuff Repair Combined With the Cinch Stitch in the Lateral Row’, *Orthopaedic Journal of Sports Medicine*, 9(5). Available at: <https://doi.org/10.1177/23259671211006040>.
- Jackson, C., Tanios, M. and Ebraheim, N. (2018) ‘Management of Subtrochanteric Proximal Femur Fractures: A Review of Recent Literature’, *Advances in Orthopedics*, 2018(1), p. 1326701. Available at: <https://doi.org/10.1155/2018/1326701>.
- Jankowski, J.M. (no date) ‘Fracture Classifications’. Available at: <https://ota.org/sites/files/2021-06/General%20A1%20Fracture%20Classifications.pdf>.
- Jones, O. (2023a) *Muscles in the Anterior Compartment of the Thigh*, *TeachMe Anatomy*. Available at: <https://teachmeanatomy.info/lower-limb/muscles/thigh/anterior-compartment/> (Accessed: 24 October 2024).
- Jones, O. (2023b) *Muscles in the Medial Compartment of the Thigh*, *TeachMe Anatomy*. Available at: <https://teachmeanatomy.info/lower-limb/muscles/thigh/medial-compartment/> (Accessed: 24 October 2024).

- Jones, O. (2024) *Muscles in the Posterior Compartment of the Thigh*, TeachMe Anatomy. Available at: <https://teachmeanatomy.info/lower-limb/muscles/thigh/hamstrings/> (Accessed: 24 October 2024).
- Kaiser, M.M. *et al.* (2012) 'Increasing stability by pre-bending the nails in elastic stable intramedullary nailing: a biomechanical analysis of a synthetic femoral spiral fracture model', *The Journal of Bone and Joint Surgery. British Volume*, 94(5), pp. 713–718. Available at: <https://doi.org/10.1302/0301-620X.94B5.28247>.
- Kaiser, M.M. *et al.* (2014) 'Modification of elastic stable intramedullary nailing with a 3rd nail in a femoral spiral fracture model – results of biomechanical testing and a prospective clinical study', *BMC Musculoskeletal Disorders*, 15, p. 3. Available at: <https://doi.org/10.1186/1471-2474-15-3>.
- Kandemir, U. (2018) 'Distal femur: dynamization of plating', *Injury*, 49, pp. S44–S48. Available at: [https://doi.org/10.1016/S0020-1383\(18\)30302-4](https://doi.org/10.1016/S0020-1383(18)30302-4).
- Karakaşlı, A., Satoğlu, İ.S. and Havitçioğlu, H. (2015) 'A new intramedullary sustained dynamic compression nail for the treatment of long bone fractures: a biomechanical study', *Eklem Hastalıkları Ve Cerrahisi = Joint Diseases & Related Surgery*, 26(2), pp. 64–71. Available at: <https://doi.org/10.5606/ehc.2015.16>.
- Kellam, J.F. (2018) 'Fracture Classification', in *AO Principles of Fracture Management*. Stuttgart: Georg Thieme Verlag KG. Available at: 10.1055/b-0038-160815.
- Khan, Y. (2019) 'Characterizing the Properties of Tissue Constructs for Regenerative Engineering', in R. Narayan (ed.) *Encyclopedia of Biomedical Engineering*. Oxford: Elsevier, pp. 537–545. Available at: <https://doi.org/10.1016/B978-0-12-801238-3.99897-0>.
- Kharb, A. *et al.* (2011) 'A review of gait cycle and its parameters', *IJCEM Int J Comput Eng Manag*, 13.
- Konda, S.R. (2017) 'Anatomy of the Proximal Femur', in K.A. Egol and P. Leucht (eds) *Proximal Femur Fractures: An Evidence-Based Approach to Evaluation and Management*. Cham: Springer International Publishing, pp. 1–7. Available at: [https://doi.org/10.1007/978-3-319-64904-7\\_1](https://doi.org/10.1007/978-3-319-64904-7_1).
- Konstantinidis, L. *et al.* (2017) 'Plate fixation of periprosthetic femur fractures: What happens to the cement mantle?', *Proceedings of the Institution of Mechanical Engineers, Part H: Journal of Engineering in Medicine*, 231(2), pp. 138–142. Available at: <https://doi.org/10.1177/0954411916682769>.

- Konya, M.N. *et al.* (2021) ‘Comparison of different fixation techniques for periprosthetic fractures: a biomechanical study of a new implant’, *International Orthopaedics*, 45(7), pp. 1817–1826. Available at: <https://doi.org/10.1007/s00264-021-05028-y>.
- Kramer, E.J. *et al.* (2016) ‘The Cost of Intramedullary Nailing for Femoral Shaft Fractures in Dar es Salaam, Tanzania’, *World Journal of Surgery*, 40(9), p. 1. Available at: <https://doi.org/10.1007/s00268-016-3496-z>.
- Larson, M.R. and Ryan, W. (2023) ‘Anatomy, Abdomen and Pelvis, Obturator Muscles’, in *StatPearls*. Treasure Island (FL): StatPearls Publishing. Available at: <http://www.ncbi.nlm.nih.gov/books/NBK589636/> (Accessed: 23 October 2024).
- Launico, M.V., Sinkler, M.A. and Nallamotheu, S.V. (2023) ‘Anatomy, Bony Pelvis and Lower Limb: Femoral Muscles’, in *StatPearls*. Treasure Island (FL): StatPearls Publishing. Available at: <http://www.ncbi.nlm.nih.gov/books/NBK500008/> (Accessed: 23 October 2024).
- Leckie, F.A. and Bello, D.J. (2009) *Strength and Stiffness of Engineering Systems*. Springer Science & Business Media.
- Lever, J.P. *et al.* (2010) ‘The biomechanical analysis of three plating fixation systems for periprosthetic femoral fracture near the tip of a total hip arthroplasty’, *Journal of Orthopaedic Surgery and Research*, 5, p. 45. Available at: <https://doi.org/10.1186/1749-799X-5-45>.
- Li, A.-B. *et al.* (2016) ‘Reamed versus unreamed intramedullary nailing for the treatment of femoral fractures: A meta-analysis of prospective randomized controlled trials’, *Medicine*, 95(29). Available at: <https://doi.org/10.1097/MD.0000000000004248>.
- Li, J. *et al.* (2020) ‘Materials evolution of bone plates for internal fixation of bone fractures: A review’, *Journal of Materials Science & Technology*, 36, pp. 190–208. Available at: <https://doi.org/10.1016/j.jmst.2019.07.024>.
- Lin, A.S.P. *et al.* (2017) ‘Biomechanics’, in S.Y. Smith, A. Varela, and R. Samadfam (eds) *Bone Toxicology*. Cham: Springer International Publishing, pp. 229–252. Available at: [https://doi.org/10.1007/978-3-319-56192-9\\_7](https://doi.org/10.1007/978-3-319-56192-9_7).
- Lo, D., Talkad, A. and Sharma, S. (2023) ‘Anatomy, Bony Pelvis and Lower Limb, Fovea Capitis Femoris’, in *StatPearls*. Treasure Island (FL): StatPearls Publishing. Available at: <http://www.ncbi.nlm.nih.gov/books/NBK519005/> (Accessed: 23 October 2024).
- Lochab, J. *et al.* (2017) ‘Do Transcortical Screws in a Locking Plate Construct Improve the Stiffness in the Fixation of Vancouver B1 Periprosthetic Femur Fractures? A

- Biomechanical Analysis of 2 Different Plating Constructs’, *Journal of Orthopaedic Trauma*, 31(1), p. 15. Available at: <https://doi.org/10.1097/BOT.0000000000000704>.
- Marsell, R. and Einhorn, T.A. (2011) ‘The biology of fracture healing’, *Injury*, 42(6), pp. 551–555. Available at: <https://doi.org/10.1016/j.injury.2011.03.031>.
- Medda, S., Unger, T. and Halvorson, J. (2023) ‘Diaphyseal Femur Fracture’, in *StatPearls Treasure Island (FL): StatPearls Publishing*. Available at: <http://www.ncbi.nlm.nih.gov/books/NBK493169/> (Accessed: 23 October 2024).
- Meinberg, E.G. *et al.* (2018) ‘Fracture and Dislocation Classification Compendium—2018’, *Journal of Orthopaedic Trauma*, 32, p. S1. Available at: <https://doi.org/10.1097/BOT.0000000000001063>.
- Merriman, D.J. *et al.* (2015) ‘The Effects of Intramedullary Reaming on Residual Long Bone Biomechanical Properties in a Composite Femur Model’, *Texas Orthopaedic Journal*, 1, pp. 59–70. Available at: <https://doi.org/10.18600/toj.010207>.
- Metcalfe, A.J., Saleh, M. and Yang, L. (2005) ‘Asymmetrical fracture fixation: stability of oblique fractures is influenced by orientation’, *Clinical Biomechanics*, 20(1), pp. 91–96. Available at: <https://doi.org/10.1016/j.clinbiomech.2004.09.003>.
- Miao, K.H. and Miao, J.H. (2023) ‘Radiological Diagnosis and Imaging of Femoral Shaft Fractures’, *Anatomia*, 2(3), pp. 282–299.
- Moein, C.M.A. *et al.* (2005) ‘Soft tissue injury related to choice of entry point in antegrade femoral nailing: piriform fossa or greater trochanter tip’, *Injury*, 36(11), pp. 1337–1342. Available at: <https://doi.org/10.1016/j.injury.2004.07.052>.
- Moher, D. *et al.* (2015) ‘Preferred reporting items for systematic review and meta-analysis protocols (PRISMA-P) 2015 statement’, *Systematic Reviews*, 4(1). Available at: <https://doi.org/10.1186/2046-4053-4-1>.
- Moore, P. and Booth, G. (2015) *The Welding Engineer’s Guide to Fracture and Fatigue*. 1st edn. Woodhead Publishing. Available at: <https://doi.org/10.1016/C2013-0-23229-3>.
- Morgan, E.F. and Buxsein, M.L. (2008) ‘Chapter 2 - Biomechanics of Bone and Age-Related Fractures’, in J.P. Bilezikian, L.G. Raisz, and T.J. Martin (eds) *Principles of Bone Biology (Third Edition)*. San Diego: Academic Press, pp. 29–51. Available at: <https://doi.org/10.1016/B978-0-12-373884-4.00024-0>.
- Mori, Y. *et al.* (2024) ‘A Review of the Impacts of Implant Stiffness on Fracture Healing’, *Applied Sciences*, 14(6), p. 2259. Available at: <https://doi.org/10.3390/app14062259>.

- Munih, M., Kralj, A. and Bajd, T. (1992) 'Bending moments in lower extremity bones for two standing postures', *Journal of Biomedical Engineering*, 14(4), pp. 293–302. Available at: [https://doi.org/10.1016/0141-5425\(92\)90003-4](https://doi.org/10.1016/0141-5425(92)90003-4).
- Nagler, J. (2019) 'Failure Mechanics of Multi Materials Laminated Systems Review Analysis-Based Project'. Available at: <https://doi.org/10.13140/RG.2.2.15062.91200>.
- Nandiraju, D. and Ahmed, I. (2019) 'Human skeletal physiology and factors affecting its modeling and remodeling', *Fertility and Sterility*, 112(5), pp. 775–781. Available at: <https://doi.org/10.1016/j.fertnstert.2019.10.005>.
- Niinomi, M. (1998) 'Mechanical properties of biomedical titanium alloys', *Materials Science and Engineering: A*, 243(1), pp. 231–236. Available at: [https://doi.org/10.1016/S0921-5093\(97\)00806-X](https://doi.org/10.1016/S0921-5093(97)00806-X).
- Nwagbara, I.C. (2019) 'Locked Intramedullary Nailing Using the Sign Nailing Device', *Nigerian Journal of Clinical Practice*, 22(4), p. 485. Available at: [https://doi.org/10.4103/njcp.njcp\\_245\\_18](https://doi.org/10.4103/njcp.njcp_245_18).
- O'Connell, R.S. *et al.* (2018) 'Biomechanical Evaluation of Osteoporotic Proximal Periprosthetic Femur Fractures With Proximal Bicortical Fixation and Allograft Struts', *Journal of Orthopaedic Trauma*, 32(10), p. 508. Available at: <https://doi.org/10.1097/BOT.0000000000001261>.
- Oesman, I., Kurniawan, D. and Canintika, A.F. (2023) 'Intramedullary nailing as a treatment for non-unions of femoral shaft fractures after plating failure: A case series', *International Journal of Surgery Case Reports*, 103. Available at: <https://doi.org/10.1016/j.ijscr.2023.107908>.
- Oh, S.-H. *et al.* (2024) 'Unstable Vancouver B1 periprosthetic femoral fracture fixation: A biomechanical comparison between a novel C-shaped memory alloy implant and cerclage wiring', *The Journal of International Medical Research*, 52(3), p. 03000605241240946. Available at: <https://doi.org/10.1177/03000605241240946>.
- Oksztulska-Kolanek, E. *et al.* (2015) 'The Biomechanical Testing for the Assessment of Bone Quality in an Experimental Model of Chronic Kidney Disease', *Nephron*, 132(1), pp. 51–58. Available at: <https://doi.org/10.1159/000442714>.
- Olson, S.A. *et al.* (2012) 'Designing a Biomechanics Investigation: Choosing the Right Model', *Journal of Orthopaedic Trauma*, 26(12), pp. 672–677. Available at: <https://doi.org/10.1097/BOT.0b013e3182724605>.

- Ömeroğlu, H. (2018) 'Basic principles of fracture treatment in children', *Eklem Hastalıkları Ve Cerrahisi = Joint Diseases & Related Surgery*, 29(1), pp. 52–57. Available at: <https://doi.org/10.5606/ehc.2018.58165>.
- O'Neill, F. *et al.* (2012) 'Validity of synthetic bone as a substitute for osteoporotic cadaveric femoral heads in mechanical testing: A biomechanical study', *Bone & Joint Research*, 1(4), pp. 50–55. Available at: <https://doi.org/10.1302/2046-3758.14.2000044>.
- Pairon, P. *et al.* (2015) 'Intramedullary nailing after external fixation of the femur and tibia: a review of advantages and limits', *European Journal of Trauma and Emergency Surgery*, 41(1), pp. 25–38. Available at: <https://doi.org/10.1007/s00068-014-0448-x>.
- Panagiotopoulou, O. (2009) 'Finite element analysis (FEA): Applying an engineering method to functional morphology in anthropology and human biology', *Annals of Human Biology*, 36(5), pp. 609–623. Available at: <https://doi.org/10.1080/03014460903019879>.
- Paruchuri, R.K., Choudur, H.N. and Chodavarapu, L.M. (2023) 'Orthopedic hardware in trauma - A guided tour for the radiologist - Part 1', *Indian Journal of Musculoskeletal Radiology*, 5, pp. 1–15. Available at: [https://doi.org/10.25259/IJMSR\\_43\\_2022](https://doi.org/10.25259/IJMSR_43_2022).
- Pauwels, F. (1980) *Biomechanics of the Locomotor Apparatus*. 1st edn. Heidelberg: Springer Berlin. Available at: <https://doi.org/10.1007/978-3-642-67138-8>.
- Pérez-Cano, F.D. *et al.* (2023) 'Human femur fracture by mechanical compression: Towards the repeatability of bone fracture acquisition', *Computers in Biology and Medicine*, 164, p. 107249. Available at: <https://doi.org/10.1016/j.combiomed.2023.107249>.
- Pfeifer, M. (2009) 'Chapter 6 - Degradation and Reliability of Materials', in M. Pfeifer (ed.) *Materials Enabled Designs*. Boston: Butterworth-Heinemann, pp. 161–187. Available at: <https://doi.org/10.1016/B978-0-7506-8287-9.00006-9>.
- Pierre, M.A. *et al.* (2010) 'Assessment of the bilateral asymmetry of human femurs based on physical, densitometric, and structural rigidity characteristics', *Journal of biomechanics*, 43(11), pp. 2228–2236. Available at: <https://doi.org/10.1016/j.jbiomech.2010.02.032>.
- Pierret, M. *et al.* (2022) 'Comparison of five methods for locked-plate fixation of complex diaphyseal fractures', *Orthopaedics & Traumatology: Surgery & Research*, 108(7), p. 103400. Available at: <https://doi.org/10.1016/j.otsr.2022.103400>.
- Polgaj, M. *et al.* (2013) 'Morphological study of linea aspera variations – proposal of classification and sexual dimorphism', *Folia Morphologica*, 72(1), pp. 72–77. Available at: <https://doi.org/10.5603/FM.2013.0012>.

- PRISMA for systematic review protocols (PRISMA-P)* (no date) *PRISMA statement*. Available at: <https://www.prisma-statement.org/protocols> (Accessed: 23 October 2024).
- Rivin, E.I. (2010) ‘Introduction and Definitions’, in *Handbook on Stiffness & Damping in Mechanical Design*. New York: ASME Press. Available at: <https://asmedigitalcollection.asme.org/ebooks/book/74/chapter/21433/Introduction-and-Definitions> (Accessed: 25 October 2024).
- Rixford, E. (1925) ‘THEORY AND TREATMENT OF SPIRAL FRACTURES’, *Annals of Surgery*, 81(1), pp. 368–373. Available at: <https://doi.org/10.1097/00000658-192501010-00033>.
- Roe, S.C. (2018) ‘Understanding the Limits of Biomechanical Testing’, *Veterinary and Comparative Orthopaedics and Traumatology*, 31(2), pp. vi–vii. Available at: <https://doi.org/10.1055/s-0038-1637025>.
- Rosa, N. *et al.* (2019) ‘Intramedullary nailing biomechanics: Evolution and challenges’, *Proceedings of the Institution of Mechanical Engineers, Part H: Journal of Engineering in Medicine*, 233(3), pp. 295–308. Available at: <https://doi.org/10.1177/0954411919827044>.
- Rudloff, M.I. and Smith, W.R. (2009) ‘Intramedullary Nailing of the Femur: Current Concepts Concerning Reaming’, *Journal of Orthopaedic Trauma*, 23, pp. S12–S17. Available at: <https://doi.org/10.1097/BOT.0b013e31819f258a>.
- Samiezadeh, S. *et al.* (2020) ‘Biomechanical Response under Stress-Controlled Tension-Tension Fatigue of a Novel Carbon Fiber/Epoxy Intramedullary Nail for Femur Fractures’, *Medical Engineering & Physics*, 80, pp. 26–32. Available at: <https://doi.org/10.1016/j.medengphy.2020.04.001>.
- Saraç, Ü., Karadeniz, S. and Özer, A. (2021) ‘Ideal plate screw configuration in femoral shaft fractures: 3D finite element analysis’, *Journal of Surgery and Medicine*, 5(5), pp. 540–543. Available at: <https://doi.org/10.28982/josam.925624>.
- Saunders, M.M. (2015) *Mechanical Testing for the Biomechanics Engineer: A Practical Guide*. Cham: Springer International Publishing (Synthesis Lectures on Biomedical Engineering). Available at: <https://doi.org/10.1007/978-3-031-01662-2>.
- Schorler, H. *et al.* (2016) ‘Bone plates for osteosynthesis – a systematic review of test methods and parameters for biomechanical testing’, *Biomedical Engineering / Biomedizinische Technik*, 62(3), pp. 235–243. Available at: <https://doi.org/10.1515/bmt-2015-0219>.

- Schorler, H. *et al.* (2017) 'Bone plate-screw constructs for osteosynthesis – recommendations for standardized mechanical torsion and bending tests', *Biomedical Engineering / Biomedizinische Technik*, 63(6), pp. 719–727. Available at: <https://doi.org/10.1515/bmt-2017-0126>.
- Sheen, J.R., Mabrouk, A. and Garla, V.V. (2023) 'Fracture Healing Overview', in *StatPearls*. Treasure Island (FL): StatPearls Publishing. Available at: <http://www.ncbi.nlm.nih.gov/books/NBK551678/> (Accessed: 23 October 2024).
- Sherman, M.A., Seth, A. and Delp, S.L. (2013) 'WHAT IS A MOMENT ARM? CALCULATING MUSCLE EFFECTIVENESS IN BIOMECHANICAL MODELS USING GENERALIZED COORDINATES', *Proceedings of the ... ASME Design Engineering Technical Conferences. ASME Design Engineering Technical Conferences*, 2013, p. V07BT10A052. Available at: <https://doi.org/10.1115/DETC2013-13633>.
- Srirekha, A. and Bashetty, K. (2010) 'Infinite to finite: An overview of finite element analysis', *Indian Journal of Dental Research*, 21(3), pp. 425–432. Available at: <https://doi.org/10.4103/0970-9290.70813>.
- Steffensmeier, A. *et al.* (2022) 'Clinical and Biomechanical Effects of Femoral Neck Buttress Plate used for Vertical Femoral Neck Fractures', *Injury*, 53(3), pp. 1137–1143. Available at: <https://doi.org/10.1016/j.injury.2021.12.004>.
- Steinke, P. (2010) 'Einleitung', in P. Steinke (ed.) *Finite-Elemente-Methode: Rechnergestützte Einführung*. Berlin, Heidelberg: Springer, pp. 1–13. Available at: [https://doi.org/10.1007/978-3-642-11205-8\\_1](https://doi.org/10.1007/978-3-642-11205-8_1).
- Szypryt, P. and Forward, D. (2009) 'The use and abuse of locking plates', *Orthopaedics and Trauma*, 23(4), pp. 281–290. Available at: <https://doi.org/10.1016/j.mporth.2009.07.002>.
- Taylor, M.E. *et al.* (1996) 'Stress and strain distribution within the intact femur: compression or bending?', *Medical Engineering & Physics*, 18(2), pp. 122–131. Available at: [https://doi.org/10.1016/1350-4533\(95\)00031-3](https://doi.org/10.1016/1350-4533(95)00031-3).
- Trompeter, A. and Newman, K. (2013) 'Femoral shaft fractures in adults', *Orthopaedics and Trauma*, 27(5), pp. 322–331. Available at: <https://doi.org/10.1016/j.mporth.2013.07.005>.
- Turner, C.H. (2006) 'Bone Strength: Current Concepts', *Annals of the New York Academy of Sciences*, 1068(1), pp. 429–446. Available at: <https://doi.org/10.1196/annals.1346.039>.

- Uhthoff, H.K., Poitras, P. and Backman, D.S. (2006) 'Internal plate fixation of fractures: short history and recent developments', *Journal of Orthopaedic Science*, 11(2), pp. 118–126. Available at: <https://doi.org/10.1007/s00776-005-0984-7>.
- Villwock, J. and Hanau, A. (2020) 'Statik starrer Körper', in B. Bender and D. Göhlich (eds) *Doppel Taschenbuch für den Maschinenbau 1: Grundlagen und Tabellen*. Berlin, Heidelberg: Springer, pp. 231–256. Available at: [https://doi.org/10.1007/978-3-662-59711-8\\_12](https://doi.org/10.1007/978-3-662-59711-8_12).
- Wähnert, Dirk *et al.* (2013) 'Biomechanical comparison of two angular stable plate constructions for periprosthetic femur fracture fixation', *International Orthopaedics*, 38(1), pp. 47–53. Available at: <https://doi.org/10.1007/s00264-013-2113-0>.
- Wähnert, D. *et al.* (2013) 'The potential of implant augmentation in the treatment of osteoporotic distal femur fractures: A biomechanical study', *Injury*, 44(6), pp. 808–812. Available at: <https://doi.org/10.1016/j.injury.2012.08.053>.
- Wähnert, D. *et al.* (2020) 'Periprosthetic fracture fixation in Vancouver B1 femoral shaft fractures: A biomechanical study comparing two plate systems', *Journal of Orthopaedic Translation*, 24, p. 150. Available at: <https://doi.org/10.1016/j.jot.2020.01.005>.
- Wang, I.-T. (2014) 'Numerical and experimental verification of finite element mesh convergence under explosion loading', *Journal of Vibroengineering*, 16(4), pp. 1786–1798.
- Wang, K. *et al.* (2019) 'Periprosthetic fracture fixation of the femur following total hip arthroplasty: A review of biomechanical testing – Part II', *Clinical Biomechanics*, 61, pp. 144–162. Available at: <https://doi.org/10.1016/j.clinbiomech.2018.12.001>.
- Welch-Phillips, A. *et al.* (2020) 'What Is Finite Element Analysis?', *Clinical Spine Surgery*, 33(8), p. 323. Available at: <https://doi.org/10.1097/BSD.0000000000001050>.
- Wendler, T. *et al.* (2022) 'Biomechanical testing of different fixation techniques for intraoperative proximal femur fractures: a technical note', *International Biomechanics*, 9(1), pp. 27–32. Available at: <https://doi.org/10.1080/23335432.2022.2142159>.
- Whittle, M.W. (2007) 'Chapter 2 - Normal gait', in M.W. Whittle (ed.) *Gait Analysis (Fourth Edition)*. 4th edn. Edinburgh: Butterworth-Heinemann, pp. 47–100. Available at: <https://doi.org/10.1016/B978-075068883-3.50007-6>.

- Willems, N. *et al.* (2013) 'The microstructural and biomechanical development of the condylar bone: A review', *European journal of orthodontics*, 36. Available at: <https://doi.org/10.1093/ejo/cjt093>.
- Windolf, M. *et al.* (2010) 'Biomechanical investigation of an alternative concept to angular stable plating using conventional fixation hardware', *BMC Musculoskeletal Disorders*, 11, p. 95. Available at: <https://doi.org/10.1186/1471-2474-11-95>.
- Wisanuoyotin, T. *et al.* (2023) 'Effect of bone cement augmentation with different configurations of the dual locking plate for femoral allograft fixation: finite element analysis and biomechanical study', *Journal of Orthopaedic Surgery and Research*, 18(1), p. 405. Available at: <https://doi.org/10.1186/s13018-023-03894-3>.
- Wright, D.J. *et al.* (2022) 'Nail diameter significantly impacts stability in combined plate-nail constructs used for fixation of supracondylar distal femur fractures', *OTA International*, 5(1), p. e174. Available at: <https://doi.org/10.1097/OI9.0000000000000174>.
- Yang, K.H. (2018) 'Chapter 6 - Prescribing Boundary and Loading Conditions to Corresponding Nodes', in K.-H. Yang (ed.) *Basic Finite Element Method as Applied to Injury Biomechanics*. Academic Press, pp. 257–280. Available at: <https://doi.org/10.1016/B978-0-12-809831-8.00006-4>.
- Yates, J.B. and Fountain, J.R. (2016) 'Fractures of the femur and tibial shaft', *Surgery (Oxford)*, 34(9), pp. 444–452. Available at: <https://doi.org/10.1016/j.mpsur.2016.07.001>.
- Zhang, S. *et al.* (2022) 'Experimental testing of fracture fixation plates: A review', *Proceedings of the Institution of Mechanical Engineers, Part H: Journal of Engineering in Medicine*, 236(9), pp. 1253–1272. Available at: <https://doi.org/10.1177/09544119221108540>.
- Zhang, Y. (2016) *Clinical Epidemiology of Orthopaedic Trauma, Clinical Epidemiology of Orthopaedic Trauma*. Thieme Verlag. Available at: <https://doi.org/10.1055/b-0036-133266>.
- Zhu, Y. *et al.* (2020) 'Epidemiology of low-energy wrist, hip, and spine fractures in Chinese populations 50 years or older: A national population-based survey', *Medicine*, 99(5). Available at: <https://doi.org/10.1097/MD.00000000000018531>.

## **Affidavit**

I hereby declare that I have written this bachelor's thesis on the topic "Analysis of the Effect of Proximal and Distal Displacement Constraints on the Femur During Biomechanical Testing for Diaphyseal Implants" independently without the help of third parties and without using any sources or aids other than those indicated.

I have indicated all passages in the thesis that are taken from printed works or sources from the Internet, either in wording or in meaning, by citing the sources. This also applies to all illustrations.

Hamburg, \_\_\_\_\_

Levita Graciella Valeriant